2009-12-15

Development of a Methodology for Numerical Simulation of a D C ARC Discharge in a Liquid Dielectric

Christopher James Lewis
Brigham Young University - Provo

DEVELOPMENT OF A NUMERIAL SIMULATION TOOL FOR MODELING A DC ARC DISCHARGE IN A LIQUID DIELECTRIC MEDIA

By

Christopher J. Lewis

A dissertation submitted to the faculty of

Brigham Young University

in partial fulfillment of the requirements for the degree of

Doctor of Philosophy

Department of Mechanical Engineering

Brigham Young University

April 2010

BRIGHAM YOUNG UNIVERSITY

GRADUATE COMMITTEE APPROVAL

of a dissertation submitted by

Christopher J. Lewis

This dissertation has been read by each member of the following graduate committee and by majority vote has been found to be satisfactory.

Date	Robert H. Todd, Chair
Date	Spencer P. Magleby
Date	Carl D. Sorensen
Date	Timothy W. McLain
Date	Christopher A. Mattson

BRIGHAM YOUNG UNIVERSITY

As chair of the candidate's graduate committee, I have read the dissertation of Christopher J. Lewis in its final form and have found that (1) its format, citations, and bibliographical style are consistent and acceptable and fulfill university and department style requirements; (2) its illustrative materials including figures, tables, and charts are in place; and (3) the final manuscript is satisfactory to the graduate committee and is ready for submission to the university library.

Date

Robert H. Todd
Chair, Graduate Committee

Accepted for the Department

Larry L. Howell
Graduate Coordinator

Accepted for the College

Alan R. Parkinson
Dean, Ira A. Fulton College of Engineering and Technology

ABSTRACT

DEVELOPMENT OF A NUMERIAL SIMULATION TOOL FOR MODELING A DC ARC DISCHARGE IN A LIQUID DIELECTRIC MEDIA

Christopher J. Lewis

Department of Mechanical Engineering

Doctor of Philosophy

The majority of literature regarding the numerical simulation of arc discharges in gaseous environments has used a plasma physics approach. Virtually all simulations treat the discharge as an idealized gaseous plasma, which can be described by temperature, pressure, and electric field. This approach can work well if the media is a shielding gas such as Argon; however, the approach does not work well for processes such as underwater welding, EDM, and underwater discharges used to generate high purity particles. The reason these discharges do not have many extensive simulation efforts as described in the literature is because they occur in liquid dielectric media (Oil and water) which complicates the simulation efforts. Most research efforts in these areas describe experimental methods to evaluate discharge properties

In this research a new method to investigate discharges in a dielectric media using an electrostatic and particle physics approach is proposed and validated. A commercial code that has been developed to simulate charged particle beams, dielectric materials, and perform multi-physics analyses, is the Vector Fields suite of solvers from Cobham Technical Services. This research demonstrates a simulation methodology that can be used to simulate a DC electric arc discharge in a lossy dielectric media using the Vector Fields environment. This simulation is the first of its kind to simulate this type of a discharge with a commercial FEA code. As such there are some limitations to the simulation. However, the simulation can be used to investigate the following:

1. Any metal, electrode geometry, discharge gap, or dielectric media can be studied
2. Primary Beam Physics
    - Electron velocity/acceleration (direct calculation of electron temperature)
    - Energy deposition on the anode from all emission sources
    - Effect of dielectric media on beam physics (trajectories, velocity, constriction, beam induced magnetic fields, space chare, and secondary emission)
    - Beam current
    - Particle trajectories (including relativistic effects)
3. Secondary Particle Generation and physics
    - Atomic species (neutral particles or ions) and secondary electron emission
    - Particle trajectories
    - Back ion bombardment on the cathode

ACKNOWLEDGEMENTS

I would like to thank Dr. Robert H. Todd for his constant support, encouragement, and mentoring. His influence has been one of the greatest on my professional outlook and career choices. I express my gratitude to each member of my committee who has provided important assistance and insight at various stages of the research. A special thanks to Gregory Andrews, James Boye, and Steven Elliott who were instrumental in mentoring through the Vector Fields simulation and charged particle beam physics, and to QLR, LLC who funded this research.

I would like to express my gratitude for my parents for their years of constant mentoring, encouragement, and support. Finally I express my love and gratitude to my beautiful wife and son who had the patience and provided constant encouragement to help me through the challenges and triumphs experienced in the course of this work. They are the greatest influence for good in my life.

TABLE OF CONTENTS

LIST OF TABLES

LIST OF FIGURES

1 Problem Statement

1.1 Introduction

This work was sponsored by QLR, LLC. QLR, LLC is investigating various uses of underwater DC arc discharges. QLR is interested in creating ultra fine metal and metal oxide aqueous slurries for use in various applications. QLR has partnered with Brigham Young University to develop a new manufacturing process machine and develop the associated numerical simulation the submerged DC arc discharge process. The purpose of the simulation for QLR was to determine the emission physics of the configuration and estimate the metal oxide formations and their relative distributions as a future tool to investigate the properties of materials created by the submerged arc process.

The majority of the literature regarding the numerical simulation and other modeling approaches for arc discharges has been accomplished using a plasma physics approach with ideal gas approximations (A. Anders 1990) (Fridman and Kennedy 2004). There are numerous examples of specialized simulation codes that have been developed to study special case gaseous discharges (Wendelstorf 2000), (Boxman and Gidalevich 2007-2008) (A. Anders 1990) (Benilov and Marotta 1995) (Bingul 2000) (Raizer 1991).

Discharges that occur in liquid dielectric media, such as oil and water, do not have extensive simulation efforts described in the literature because of the complicating physical interaction of the dielectric media. Dielectric media are sometimes referred to as lossy materials because they exhibit some conductivity, unlike an idealized insulator or gas. For this reason, much of the literature reviewing research on EDM processes, nano-structure generation, uniform high purity metals, underwater welding, high kV pulsed power discharges, and other discharged in liquid dielectrics have largely depended on experimental methods to evaluate discharge properties. However, this is an active area of research (Descoeudres 2006) (Gidalevich, Boxman and Goldsmith 2004) (Gidalevich and Boxman 2006) (Lan, et al. 2009) (Nakamura, et al. 2009) (Namihira, et al. 2007).

It has been shown that lossy dielectric materials can be investigated from an electrostatics and particle physics standpoint (Elliot 2009) (Simkin 2009). One commercial code that has been developed to deal with charged particle beams, electro-static simulation, lossy dielectric materials, and other multi-physics analyses is the Vector Fields suite of solvers from Cobham Technical Services. To date this software has never been used to simulate discharges. It is proposed that the particle physics approach can provide new insights into the physics and behavior of charged particles from a discharge occurring in a liquid dielectric media.

The remainder of this chapter describes the research hypothesis, objectives associated with this research effort, a summary of the primary contributions of this work, and the organization and format of this dissertation.

1.2 Hypothesis

It is hypothesized that the discharge physics of a DC electric arc discharge in a lossy dielectric media can be accurately simulated within the Vector Fields environment.

1.3 Research Objectives

There are two primary objectives of this research:

1. Develop a methodology to numerically simulate a discharge in a lossy dielectric media using a particle physics approach
2. Explore the range of usefulness and validate the methodology using a case study of interest (provided by QLR, LLC)

1.4 Primary Contributions of this Research Effort

The primary contributions of this research are:

1. Taken an existing tool and developed it for a new application
2. This newly developed tool is the first to simulate a discharge within a dielectric media
3. The results of using this tool confirms that a particle physics approach to simulating discharges is comparable to a plasma physics and experimental research
4. This new simulation tool can be used to provide greater insight into the following phenomenon for an underwater discharge:

a. The primary and secondary emission physics and particle trajectories
b. The effect of the dielectric media on emission physics, beam induced magnetic fields, and arc constriction
c. Anode energy deposition
d. Direct simulation of electron temperature for comparison to experimental spectroscopy measurements
e. New tool opens the door to developing process rules for creating particles using an underwater discharge

1.5 Outline of this Work

The following describes the format and organization of this work. Chapter 2 reviews and discusses classical and current relevant research efforts to understand, model/simulate, and describe gaseous and underwater electric arc discharges along with their many applications. Chapter 3 describes the simulation methodology to be able to simulate a discharge in a liquid dielectric. Chapter 5 presents a case study of the developed QLR manufacturing process machine and its associated process. Chapter 5 presents the results of applying the methodology to the case study. Chapter 6 presents the work done to validate the simulation for the case study and to investigate the useful range of the simulation. Chapter 7 outlines the key inferences and conclusions drawn from the case study and the simulation methodology. Finally, Chapter 8 presents the recommendations for future research.

2 Previous Research

2.1 Introduction

This chapter presents and discusses classical works and relevant research efforts aimed at understanding, modeling/simulating, and using underwater electric arc discharges for various purposes.

The classical uses of underwater arc discharges are welding and cutting applications (Lancaster 1986) (Ogawa 2002). The most active areas of research for underwater discharges are:

- Nanotechnology research efforts for carbon nano-structure formation
- Powder metallurgy (fine grain, high purity powders)
- Electro-discharge machining (EDM)
- Water and chemical purification (high kV pulsed power discharges).

Examples of carbon nano-structures are nano-tubes (Lau, et al. 2003) (Teo, et al. 2008-2009), nano-onions (Sano, et al. 2001), nano-fibers (Chhowalla, et al. 2003), nano-horns (Wang, et al. 2004), and nano-spheres (Yongning, et al. 2004). Powder metallurgy research uses underwater discharges to generate high purity, ultra-fine and micro-scale metal powders typically focused on refractory metals (tungsten, zirconium, and

germanium), though some transition metals are cited as well (Liu, et al. 2006) (Parkansky, et al. 2007). EDM has a wide body of literature and has seen a large increase in recent research efforts (Descoeudres 2006) (Qian, et al. 2005) (Korobeinikov and Melekhov 2002). Finally, research for using high kV pulsed discharges in water and oil product purification is increasing (Gidalevich and Boxman 2006) (Gidalevich and Boxman 2006) (Jones and Kunhardt 1995) (Lan; et al. 2009) (Namihira, et al. 2007).

Some emerging research areas using electric arc discharges in fluids include low energy discharges to create micro-shockwaves for particle delivery systems (medication), gene therapy, food preservation, wood preservation and conditioning, and cancer treatment (Jagadeesh and Takayama 2002).

Nano-particle generation and various forms of EDM are the most relevant research topics to the work of this dissertation. Another field that has many similarities to underwater discharges is vacuum arcs which have an extensive body of literature.

This chapter first presents a brief history of electrical discharges and the theoretical foundation for general gaseous electrical discharges. This is followed by a review of the existing body of literature for underwater arc discharges and the challenges of applying general gas discharge theory to underwater applications.

2.2 A Brief History of Electrical Arc Discharges

In the late 1700's Alessandro Volta created the first electrochemical battery, the "Voltaic Pile" (A. Anders 2003). It was the first major breakthrough to create and store electrical energy. The voltaic pile gave birth to man-made electrical arc discharges. Humphry Davy, an English Chemist and Vasilii Petrov, a Russian scientist independantly

discovered continous electric arc discharges powered by large voltaic piles in the early 1800's. Davy's demonstrations of continuously burning carbon arc lamps led the way for the development of glow discharge arcs and electric lighting (A. Anders 2003). Electric generators replaced voltaic piles and made larger scale electrical production possible by the late 19th century (Miller 2008).

By 1890, electric arc discharges were beginning to be used to join materials together. After the end of World War I, Comfort Avery Adams and twenty members of the Wartime Welding Committee of the Emergency Fleet Corporation founded the American Welding Society which since its inception has been dedicated to the advancement of welding and related processes (Miller 2008). By the late 1950's, the study of the physics of electric arc discharges and welding phenomenon was a topic of serious research and investigation (Lancaster 1986).

During the last 50 years, advancements in power supply technologies, manufacturing processes, metallurgy, and computing power have lead to increased understanding and modeling capabilities. Today electric arc research continues efforts to better understand and quantitatively model glow discharges, lighting, welding arcs, and vacuum arc discharges. It has also branched out to include electric arc discharges for nano-particle generation, chemical processing, water purification, and biological applications (Fridman and Kennedy 2004) (Jagadeesh and Takayama 2002) (Gidalevich, Boxman and Goldsmith 2004).

2.3 Electrical Arc Discharge Theory

Within this section, general electrical arc discharge theory is outlined. There are numerous derivations, theoretical formulations, and nomenclature in the literature on this subject. Fridman and Kennedy have compiled the most recent work of some six hundred texts, articles, journal papers, and other peer reviewed documents relating to plasma physics (Fridman and Kennedy 2004). Their reference book, Plasma Physics and Engineering published in 2004 contains an excellent body of literature on this subject. Raizer has also compiled an excellent reference text for gaseous electric arc discharges (Raizer 1991). Lafferty and later Boxman compiled extensive texts for vacuum arc physics and modeling (Lafferty 1980) (Boxman, Martin and Sanders 1995). Vacuum arc theory takes into special consideration the formation and behavior of cathode and anode spots. This work uses the nomenclature developed by Fridman and Kennedy to discuss general arc discharge theory.

The most important physics in a discharge are the emission characteristics. To form a discharge, some form of thermionic emission must occur. Emission occurs when a charged particle has enough energy to overcome the electrostatic forces that bind it in its natural structure (Murphy and Good 1956). Thermal and electrical energy are the primary mechanisms for causing thermionic emission through a cathode spot (Modinos 1984). Various forms of field emission, also known as electron emission or cold emission, play a role either in the pre-breakdown, breakdown, or arc sustaining phenomena. Field emission occurs when there is a sufficiently high electric field to impart enough energy to an electron to free itself from a metal surface (Fridman and Kennedy 2004). The emission characteristics of the cathode largely define the discharge

properties. The plasma, or positive column, is a charged region that develops in the gap between the cathode and the anode (Lozansky and Firsov 1975). The plasma column is a positively charged conductive fluid made up electrons, ions, and neutral particles. The type of plasma column generated determines the geometry and stability of the arc (Fridman and Kennedy 2004).

2.3.1 Classification of Arc Discharges

Electrical arc discharges (or thermal arc discharges) are classified by the principal cathode and positive column process mechanisms (Fridman and Kennedy 2004) (Raizer 1991) (Boxman, Martin and Sanders 1995):

1. Hot Thermionic Cathode – The cathode maintains a temperature of at least 3000 K where thermionic emission is the primary emission mechanism. Field (electron) emission is not required for the arc to be self-sustaining. The only possible cathode materials for sustained hot thermionic cathodes are the high melting temperature refractory elements (molybdenum, tungsten, etc.). TIG welding is an example of a hot thermionic cathode arc discharge.
2. Arcs with Hot Cathode Spots – Low melting temperature materials (copper, iron, etc.) cannot sustain temperatures above 3000 K so self-sustained thermionic emission cannot occur. Instead, the current in the cathode will focus to fine points along the surface and initiate intense field emission sites. This creates electron heating of these small emission sites that can escalate to create thermionic cathode spots that appear and move quickly across the electrode. These moving hot spots generate high local current densities and result in intensive, short heating and

evaporation of the cathode material. Because of the intense evaporation, the cathode spots cannot be sustained. Most forms of welding arcs fit into this category.

3. Vacuum Arcs – Occur only in a vacuum or a very low-pressure environment. In the absence of air or other gases, emission of electrons from the cathode takes place without creating a plasma discharge since the mean free path of gas atoms is too large to effectively form any ionized media. Vacuum arcs can be the result of thermionic emission; however, the most common cause of vacuum arcs is field emission (Lafferty 1980) (Boxman, Martin and Sanders 1995) (Harris 1980) (Latham 1995). Discharges within a vacuum typically cause intense erosion of the anode. The discharge channel is formed and sustained by the metal vapor generated from erosion and evaporation of the electrodes. The pre-breakdown phenomena and the formation of cathode spots in a vacuum are very similar to the formation of cathode spots in any dielectric media.
4. High-Pressure Arc Discharges – Occur when an arc is struck in an environment with pressures exceeding 10 atm. In these cases, the thermal plasma is dense enough to convert almost all of the discharge power to radiation. Common examples of high pressure discharges are xenon and mercury vapor arc lamps.

Copper is the primary material of interest in this research effort. Copper has a relatively low melting temperature and is not capable of sustaining thermionic emission and will naturally produce hot cathode spots. For this type of arc, the geometry of the electrodes and input power parameters determine if a single spot or multiple cathode spots are present at the same time. The number of cathode spots affects the amount of

energy available for ionization in the plasma column, the geometry of the plasma column, and the overall stability of the arc discharge (Fridman and Kennedy 2004).

2.3.2 The Arc Discharge Model

Electrical arc discharges cannot be described by a single set of equations and boundary conditions (Fridman and Kennedy 2004) (Boxman, Martin and Sanders 1995) (Wendelstorf 2000). Different physical phenomena control the physics of the arc discharge at different locations or layers. The physics that describe each of these layers are non-linear (Zhukov 1982). The electric arc discharge can be understood only through a system of non-linear interactions. Wendelstorf presented an exceptional work detailing an iterative *ab initio* modeling approach (computation based on fundamental principles, physical laws, and physical constants) for the quantitative prediction of gaseous electric arc discharge characteristics (Wendelstorf 2000).

In his work, Wendelstorf describes five sub-models of physical phenomena that must be included to analytically model or simulate the gaseous electric arc discharge:

1. Heat conduction within the solid electrodes
2. Electron emission from the cathode surface
3. Electrical and thermal transition from the electrode surface to the thermal plasma (sheath and pre-sheath)
4. Current and heat transport within the arc plasma column
5. Arc discharge geometry

Figure 2-1 shows a general arc discharge. This figure identifies the various physical layers that affect the formation and geometry of the arc discharge.

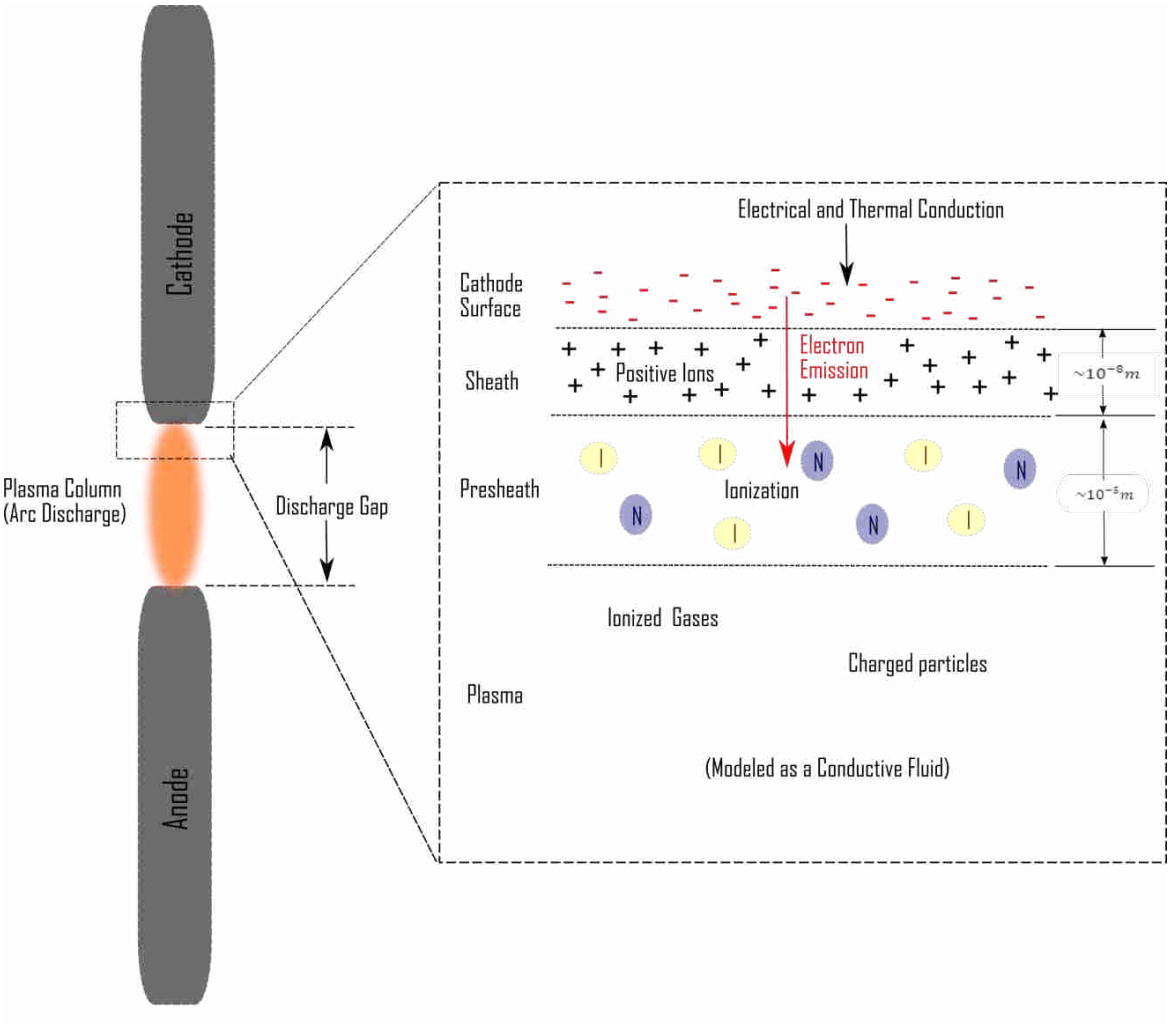

Figure 2-1: General Electric Arc Discharge

The heat conduction equation from the electrodes determines the amount of thermal and electrical energy that is available for electron emission. This energy is dependent on the current flow, material, electrode geometry, and surrounding media. The

two primary forms of media for an electrical arc discharge are gases (air, argon, carbon dioxide, etc) and liquids (water, alkaline solutions, and some liquid gases).

Electron emission depends on the surface temperature and the material's work function which is a measure of the binding energy of an electron to a metal surface (Fridman and Kennedy 2004). The work function can also be thought of as the amount of energy required to release an electron from the surface (Wendelstorf 2000). Cathode spots, erosion, and cathode heating are calculated within this sub-model (Fridman and Kennedy 2004).

Solution of the electron emission model provides necessary boundary conditions for the sheath and the pre-sheath models required to determine the electrical and thermal transition from the electrode surface to the plasma. The sheath sub-model defines the ionization, positive charge, and in many respects the stability of the plasma column.

The plasma column characteristics include the atomic state distribution (chemical makeup of the plasma), current transport, magnetic field, radiation, and plasma temperature (Wendelstorf 2000). Finally, the discharge geometry depends on electrode configuration (horizontal or vertical), burn type (free burning – unobstructed, free burning – obstructed, wall-stabilized, vortex-stabilized, coaxial flow stabilized, transpiration-stabilized, transferred, or non-transferred) (Fridman and Kennedy 2004). This research investigated a horizontal, free-burning – obstructed electrode configuration. The general physics that define the five sub-models are described below.

2.3.2.1 Heat Conduction within the Solid Electrodes

The heat conduction within the solid electrodes is modeled using Fourier's law and the heat diffusion equation as shown in equation 2.1 (Incropera and DeWitt 2002).

$$\rho C_p \frac{\partial T}{\partial t} = \nabla[k(T)\nabla T] + \dot{q} \quad \textbf{(2.1)}$$

Where:

ρ (kg/m^3) is the density

c_p (J/kg*K) is the specific heat

T (K) is the temperature distribution of the surface of the electrode where the arc occurs

t (seconds) is time

k (W/m*K) is the thermal conductivity

$\dot{q}$ (W/m^3) is the energy generation term (also called the Joule heating term)

The heat diffusion equation applies only for constant specific heat, though it does allow for variable thermal conductivity.

The temperature distribution is strongly influenced by the geometry of the electrode tip. In order for the arc to form, the current density has to be high enough to reach thermionic emission temperatures. The larger the total area of the electrode tip, the more difficult it is to get the whole tip up to thermionic emission temperatures. The thermal and electrical conductivity of a material and the geometry of the electrodes have the greatest effect on cathode hot spot formation, which in turn has the greatest effect on electron emission from the cathode surface (Wendelstorf 2000).

Temperature and material composition (impurities, doped, or alloyed electrodes) will have a significant effect on conductivity and thus hot spot formation. The primary

reason for this effect is that material composition affects the work function (the energy required to liberate an electron from the surface of the electrode). Extensive research efforts have focused on investigating doping materials to lower the work function to enable electron emission at lower temperatures and electric fields (Boxman, Martin and Sanders 1995) (Schneider 1999). The thermal conductivity with respect to temperature of some common materials in the literature is shown in Figure 2-2.

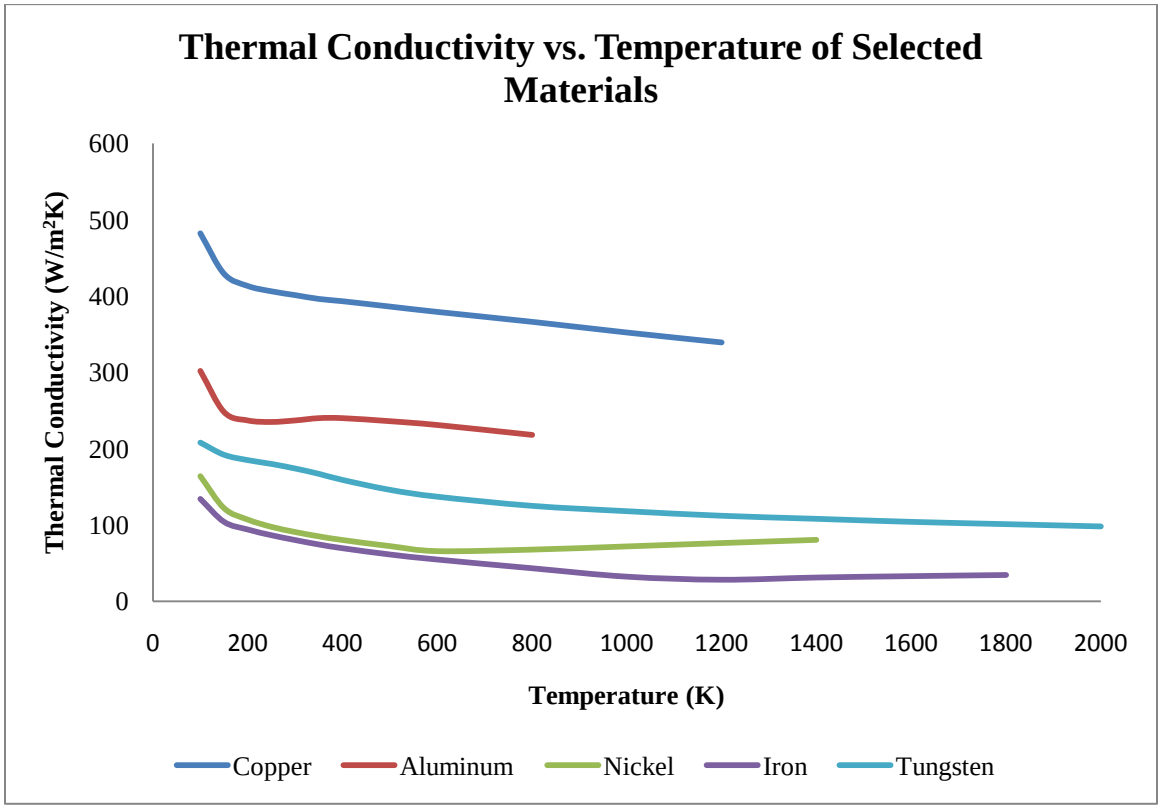

Figure 2-2: Thermal Conductivity of Common Electrode Materials (Efunda 2008)

2.3.2.2 Electron Emission from the Cathode Surface

In order for an arc to form, thermionic emission temperature must be reached at a cathode spot. Cathode spots form on the surface of the cathode where there is enough thermal energy and/or electron emission from the cathode to reach saturation current

density where the electrical field can break through the negative space charge that builds up on the cathode's surface (Fridman and Kennedy 2004). The electron distribution in a metal follows the quantum-mechanical Fermi function in Equation 2.2 (Landau and Lifshitz 1980).

$$f(v_x, v_y, v_z) = \frac{2m^3}{(2\pi h)^3} \frac{1}{1+exp\left(\frac{\varepsilon-\mu(T,n_e}{T}\right)} \quad \textbf{(2.2)}$$

Where:

m (kg) is the mass of an electron

h (m) is distance between the electron and the surface

ε (J) is the total energy (kinetic and potential) of an electron

$\mu(T, n_e)$ is the chemical potential (n_e is the total electron density)

The Fermi function describes the energy levels of electrons in a metal. The integration of the Fermi function leads to Equation 2.3, the Sommerfeld formula which describes the saturation current density for thermionic emission (Fridman and Kennedy 2004).

$$j = \frac{4\pi me}{(2\pi h)^3} T^2 (1-R) exp^{(-W/T)} \quad \textbf{(2.3)}$$

Where:

j (A/m) is the saturation current density

e © is the charge of an electron

h (m) is the distance between the surface of the metal and the electron

T (K) is the surface temperature of the cathode

R is the reflection coefficient of electrons (which ranges from 0 to 0.8)

W (eV) is the work function

The first term of Equation 2.3 is known as the Sommerfeld, or emission constant and the numerical value in Equation 2.4 is typically used.

$$S_C = \frac{4\pi me}{(2\pi h)^3} = 120 \frac{A}{cm^2 K^2} \quad \textbf{(2.4)}$$

However, the Sommerfeld (or emission constant) can change depending on the material and actual conditions. It is a factor that is often varied in numerical simulations to match experimental results (Vector Fields 2008-2009) (Elliot 2009) . The work function (W) is based on the Fermi function and describes the energy necessary to extract an electron from the metal (Fridman and Kennedy 2004). As noted previously many cathode materials are doped with low work function materials to reduce the energy necessary to extract electrons from the cathode (Wendelstorf 2000). Another way to lower the work function is to apply an external electric field. The work function is lowered because of the infusion of additional energy to excite the electrons in the metal which is known as the Schottky effect (A. Anders 1990). An expression for the work function is shown in Equation 2.5.

$$W = W_O - SE \quad \textbf{(2.5)}$$

Where:

W_o is the work function of a metal with no external electrical field (Equation 2.6)

SE is the Schottky correction factor (Equation 2.7)

$$W_O = \frac{e^2}{(4\pi\epsilon_O)4\alpha} \quad \textbf{(2.6)}$$

$$SE = \sqrt{\frac{eE}{4\pi\epsilon_O}} \quad \textbf{(2.7)}$$

Where:

e is the charge of and electron

α is the typical inter-atomic distance in the metal

E (V/cm) is the external electrical field applied to the cathode

ε_0 (J) is the permittivity of free space

If Equation 2.6 and Equation 2.7 are combined, a useable formulation for the work function is obtained. The numerical solution for the work function is often used for practical applications (Fridman and Kennedy 2004). Both forms of the work function are given in Equation 2.8.

$$W(eV) = \frac{e^2}{16\pi\varepsilon_O\alpha} - \sqrt{\frac{eE}{4\pi\varepsilon_O}} = \frac{e^2}{16\pi\varepsilon_O\alpha} - 3.8\times10^{-4}\sqrt{E} \quad \textbf{(2.8)}$$

If there is a strong external electric field (E > $1*10^6$ volts/cm), the electric field can pull electrons from even a cold metal. This cold emission is also called field emission. This behavior is classically modeled using a form of Equation 2.9, known as the Fowler-Nordheim formula (Fridman and Kennedy 2004).

$$j = \frac{e^2}{4\pi^2 h}\frac{1}{\left(W_O + \varepsilon_f\right)}\sqrt{\frac{\varepsilon_f}{W_O}}\,exp\left[\frac{4\sqrt{2m}W_O^{\frac{3}{2}}}{3ehE}\right] \quad \textbf{(2.9)}$$

Paulini et. al. describes this behavior in detail and describes how to perform thermo-field emission analysis initiated by field emission (Paulini, Klein and Simon 1993). Table 2-1 contains typical work functions for various materials based on work from Wojciechowski (Wojciechowski 1997), Fridman and Kennedy (Fridman and Kennedy 2004), and Vladimirov, et al (Vladimirov, Ostrikov and Samarian 2005).

Table 2-1: Work Function of Various Materials

Material	Work Function (eV)
Copper (Cu)	4.4
Carbon (C)	4.7
Iron (Fe)	4.31
Aluminum (Al)	4.25
Molybdenum (Mo)	4.3
Tungsten (W)	4.54
Platinum (Pt)	5.32
Nickel (Ni)	4.5

The melting temperature of the material, surface temperature, work function, Schottky effect, and Fowler-Nordheim effect have the largest effects on the emission characteristics at the cathode. Between seventy and ninety percent of the electric current in the positive plasma column results from these thermionic and field emission mechanisms (Fridman and Kennedy 2004). The remainder is generated by secondary electron emission mechanisms. The most important secondary electron emission mechanisms are the Townsend breakdown, Penning mechanism, potential electron emission, and photoelectron emission (Fridman and Kennedy 2004) (Vladimirov,

Ostrikov and Samarian 2005). All of these secondary mechanisms are caused by surface bombardment from ions, neutral or heavy particles, and/or free electrons (Boxman, Martin and Sanders 1995) (Latham 1995).

The Penning mechanism is the largest secondary emission mechanism. The Penning effect occurs when a positively charged ion approaches the surface of the cathode. If the ionization energy of the ion is higher than the work function of the material, the ion can draw an electron out from the metal surface. For a clean surface, the secondary ion-electron emission coefficient (γ) can be estimated using Equation 2.10 (Fridman and Kennedy 2004)

$$\gamma \approx 0.016(I - 2W) \quad \textbf{(2.10)}$$

Where:

I (eV) is the ionization energy of the approaching ion

W (eV) is the work function

If the surface is not clean, the secondary emission coefficient will be smaller. Many researchers have cataloged secondary emission effects for various materials (Boxman, Martin and Sanders 1995) (Zhukov 1982) (Vladimirov, Ostrikov and Samarian 2005) (Dobrestsov and Gomounova 1966) (Fransis 1960) (Granovsky 1971) (Komolov and Rachovsky 1992).

2.3.2.3 Transition from Electrode Surface to Thermal Plasma

The electrical and thermal transition from the surface of the cathode to the positive plasma column is divided into the sheath and the pre-sheath zones. The sheath, as was shown in

Figure 2-1, is a very thin skin where the positive ions are accelerated and bombard the surface of the cathode to cause the surface to reach the thermionic emission temperature, increase electron emission, and accelerate electrons into the pre-sheath where ionization can occur. Because of the length (10^{-8} m) and physical properties of the sheath, it can be modeled as a one dimensional problem (Wendelstorf 2000). As noted previously, electrons are drawn from the surface of the cathode by thermionic emission (γ_{eff}) and secondary emission (γ). The fraction of the electric current in the cathode sheath layer from thermionic emission can be calculated from Equation 2.11 (Fridman and Kennedy 2004).

$$S = \frac{\gamma_{eff}}{\gamma_{eff} + 1} \approx 0.7 - 0.9 \qquad \textbf{(2.1)}$$

The most important quantity to determine in the sheath is the voltage drop across the sheath layer (Wendelstorf 2000) (Vladimirov, Ostrikov and Samarian 2005) (Godyak and Sternberg 1990). The voltage leaving the sheath and transitioning into the pre-sheath determines the amount of energy available for ionization. To calculate the voltage drop, the electric field within the sheath must be determined. The sheath has been modeled as a collisionless (Fridman and Kennedy 2004) (MacKeown 1929) and a collision dominated space (Lister and Adler 1999) (Warren 1955). Collision dominated sheaths are typically associated with glow discharges while a collisionless sheath is associated with thermionic driven discharges. DC electric arc discharges are primarily thermionic; therefore, a collisionless sheath can be used.

The electric field is driven by the current density in the sheath layer. Poisson's equation for the voltage (V) in the collisionless layer has many formulations in the literature (Fridman and Kennedy 2004) (Wendelstorf 2000) (Vladimirov, Ostrikov and

Samarian 2005) (MacKeown 1929) (Shadowitz 1975) (Woodson and Melcher 1968). One representation is shown in Equation 2.12 (Fridman and Kennedy 2004).

$$-\frac{d^2V}{dx^2} = \frac{1}{2}\frac{dE^2}{dV} = \frac{e}{\varepsilon_0}(n_+ - n_e) = \frac{j}{\varepsilon_0\sqrt{2e}}\left[\frac{(1-S)\sqrt{M}}{\sqrt{V_s - V}} - \frac{S\sqrt{m}}{\sqrt{V}}\right] \quad \textbf{(2.12)}$$

Where:

M is the mass of the ions

m is the mass of electrons

V is the voltage

V_S is the voltage drop across the sheath

Integrating Equation 2.12 give a relationship for the electrical field in the sheath.

$$E_s{}^2 = \frac{4j}{\varepsilon_0\sqrt{2e}}\left[(1-S)\sqrt{M} - S\sqrt{m}\right]\sqrt{V} \quad \textbf{(2.13)}$$

Where:

j is the current density

ε_0 is the permittivity of free space

e is the charge of an electron

S is the fraction of electron current in the sheath layer

M is the mass of ions

m is the mass of electrons

V is the voltage

Equation 2.13 can also be written in numerical form:

$$E_S = 5 \times 10^2 A^{\frac{1}{4}}(1-S)^{\frac{1}{2}}V_S^{\frac{1}{4}}j^{\frac{1}{2}} \quad \textbf{(2.14)}$$

Where:

A is the atomic mass of ions (typically shown as the ions from the gas surrounding the discharge)

A second integration of the Poisson equation results in an expression for the length of the sheath (4).

$$\Delta l = \frac{4V_S}{3E_S} \tag{2.15}$$

In order to get a relationship for V_S, an energy balance at the sheath and pre-sheath edge is used. Again, the literature has multiple formulations for the energy balance. A simplified form is given in Equation 2.16 (Wendelstorf 2000).

$$V_S = \frac{jl}{eW} \tag{2.16}$$

It can be seen that the voltage drop is dependent on the current density, and electrical field of the ions bombarding the cathode and the work function of the material. In reality there are numerous elements that affect the voltage drop across the sheath.

Benilov and Marotta have developed a very comprehensive energy balance in the system which includes effects of radiation, conduction, feedback voltage from the plasma column, in addition to the primary energy fluxes in the system (energy from emitted electrons, work of the electric field over the sheath) (Benilov and Marotta 1995). Zuchov shows that there is not a significant difference in the results between more simplistic models and the more comprehensive models (Zhukov 1982). In most cases the conduction and radiation components do not have a significant effect on the voltage drop in the sheath and pre-sheath zones The pre-sheath is also known as the ionization zone. Fridman and Kennedy use a simplified energy flux balance to calculate the voltage drop across the sheath and pre-sheath shown in Equation 2.17 (Fridman and Kennedy 2004).

$$V_S = \frac{S + W - 1}{(1 - S)} \quad \textbf{(2.17)}$$

For a cathode spot to form, a minimum current (I_{min}) is required. The minimum current for most non-ferromagnetic materials can be found using the empirical formula Equation 2.18 (Fridman and Kennedy 2004).

$$I_{min} = 2.5 \times 10^{-4} T_{boil} \sqrt{k} \quad \textbf{(2.18)}$$

Where:

T_{boil} is the boiling point

k is the thermal conductivity of the cathode material

Cathode spots are also sources of intensive jets of metal vapor (Fridman and Kennedy 2004) (Lafferty 1980) (Boxman, Martin and Sanders 1995). Experimental data characterizing cathode spots for various materials can be found in Lafferty (Lafferty 1980) and Lyubimov and Rachovsky (Lyubimov and Rachovsky 1978).

2.3.2.4 Current and Heat Transport within the Arc Plasma Column

Most modeling approaches treat the plasma as an incompressible quasi-neutral conducting fluid (Wendelstorf 2000) (Lancaster 1986). The plasma is in motion and has some fluid flow which will satisfy the mass continuity and momentum equations. Most modeling approaches also treat the electrons and heavy particles as a single fluid (Wendelstorf 2000). Wendelstorf derives a comprehensive model for energy transport in a gaseous discharge. The heat transport in a discharge included conduction, convection, and radiation effects however, the discharge is primarily electrical in nature. Electrical energy is transferred via current and magnetic forces. Current transport follows Ohm's law. While there are generalized vector forms of the equation like Equation 2.19

(Vilsmeier 1982) others have shown that simplified models like Equation 2.20 are typically adequate (Wendelstorf 2000).

$$\vec{j} = \sigma \cdot \left\{ \vec{E} + \vec{v} \times \vec{B} - \frac{1}{en_e} \vec{j} \times \vec{B} + \frac{1}{2en_e} \vec{\nabla} p_e + 0.41 \cdot \frac{k_b}{2e} \vec{\nabla} T \right\} \quad \textbf{(2.19)}$$

$$\vec{j} = \sigma \vec{E} \quad \textbf{(2.20)}$$

The first term of Equation 2.19 is the effect of the electric field. The second term is the induction current from the voltage and magnetic fields. The third term is the Hall current. The fourth term represents the diffusion current. The fifth term is a representation of thermo-diffusion. The current from the electric field plays the most significant role, while there is evidence that the diffusion current can also play a role within the electric arc (Vilsmeier 1982).

An arc will also inherently produce a magnetic field which for discharges and charged particle beams the vector relationship is known as Biot-Savart's law demonstrated in Equation 2.21 (Wendelstorf 2000) (Vector Fields 2008-2009).

$$\vec{B}(\vec{r}) = \frac{\mu_0}{4\pi} \int \frac{\vec{j}(\vec{r}) \times (\vec{r} - \vec{r}')}{\left|\vec{r} - \vec{r}'\right|^3} d^3 r' = \frac{\mu_0}{4\pi} \int \frac{Idl \times \vec{r}}{r^3} \quad \textbf{(2.21)}$$

Where:

I is the current

dl is a differential element of the direction of the current

μ_0 is the magnetic constant

$\vec{r}$ is the displacement unit vector

r is the distance from the element to the point where the field is being computed

The magnetic effects from the beam physics can be significant in many applications and should not be ignored. This is particularly true of discharges in dielectric media (Boxman, Martin and Sanders 1995) (Fridman and Kennedy 2004) (Wendelstorf 2000).

2.3.2.5 Arc Discharge Geometry

The discharge geometry will largely depend on electrode configuration (Lozansky and Firsov 1975) (Hsu and Pfender 1984). There are six main types of electrode configurations. A general description is given below. For a more comprehensive description see (Fridman and Kennedy 2004).

- Free Burning Linear Arcs: Are either horizontal or vertical. In horizontal configuration, the burning gases have a buoyancy effect and form a visual arch shape. Sir Humphrey Davy observed this and termed it an arc (A. Anders 2003). An unobstructed arc is usually larger than the diameter of the electrodes and has a self-sustained arc. However, because of surface preparation, surface geometry, current inputs, or electrode material, the arc can become obstructed and the arc becomes electrode stabilized with a small discharge gap (Fridman and Kennedy 2004). The arc is smaller than the diameter of the electrodes in an obstructed, free-burning linear arc.
- Wall-stabilized: The anode of wall stabilized arcs is a tube. The cathode is at one end of the tube and the other end is typically a nozzle opening to air. The ignition gases flow into the tube and are ignited. The most common applications are for gas heating and cutting (plasma torch).

- Transferred Arc: Generally used in the metal refining and casting industries. Transferred arcs typically operate in the multi-megawatt power range. They system employs the use of a water cooled cathode which uses electron emission to transfer the arc to an external anode.
- Flow Stabilized Arc: These arc configurations utilize a second gas, or fluid, to stabilize the arc channel. Typical configurations include vortex-stabilized, coaxial flow stabilized, and transpiration-stabilized. In each case the secondary gas flow keeps the arc column in the center of the anode tube.
- Non-transferred Arc: The anode and cathode are opposite each other and a compressed gas flows between them pushing the arc out of an opening where the treatment material is placed.

Additionally the physical geometry of the electrodes and the configuration of the discharge gap will affect the shape of the discharge geometry.

2.3.2.6 Arc Discharge Theory Summary

An electrical arc discharge is a non-linear system requiring five sub-models to describe the physics of the arc. The five physical layers of modeling include the heat conduction in the electrodes, the sheath or space charge layer, the pre-sheath (ionization layer), the positive plasma column (arc column), and the discharge geometry and electrode configuration.

2.4 Underwater Arc Discharge Theory

Some of the primary differences between gaseous arcs and underwater arcs are the dielectric properties of gases are significantly different than water, the propagation of the plasma column, and the formation of a shock wave (Gidalevich and Boxman 2006) (Zel'dovich and Raizer 1966). The basic physics for arc formation is the same as for gaseous systems. The plasma properties are where the problem diverges (Gidalevich, Boxman and Goldsmith 1998) (Ridah 1998) (International Institute of Welding 1983).

The most common use of underwater electric arc discharges is underwater welding. The oil, gas, and naval industries are the largest users of underwater welding technology. Underwater welding is typically done at significant depths where the pressure around the discharge is significantly greater than atmospheric pressure which significantly changes the arc characteristics (International Institute of Welding 1983). For this reason there is significant private research efforts aimed at filler materials, mechanisms for creating dry arc conditions, and special electrodes and power supplies for underwater discharge applications (International Institute of Welding 1983) (American Welding Society 2009).

Many researchers using underwater discharges for nano-particle generation use open topped baths and perform the process relatively close to the surface so that high pressure arcs are not formed (Gidalevich and Boxman 2006) (Chhowalla, et al. 2003). It is important to maintain the discharge close to atmospheric pressures in order to be able to use low pressure arc physics.

Discharges in dielectric media have a number of additional layers in the discharge that do not exist in a gaseous discharge. The discharge must first create a conductive

channel through the media. In aqueous solutions, the phenomenon is typically associated with bubble formation near the electrodes (electrolysis separation of the hydrogen and oxygen), culminating in a visible streamer. This phenomenon has primarily been studied experimentally (Chadband 1993) (Descoeudres 2006) (Korobeinikov and Melekhov 2002) (Jones and Kunhardt 1995) (Nakamura et. al 2009). Figure 2-3 shows an example of bubble formation and a streamer from Descoeudres. For reference the bubbles are forming on cathode (Descoeudres 2006).

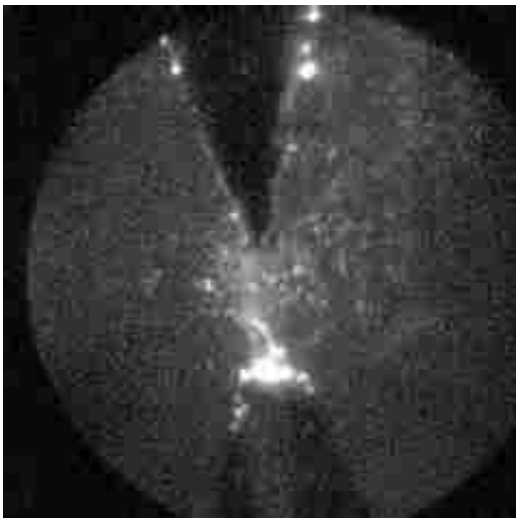

Figure 2-3: Bubble from the Pre-Breakdown (Descoeudres 2006)

The streamer which formed from the initial conduction path transitions into the positive plasma channel composed of vaporized and ionized dielectric media which forms a gaseous plasma bubble. In water, the plasma itself is composed almost entirely of disassociated and ionized hydrogen and oxygen and charged particles from the electrodes (Gidalevich and Boxman 2006) (Descoeudres 2006). The gaseous discharge is

surrounded by the dielectric media which exerts both physical pressures against the bubble as well as electrical insulation. Both effects can readily quench the discharge.

Adjacent to the plasma bubble, there is a transition layer of vaporized water molecules and unaffected dielectric media. Using high speed photography and other imaging techniques, discharges in dielectric media tend to form semi-spherical or parabolic plasma bubbles (Descoeudres 2006) (Gidalevich and Boxman 2006a) (Lan, et al. 2009).

Jones and Kunhardt proposed modeling the underwater arc discharge as a plasma bubble in water (Jones and Kunhardt 1995). This approach was followed and expanded by Gidalevich and Boxman (Gidalevich and Boxman 2006a) (Gidalevich and Boxman 2006b). The plasma column is bounded and enveloped in water. Gidalevich shows that the boundary conditions that exist for an underwater arc discharge are significantly different from a gas discharge. The plasma channel must expand within the water, pushing water away to generate a gaseous plasma column to sustain the discharge. At the boundary layer, water is vaporized and ionized (Gidalevich, Boxman and Goldsmith 2004). For many applications, including underwater welding, the disassociation and ionization of the hydrogen and oxygen atoms has undesirable effects (International Institute of Welding 1983) (Ducharme, et al. 1996) (Dowden and Kapadia 1994). The primary concern is the ionization of oxygen which causes rapid oxidation of any metallic media is contacts.

2.5 Chapter Summary

There were three major bodies of research reviewed for modeling and simulation approaches for gaseous, underwater, and arcs in other dielectric media. The list below summarizes the three research areas, and what aspects are most relevant and useful in this research effort.

- Submerged Arc-Discharges & Gaseous Discharges:
  - Relevant Aspects
    - Physics and methodologies used to develop predictive analytical models and simulations of gaseous discharges
    - Effects of water on discharges
- Electrical Discharge Machining
  - Relevant Aspects:
    - Modeling and simulation efforts of the EDM discharge
    - Effects of the dielectric on the discharge and particle generation
- Vacuum Arcs
  - Relevant Topics
    - Electron emission physics and modeling techniques of cathode and anode phenomena

These bodies of literature provide a description of the physics necessary to model the discharge, describe the challenges of modeling a dielectric fluid (i.e. water or oil), and provide insights regarding the relevant material properties and boundary conditions for the analytical model or numerical simulation developments.

The body of literature for discharges in dielectric media lacks the level of analytical modeling or numerical simulations that gaseous discharges have. The challenge is how to include the effects of the dielectric media on the discharge physics.

The key elements from the literature review that have significant impact on the remainder of this work are:

- The thermionic emission model used for DC arc discharges is the Sommerfield Formula
- The sheath of a discharge has a length between 0.01-0.1 mm in length
- The sheath can be characterized by a large acceleration of the electrons
- Positive ions will be attracted to the sheath through back ion bombardment and will help to neutralize the space charge in front of the cathode
- The work function for Copper is nominally 4.4 but has publication ranges between 4.3 and 4.5
- Discharges in dielectric media are constricted beams with large effects from beam induced magnetic fields which are modeled using Biot-Savart's law
- Disassociation through electrolysis occurs without a discharge in an aqueous media, it can be characterized by hydrogen bubble clinging to the surface of the cathode structure
- The liquid dielectric interacts with the primary electron beam and will alter the discharge physics

3 Numerical Simulation Methodology

This chapter will present the approach used to develop the numerical simulation of an arc discharge in a dielectric media within the Vector Fields software framework. Vector Fields is a commercial finite element (FEA) code from Cobham Technical Services used in national laboratories world-wide for multi-physics analysis of electrically energized systems. SCALA (one of the Vector Fields solvers) has been used to simulate electron beams, x-ray generation, klystron beams, and particle accelerators, glow discharges, mass transfer of charged particles in various media, and charged particle physics in outer space (Elliot 2009). The research team worked closely with Steven Elliot from Thin Films Consulting in developing the methodology to use Vector Fields to simulate the case study underwater arc discharge. To our knowledge, this is the first time a commercial numerical code has been used to simulate an underwater arc discharge in any form.

The general simulation methodology is described, followed by a detailed description of each of the steps of the simulation method. The primary task of the simulation methodology is to define the simulation inputs that are necessary to adequately simulate the geometry and discharge physics of the physical underwater discharge. A discussion and derivation of the physics employed in the simulation is included in Chapter 5.

3.1 Simulation Methodology

The methodology describes the simulation inputs that must be defined in order to develop a general simulation approach within the Vector Fields framework:

a. Define the simulation geometry (electrode shapes, plasma bubble geometry, vaporized transition layer, unaffected dielectric media, and discharge gap)
b. Define electrical boundary conditions
c. Identify and define material properties
d. Define emission surfaces/volumes and physics (thermionic, secondary emission, collision-less or collision models, etc.)

3.2 Define Simulation Geometry

As noted in chapter 2, the discharge physics are affected as much by electrode geometry and the surrounding media as they are by the physical and electrical properties of the electrode material. An arc discharge in a dielectric medium is made up of a number of physical layers that do not exist in an idealized gaseous discharge. There is a plasma bubble composed of vaporized and ionized slurry material and the electrons coming from the cathode, a boundary/film layer of vaporized and non-vaporized dielectric media, a region of dielectric media that is affected by the plasma but still in liquid phase, and finally the unaffected dielectric media that surrounds the discharge.

Gidalevich and Boxman and later Lan et.al. proposed modeling an underwater discharge plasma volume in flowing water as a gaseous cylindrical plasma volume (Gidalevich and Boxman 2006b) (Gidalevich, Boxman and Goldsmith 2004) (Lan et. al.

2009). Descoeudres proposed modeling an EDM discharge in water or oil as a spherical volume (Descoeudres 2006). Therefore, depending on the shape of electrodes and the dielectric fluid configuration (flow or no flow) the plasma volume can be modeled as a cylinder, sphere, or a combination of geometries.

Additionally, the discharge physics is dominated by the cathode spot phenomenon in non-refractory metals. The thermionic discharge is formed at small, random locations on the cathode surface. With cathode spot dominated discharges, very little of the surface of the electrode is involved in any given discharge. The simulation must define the cathode spot geometry and physics. Cathode spot phenomena such as cathode spot motion, splitting, and multiple cathode spot formation, all play a role in the discharge physics, but are not investigated in this research.

The following geometric considerations must be made in a general approach to simulating a discharge in a dielectric media:

1. Electrode geometry and configuration discharge gap
2. Cathode spot geometry and location
3. Plasma bubble geometry (size and shape)
4. Water vapor/slury transition layers between the plasma bubble and the unaffected dielectric media

A graphical view of these geometric considerations in a general simulation setup can be seen in Figure 3-6. The figure focuses on the location of the discharge showing that the discharge occurs in a small region between the cathode and anode surfaces regardless of the bulk geometry of the cathode and anode.

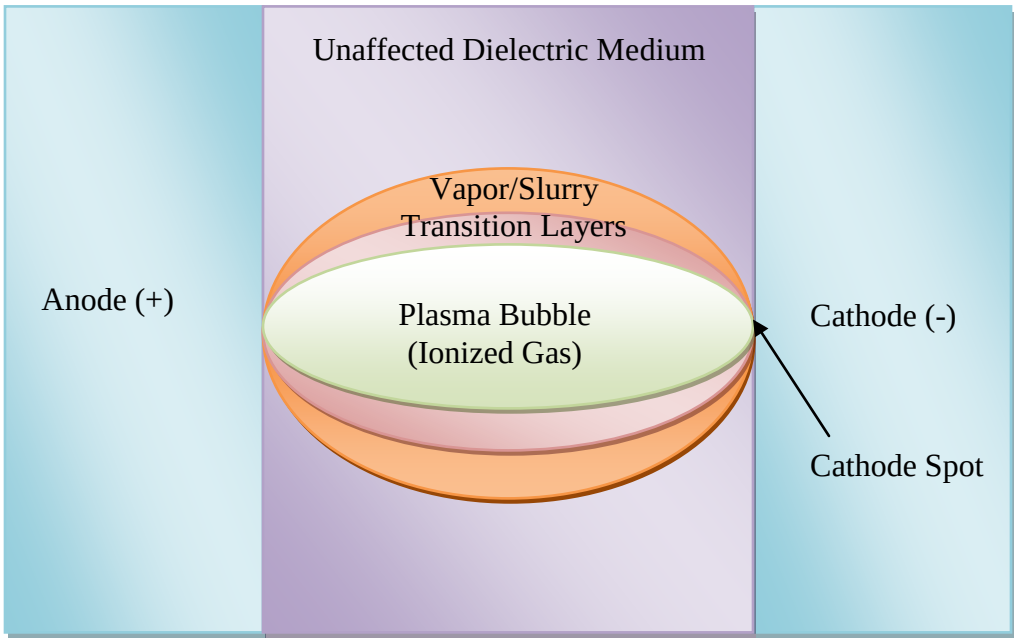

Figure 3-1: General Simulation Setup

3.3 Define Electrical Boundary Conditions

After the geometry of the simulation is defined, boundary conditions that define the electrical circuit must be defined. The simulation requires that a full electrical circuit is made. The cathode is placed at negative potential and the anode is either at ground potential or at a positive voltage potential. Either of these conditions will meet the requirements for the circuit. The voltage at the surface of the electrodes is defined by the user.

3.4 Define Material Properties

The material properties required for the simulation include the electrical properties of the electrode materials and the dielectric properties of the dielectric media. The electrical properties needed are the work function, emission constant, and the

cathode spot temperature of the cathode material. These properties are readily available in the literature for most materials of interest.

The dielectric properties of the media are not as readily obtained. The literature has dielectric properties for water, synthetic oils, and transformer oils which are common media used in submerged discharges. These published values are only for the unaffected dielectric media. In gaseous form, the conductivity of water will be as much as 10 times less than in liquid form (Lide 2007-2008) (Burgess 1999) (Yoder 2006).

In the plasma bubble the media is completely vaporized and ionized and thus becomes conductive plasma and ceases to be a dielectric media. The conductivity of the plasma is greater than a dielectric but will be significantly less than even a poorly conducting metal. Surrounding the plasma bubble is some region of gaseous, vaporized, and liquid dielectric. This region has some combination of the gaseous dielectric properties of the constituent compounds making up the media and the unaffected media. Dielectric properties for common gases are available in literature, but combinations of gases are not available. However, the properties of the primary (largest) constituents could form a baseline for investigation. This is the primary challenge to simulating discharges in dielectric media.

With this challenge, some method for estimating the properties for these regions is needed as there is no known method to determine the properties needed experimentally. The conductive plasma must have conductivity higher than water. The most conductive water in published literature is with ionic metal content (like salt water). Conductivity is typically measured in Semens/meter (Burgess 1999) (Yoder 2006). Salt water has a conductivity of 4.8 S/m as compared with 5.0×10^{-6} to 0.5 S/m for various

purities of water (Lide 2007-2008) (Yoder 2006). Therefore, the conductivity of the plasma is postulated to have a minimum conductivity of 5 S/m.

The conductivity of the transition layer must be some fraction of the conductivity of vaporized, liquid water, and conductive plasma. Since the conductivity of the gas is as much as 10 times lower than liquid water, the conductivity of the water content in the transition layer must be dominated by the dielectric properties of water, but the addition of conductive plasma constituents could increase the conductivity of the transition layer. It is postulated that the maximum conductivity of the transition layer of the discharge is 5 S/m and a minimum of 0.5 S/m.

Finally the conductivity of the slurry is highly dependent on the suspended metal/metal ion content. The conductivity of the slurry with the copper discharge can be directly measured as a function of time exposed to the discharge. ASTM testing standard D 877-00 determines the relative permittivity (dielectric constant) and conductivity of fluids using parallel plate electrodes (American National Standards Institute 2001). Following this test standard the conductivity of the slurry was measured in the experimental apparatus discussed Chapter 4. The following approach was used in this research to measure the dielectric properties of the slurry.

A series of controlled experiments were run to determine the change in conductivity over time. A controlled volume of water was exposed to the underwater discharge for a specific amount of time. At equally spaced time intervals 5 ml samples were extracted from the developing slurry. Each test run was terminated after eight hours. The change in conductivity was plotted as a function of time exposed to the

discharge. Figure 3-3 shows the average change in conductivity over time for the experimental apparatus.

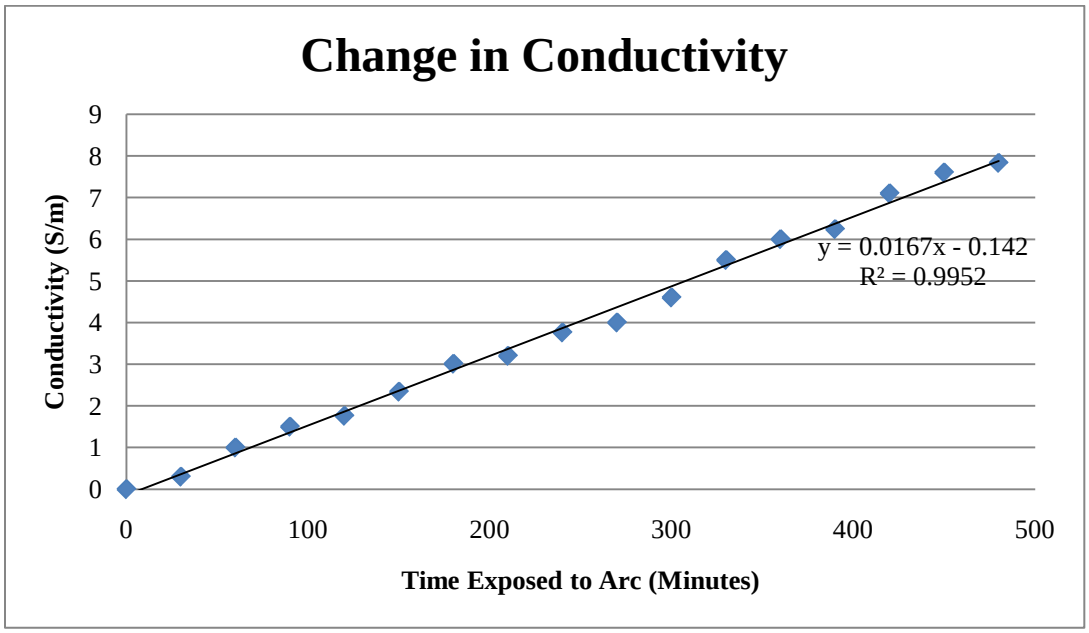

Figure 3-2: Change in Conductivity Over Time

The conductivity increased linearly with time exposed to the arc. The conductivity of the initial high purity water was approximately 5.0 x 10^{-6} S/m. The conductivity of the highest concentration of metal/metal-oxides in the slurry was approximately 8 S/m. Therefore for the simulation the relative ranges for the various layers can be estimated from this information. In summary, the postulated potential ranges for the conductivity of the various layers are:

1. Slurry: pure water to some level of ion content – 5.0x10^{-6} to 0.5 S/m
2. Transition Layers: some level of slurry and ion content – 0.5 to 5 S/m
3. Conductive Plasma: 5 S/m to 8 S/m

The second dielectric property needed is an estimate of the relative permittivity, or dielectric constant, for the various layers. Relative permittivity is a measure of capacitance in a material, or how electrostatic flux lines are focused in a given material (Latham 1995). The relative permittivity is dependent on chemical composition, temperature, and electric field (Boxman, Martin and Sanders 1995) (Latham 1995).

Water has a relative permittivity of 80 at room temperature and 34.5 as water vapor (Lide 2007-2008). Metals are not insulators and so are not typically given values of relative permittivity as metals do exhibit any level of capacitance. However, if metals were given relative permittivity the values would approach infinity as it approached a perfect conductor. The slurry has increasing values of ionic and metallic content which means that the relative permittivity of the solution will increase above the level of water.

As noted previously, ASTM 877-00 can also be used to determine the relative permittivity of the slurry. Figure 3-3 shows the change in relative permittivity with respect to the time exposed to the discharge for the samples from the eight hour experimental runs.

Like conductivity, the relative permittivity increased linearly with time exposed to the arc. The initial high purity water had relative permittivity of approximately 80 and the highest metal/metal-oxide concentration of the slurry was 92. However, these results are for a slurry at room temperature and do not directly represent the plasma, but it is postulated that they can be used to develop a range of values for the simulation.

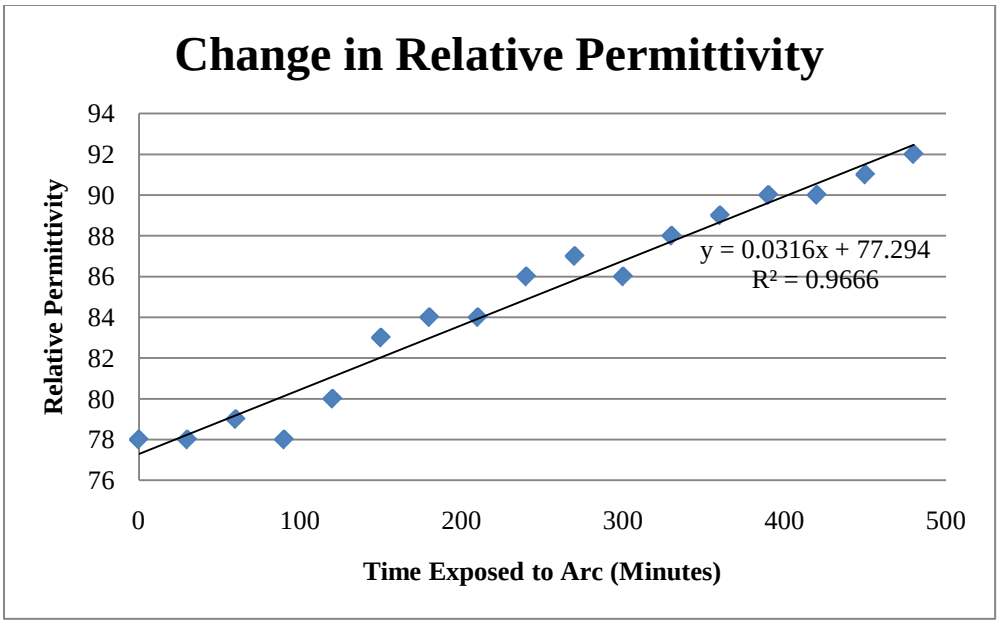

Figure 3-3: Change in Relative Permittivity Over Time

It is postulated that the conductive plasma, while not strictly a dielectric media, can be assumed to have higher relative permittivity than any other region. The transition layer made up of ionic particles, vaporized water, and liquid slurry and has some fractional combination of the various dielectric properties. The slurry will have a range between pure water and the measured slurry values. Therefore, the postulated potential ranges for the relative permittivity of the various regions are:

1. Slurry: 80 to 90
2. Transition Layers: 80 to 92
3. Conductive Plasma: 85 to 100

These postulated ranges for the conductivity and relative permittivity became the basis for the simulation input ranges for the various layers of the discharge gap.

3.5 Define Emission Surfaces/Volume and Emission Physics

Discharges in dielectric media are typically characterized by cathode spots, or cathode hot spots. Current focuses to a localized region typically a few μm in diameter (Wendelstorf 2000) (Fridman and Kennedy 2004) (Boxman, Martin and Sanders 1995). Field emission begins to occur in the pre-breakdown phase and begins to draw more current to the emission sight. Field emission, current, and temperature rise in the spot until there is a rapid transition to thermionic emission. The thermionic emission area can become as large as a few millimeters in diameter (Fridman and Kennedy 2004) (Boxman, Martin and Sanders 1995).

Therefore a discharge in a dielectric media can be simulated as a single, or multiple, cathode spots with the emission surface being defined as a circular surface between 0.001 - 2 mm in diameter. As noted in chapter two, the discharge physics of a thermionic discharge typically follow the Sommerfield formula. This is the primary emission physics for the model

As noted previously, the plasma will develop directly in front of the cathode spot in a semi-spherical or cylindrical shape. The plasma and transition layers can be defined as concentric spherical or cylindrical volumes that encapsulate the cathode spot and span the discharge gap to the anode. As the electrons in the primary beam cross the discharge gap they will interact with the dielectric media in the gap. This interaction will cause secondary electron emission in the gap as ions are formed with the dielectric media. This secondary electron and ion formation is included in this simulation.

When the primary electron beam collides with the anode, a large amount of energy must be dissipated by the anode. Most of the kinetic energy will be dissipated by heat,

but some of the energy will cause secondary emission of anode material particles (electrons and ions) and some of the beam will be backscattered back into the discharge gap. These phenomena are included in the simulation efforts of this work.

3.6 Chapter Summary

The following is a list of the key model inputs that must be defined for the simulation:

- Geometry of the electrodes and discharge gap
- Geometry of the cathode spot
- Geometry of the plasma bubble, transition layers, and surrounding dielectric media (these are defined so that the dielectric properties of each layer can be independently defined)
- Electrical boundary conditions on the surface of the cathode and anode
- The emission properties of the cathode material (work function, emission constant, and cathode spot temperature)
- The dielectric properties of the plasma bubble, transition regions, and unaffected dielectric media (relative permittivity-dielectric constant, and conductivity)
- The emission physics of the cathode spot (Sommerfield equation)
- The secondary emission characteristics of the dielectric media in the discharge gap (secondary emission fraction as a function of incident particle energy)
- The secondary emission and backscatter physics of the anode (emission fractions as a function of incident particle energy)

The inputs described in this chapter will fully define the simulation geometry and physics and allow for simulation of a discharge in a dielectric media from an electrostatic and particle physics approach.

As noted previously, Chapter 4 will briefly describe the case study using the manufacturing process machine developed for the research sponsor to evaluate the simulation methodology. Chapter 5 will show the results of applying the methodology to the case study, and Chapter 6 will describe the simulation validation and range of use.

4 Experimental Apparatus

This chapter presents the case study provided by QLR, LLC. QLR, LLC is interested in generating metal and metal oxide particles suspended in an aqueous solution. The primary material of interest in this research is copper. A laboratory process machine was setup for this research shown in Figure 4-1.

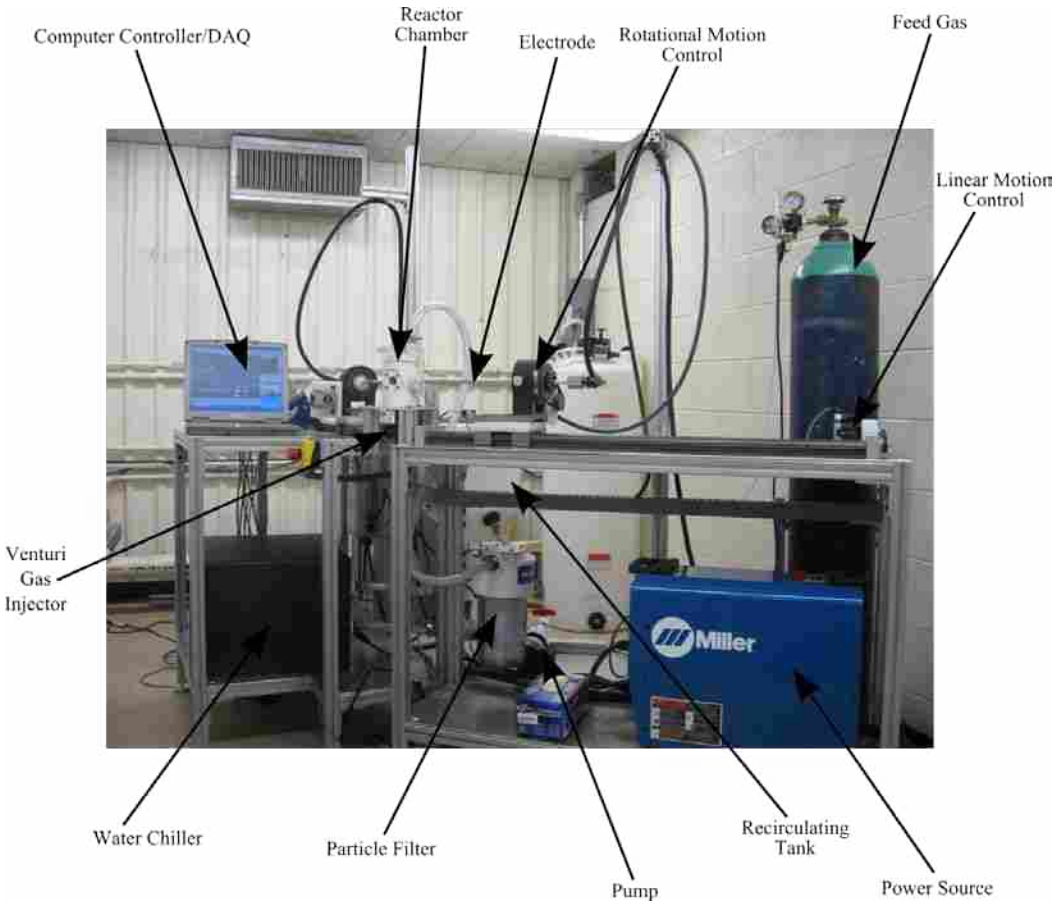

Figure 4-1: Experimental Process Machine

The machine is composed of two ½" diameter electrodes oriented 135° apart with rotational and linear motion controlled by a PID algorithm for autmated control of the discharge through the computer and data acquisition device (DAQ). The power supply for the discharge is a Miller XMT 359 MPA DC multi-process welding power supply.

The fluid management system is composed of a holding tank, recirculation pump, a water chiller (to control the temperature of the slurry), and a particle filter to ensure that large particles do not pass through the pump and damage the impeller. In some cases a feedgas (CO_2) was injected into the fluid stream via a Venturi gas injector in order to form carbonates from the metal oxides formed as a result of the discharge. All components that contacted the slurry were either polymers or ceramics to ensure there was no reaction between the slurry and the materials in the system.

The discharge occurred in a chamber that was fitted with a quartz window for physical observation of the discharge. There were two orientations for the window, one was a frontal view (as shown in the figure above) as well as a top view as shown in Figure 5-15.

Similar to other research efforts, solid rods were used as the electrodes because the end product is metal or metal-oxide powders or slurries and the larger diameter rod can be more readily automated than other electrode configurations (Chhowalla, et al. 2003) (M. Chhowalla 2008) (Gidalevich and Boxman 2006).

The purpose of the simulation for QLR was to determine the emission physics of the configuration and estimate the metal oxide formations and their relative distributions as a future tool to investigate other materials before using them in the process machine.

5 Simulation Results: Experimental Apparatus

This chapter will present and discuss the results of the case study simulation as the simulation methodology was applied. The results will be presented in the following order: the simulation geometry (electrode shapes, plasma bubble geometry, vaporized transition layer, unaffected dielectric media) and mesh considerations, electrical boundary condition, material properties, and emission surfaces/volumes and emission physics.

5.1 Experimental Apparatus Simulation Geometry

The following section presents the geometric considerations for the electrode configuration, dishcarge gap, plasma bubble geometery and the transition layer geometries, and the cathode spot geometry and location for the case study.

The electrodes are ½" diameter copper rods with a flat face as machined. Figure 5-1 shows some examples of characteristic still images of the underwater discharge using new electrodes. In all cases the cathode is on the right and the anode is on the left.

Figure 5-1: Example Discharges with New Electrodes

The figure on the left is a typical single cathode spot discharge generated across a 1 mm gap. The other two images show discharges with much more light intensity and bubble formation. While the discharge can vary in its light intensity and apparent size, the images show that the discharge typically occurs in the shortest gap between the two electrodes which varied in the process machine from 0.1 to 2 mm. Also, the materials are rotated to provide a fresh new surface for more uniform electrode wear. Over time the rods take on a ball and socket shape through erosion. The VF simulation uses the ball and socket shape for the discharge geometry as shown in Figure 5-2.

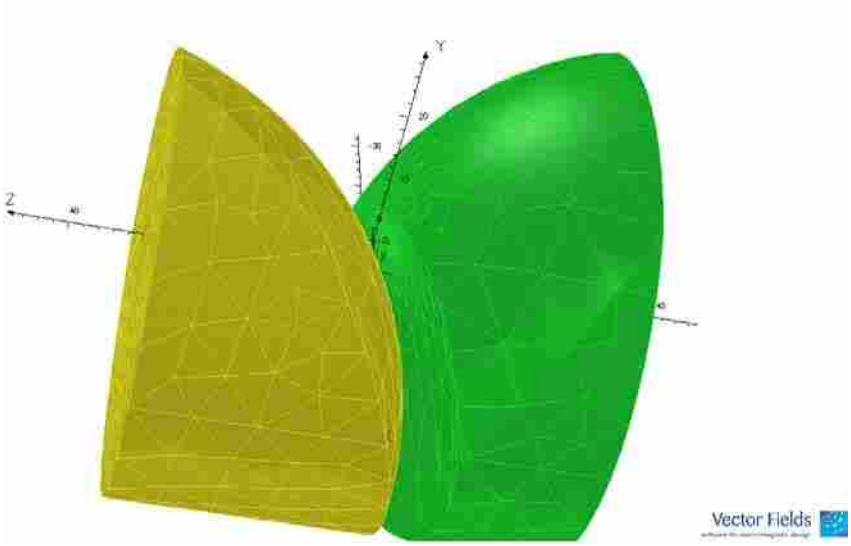

Figure 5-2: Vector Fields Model of the Electrode Structures

The average discharge gap from the process machine measurements was approximately 1 mm. The discharge gap for the model was initially set at 1 mm, but was investigated from 0.1 – 2 mm to see how the primary electron beams was affected by the discharge gap. The cathode spot is located on the surface of the cathode near the top of the socket. It can be located at the refined mesh visible in that region.

The literature discusses two primary ways to estimate the actual size of a cathode spot, filtered light intensity measurements and measurement of the cathode spot remnants on the cathode surface (Boxman, Martin and Sanders 1995) (Harris 1980) (Lafferty 1980) (Fridman and Kennedy 2004). Individual emission sites for copper are commonly reported as having a range of 0.01 - 0.1 mm in diameter for most materials of interest and that the affected area of a cathode spot can be larger than 1 mm in diameter (Boxman, Martin and Sanders 1995) (Fridman and Kennedy 2004) (Lafferty 1980) (Harris 1980). Figure 5-3 shows two typical cathode spot remnants from controlled single discharges of copper electrodes at 1000x magnification from the process machine.

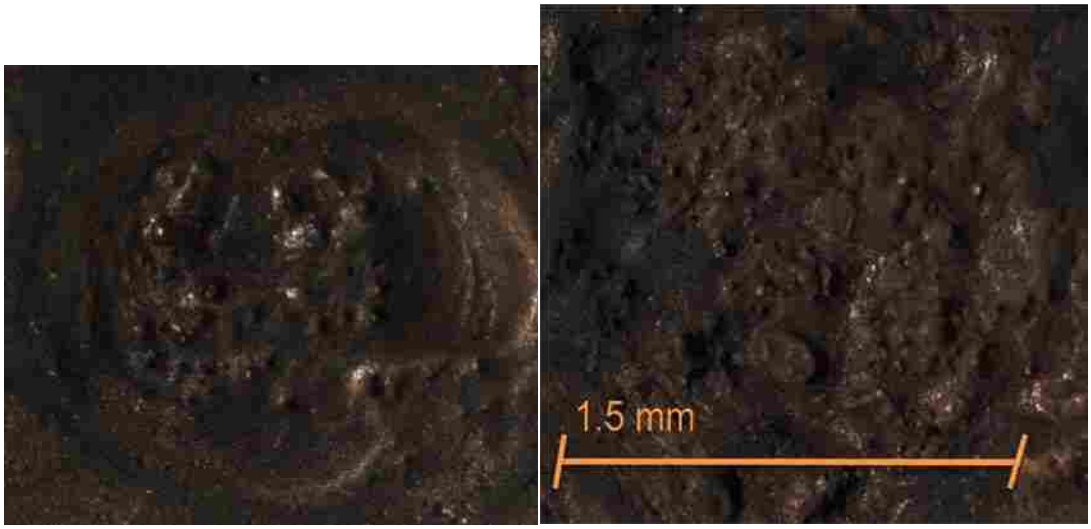

Figure 5-3: Cathode Spot Remnants

These images are typical of the 30 cathode spot remnants reviewed. The range of affected regions in a cathode spot varied from 0.4-1.6 mm in the longest dimension with the average ~1mm. The shortest dimension ranged from 0.26-1.56 mm with an average length of ~0.96 mm. Cathode spot remnants were roughly circular in nature. Figure 5-4 shows a histogram of the longest length dimension.

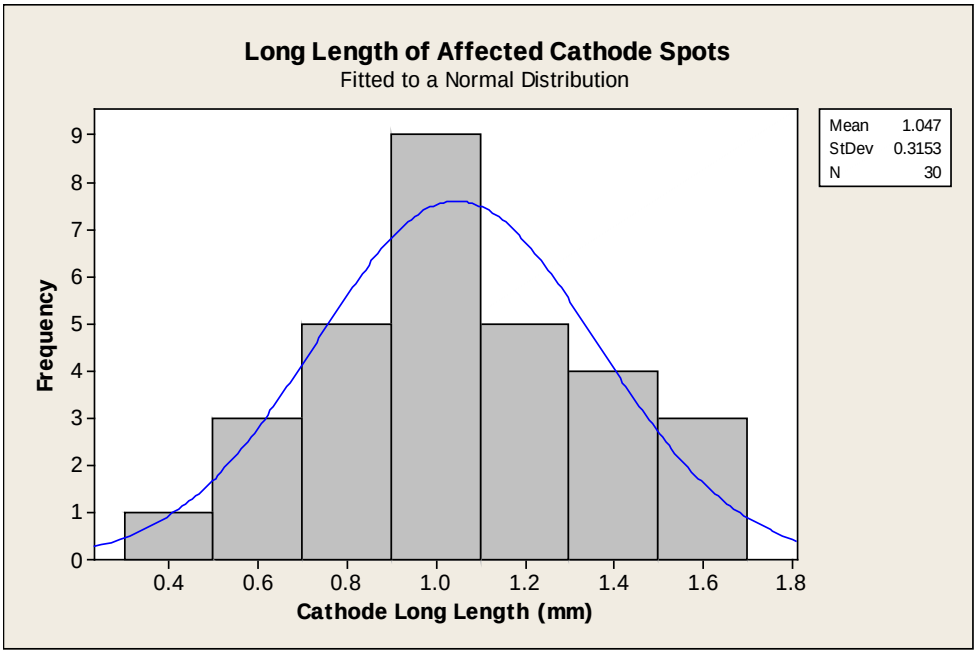

Figure 5-4: Long Length of Affected Cathode Spot Remnants

The data is well described by a normal distribution for the affected length of the cathode spots. The cathode spot remnants also have smaller pitted structures within the affected area of the cathode spot. The pitted structures, or craters, are individual emission sites. To better view these smaller structures an SEM image of a portion of a cathode spot remnant is shown in Figure 5-5.

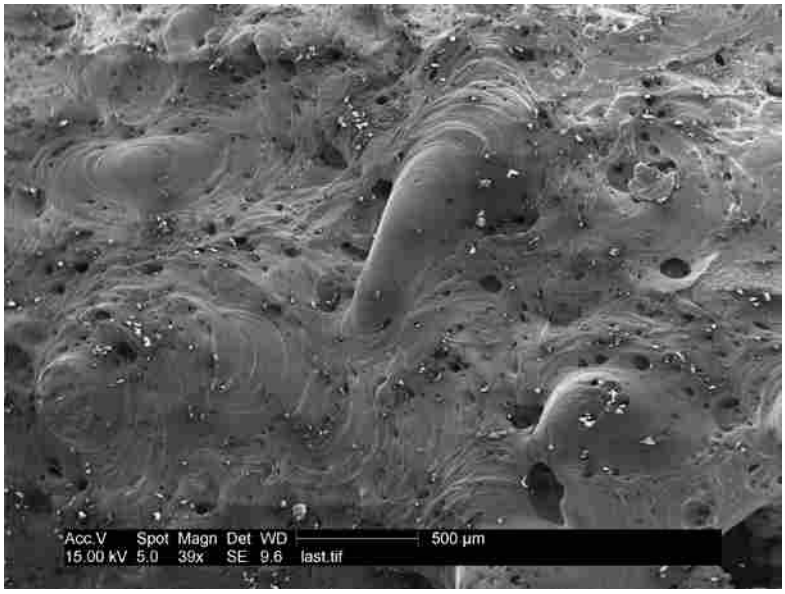

Figure 5-5: Cathode Spot Remnant SEM

The small craters range in size from ~10 to 100 µm. The dimensions of the individual sites and the total affected emission sites from the cathode spot remnants agree with the published literature for the copper electrodes listed above.

The simulation requires the emission surfaces and volumes to be defined by the user. It is not practical to define individual emission sites from the SEM level, but rather to use the total emission area such as shown in Figure 5-3. Because the individual emission sites are not simulated, the cathode spot from the simulation will not have all of the residual physical characteristics as an actual cathode spot.

The cathode spot is a simulation input and is based on the measurements above. As noted above, the average affected diameter of a cathode spot is 1 mm and spots are roughly circular. Therefore, the spot is simulated as a 1 mm diameter circular patch on the surface of the cathode. The spot has uniform thermionic emission (current density)

following the programmed emission physics. An example of the current density of a one millimeter cathode spot is shown in Figure 5-6.

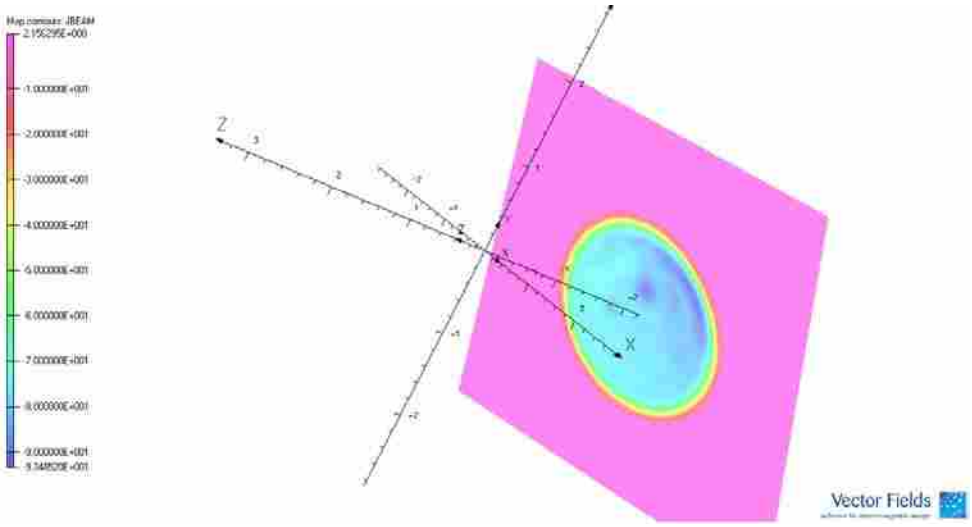

Figure 5-6: Current Density Map of a 1 mm Diameter Cathode Spot

The VF plots show that the current density is highest in the blue regions and lowest in the red regions. The pink region indicates that there is no emission from this portion of the surface. The units are in Amperes/mm^2 and show the expected uniform emission from the simulated region. Since the cathode spot is a simulation input and the simulation treats the spot as a uniform emission source, the simulation spot characteristics cannot be compared to the cathode spot remnants to be used to validate the simulation. The spot remnants were used to setup the simulation.

Finally, the plasma bubble, transition layers, and surrounding media were modeled as concentric spheres of increasing size. This geometry was chosen based on digital and high speed images taken of the discharge and that there are examples of using this geometry in the literature (Descoeudres 2006). A cross section view of the Vector

Fields model with the surfaces meshed with the emission surfaces and volumes identified is shown in Figure 5-7.

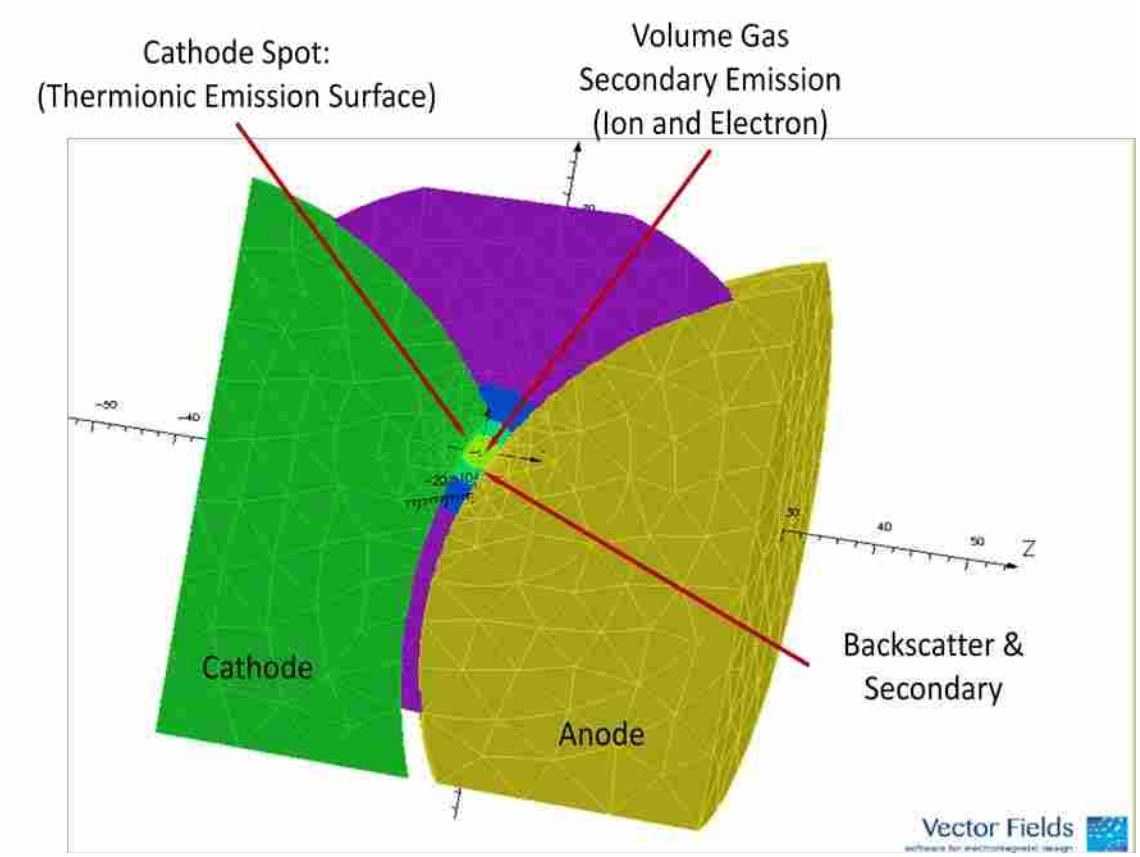

Figure 5-7: Cross Section of Vector Fields Model

The primary electron beam is expected to primarily travel through the innermost region (yellow). This region is considered to be the primary plasma bubble. It stretches from the cathode to the anode and fully envelope the cathode spot. This region has the tightest mesh to ensure that there is an appropriate level of resolution for the numerical solver. There are two transition layers modeled (green and blue). The mesh in the green layer is only slightly larger than the yellow region to have good resolution and to

optimize computational costs. The blue region is further relaxed as it is anticipated that the primary beam will not travel through this region but will still have secondary particle trajectories in the region. Finally the purple region represents the unaffected dielectric media and has the most relaxed mesh since there should be very little occurring outside of the blue model region.

5.2 Electrical Boundary Conditions and Material Properties

The only electrical boundary conditions required are the voltages at the surfaces of the electrodes. These voltages are defined by the power supply. The welding power supply used in the case study has a drive voltage of 72 volts. In operation the voltage drops to approximately 25 volts as current flows and the discharge is generated. The simulation assumes infinite current and would therefore be able to theoretically maintain the drive voltage of the power supply. There are methods to include current and voltage drops in the simulation software; however, this simulation work does not include these techniques but leaves them as recommendations for future research. The results in this section use the assumption of infinite current and 72 volts. Chapter 6 includes a discussion on the effect of the emission voltage boundary condition (72 vs. 25 volts) on the simulation results.

The electrodes are both made from oxygen-free copper 101 round bar stock. Copper is an extensively researched material and the work function, emission constant, and the cathode spot temperature of the cathode material are readily available in the literature (Boxman, Martin and Sanders 1995) (Fridman and Kennedy 2004) (Efunda 2008) (Terunuma, et al. 1997).

An important characteristic of all dielectric media is that they exhibit some electrical loss characteristics (have non-zero conductivity) (Latham 1995) (Damamme, Le Gressus and De Reggi October 1997). This behavior makes it difficult to simulate from a plasma physics standpoint, but from an electrostatic view, the lossy characteristics can be readily included in the simulation.

Additionally, the water does not retain the same dielectric properties throughout the discharge zone. The plasma bubble is highly conductive mostly gaseous plasma. The transition layers at the edge of the bubble are composed of vaporized water and liquid water with variable conductivities. And within a short period of time, the surrounding water volume is filled with metal and metal oxide particles which rapidly change the conductivity of the slurry. Each of these layers needs to be assigned different dielectric properties in order to accurately simulate the discharge.

As noted in chapter three, the dielectric properties of the slurry were estimated by extrapolating data from the literature and a developing slurry using ASTM testing standard D 877-00 which determines the relative permittivity (dielectric constant) and conductivity of fluids using parallel plate electrodes (American National Standards Institute 2001).

Using the information from the previous sections, the ranges for the various input parameters for the case study simulation can be developed. Table 5-1 summarizes the ranges of electrical and dielectric property inputs for the simulation.

Table 5-1: Model Attribute Ranges Investigated in VF Simulation

Model Attribute	Properties	Copper	Source
Electrical	Work Function (eV)	4.3 - 4.5	Literature
	Cathode Spot Temperature (K)	3,500 - 4,500	Literature
	Emission Constant (A/cm^2K^2)	120	Literature
Boundary Conditions	Cathode (V)	-25 to -72	Measurement
	Anode (V)	0	Measurement
Cathode Spot	Size (mm)	0.15 – 2	Literature, Measurement
	Discharge Gap (mm)	0.5 - 2	Measurement
Plasma Bubble	Relative Permittivity	85 - 100	Estimated from Measurement and Literature (EFM,L)
	Conductivity (S/m)	5 - 10	EFM,L
Plasma/Slurry Transition	Relative Permittivity	80 - 92	EFM,L
	Conductivity (S/m)	1 - 5	EFM,L
Slurry	Relative Permittivity	80 – 85	Measurement
	Conductivity (S/m)	0.001 – 0.1	Measurement

5.3 Define Emission Surfaces/Volume and Emission Physics

As shown in Figure 5-2, there are three primary emission surfaces/volumes to define. There is the cathode spot, the volumetric secondary emission (electrons and ions in the discharge gap), and backscatter electrons and secondary emission from the anode. Each of these emission surfaces or volumes is defined in this section. Additionally the

FEA physics of the Vector Fields software is also describe to show how the software computes important physical phenomena.

5.3.1 **Vector Fields Physics**

Three dimensional stationary electromagnetic fields can be defined as a sum of the solenoidal and rotational fields (Vector Fields 2008-2009). Electrostatic fields (with no rotational component) can be evaluated using the electrostatic potential. Therefore the electric field can be calculated by:

$$E = -\nabla V \tag{5.1}$$

Where:

E (V/m^2) is the electric field

V (Volts) is the electrostatic potential

The divergence of electric flux density is related to the charge density by:

$$\rho = \nabla \cdot D \tag{5.2}$$

Where:

D (C/m^2) is the electric flux density, or the displacement field

ρ (C/m^2) is the charge density

The electric flux density is related to the electric filed by the dielectric permittivity tensor by:

$$D = \varepsilon E \tag{5.3}$$

Where:

ε is the dielectric permittivity tensor

Using this relationship and by combining 5.1 and 5.2, Vector Fields solves a form of Poisson's equation to obtain the electrostatic properties of the simulation.

$$\nabla \cdot \varepsilon \nabla V = -\rho \tag{5.4}$$

Where:

ε is the dielectric permittivity tensor

V (Volts) is the electrostatic potential

ρ (C/cm^2) is the charge density

Similarly current flow is solved with another embodiment of Poisson's equation:

$$\nabla \cdot \sigma \nabla V = -\rho \tag{5.5}$$

Where:

σ (Siemens/mm) is the conductivity

V (Volts) is the electrostatic potential

The total energy (Joules) can be calculated by:

$$J = \sigma E \tag{5.6}$$

Magnetic fields have both solenoidal and rotational components. Vector Fields uses two methods to evaluate the magnetic fields depending on if there is current flowing in the magnetic material. If current is flowing, VF splits the total field into two components to solve for the magnetic field (Vector Fields 2008-2009):

$$H = H_m + H_s \tag{5.7}$$

Where:

H_m is the is the reduced field intensity

H_s is the conductor field intensity

The reduced field intensity is represented by the reduced scalar potential (ϕ):

$$H_m = -\nabla\phi \tag{5.8}$$

The conductor field intensity is represented by:

$$H_s = \int_{\Omega_J} \frac{J \times R}{|R|^3} d\Omega_J \tag{5.9}$$

Where:

J is the is the total energy vector

R is the distance vector

When there are no currents flowing in the magnetic materials, the total magnetic field can be evaluated using the total magnetic scalar potential and the permeability tensor with Poisson's equation:

$$\begin{aligned} H &= -\nabla\psi \\ \nabla \cdot \mu\nabla\psi &= 0 \end{aligned} \tag{5.10}$$

Where:

μ is the permeability tensor

ψ is the total magnetic scalar potential

Vector Fields applies both methods to reduce numerical errors in solution. Additionally Biot-Savart beam induced magnetic fields can be applied to a simulation if included by the user.

5.3.2 **Cathode Spot Emission Physics**

Field emission is the precursor to thermionic emission and a visible discharge. Thermionic emission in gaseous discharges is typically modeled with some form of the Sommerfield formula (Wendelstorf 2000) (Fridman and Kennedy 2004). The

Sommerfield formula is dominated by the thermal effects of the emission and is also defined as a thermal saturation limiting emission model (Vector Fields 2008-2009). One of the most commonly used thermal saturation models derived from the Sommerfield formula is called the Richardson-Dushman equation (Fridman and Kennedy 2004). Other thermionic emission models are current density, or space charge limiting models (Child's Law and Langmuir/Fry) and Maxwell velocity distribution models. This simulation uses the Richardson-Dushman equation defined as (Vector Fields 2008-2009):

$$j = AT^2 \exp\left(\frac{-q_e\phi_w}{kT}\right) \quad \textbf{(5.11)}$$

Where:

A (A/cm^{2}K^2) is the emission constant

T (K) is the temperature of the cathode

q_e(Coulomb) is the electronic charge

ϕ_w(eV) is the work function

k (J/K) is the Boltzmann constant = 1.3806508x10^{-23}

The Richardson-Dushman emission model is defined by the cathode work function, cathode spot temperature, and emission constant. These are the material properties for the cathode that were defined previously.

The underwater discharge of the case study is categorized as an obstructed arc that is cathode stabilized (Fridman and Kennedy 2004). This means that the plasma is not permitted to become self-sustaining because of the influence of the electrodes, energy inputs, and surrounding dielectric media. Because of this, there should be a significant beam induced magnetic effect. This magnetic effect is modeled with Biot-Savart's law demonstrated in Equation 2.21 (Wendelstorf 2000) (Vector Fields 2008-2009).

$$\vec{B}(\vec{r}) = \frac{\mu_0}{4\pi}\int \frac{\vec{j}(\vec{r})\times(\vec{r}-\vec{r}')}{\left|\vec{r}-\vec{r}'\right|^3} d^3r' = \frac{\mu_0}{4\pi}\int \frac{Idl\times\vec{r}}{r^3} \quad \textbf{(5.12)}$$

Where:

I is the current

dl is a differential element of the direction of the current

μ_0 is the magnetic constant

$\vec{r}$ is the displacement unit vector

r is the distance from the element to the point where the field is being computed

The Richardson-Dushmann equation was used to model the thermionic emission and was coupled to the Biot-Savart equation to simulate the primary electron beam physics. It will be shown that the magnetic effects induced from the beam have a significant effect on the simulation results.

5.3.3 **Volume Secondary Emission**

As the primary electron beam travels across the gap from the cathode to the anode there are collision interactions between the beam and the dielectric media. These collisions between the highly energized electrons in the beam and the atoms and molecules in the beam path will generate secondary particles. The most common particle will be secondary electron emission as ions are formed.

Secondary emission is defined by the incident particle's velocity, energy, and angle of impact. Secondary emission, and backscattering are typically modeled as having a cos(θ) distribution (Elliot 2009) (Malton 2009). This distribution is used because this secondary emission has been shown to have little correlation between incident angle and

emission particle angle and this distribution has strong correlation to experimental results in many applications (Boxman, Martin and Sanders 1995) (Malton 2009). Therefore, to simulated secondary particle generation an expression for a distribution of particles with a range of energies, velocities, and emission angles is needed. This distribution is derived as a function from a distribution of charged particles with a distribution of velocities, energies, and angles of impact to the region of interest.

It is common to define an emission fraction for the surface, volume, or line of interest. The emission fraction then can be used with a probability density function to simulate the generation of secondary particles. Within Vector Fields, the emission fraction is determined through a triple over the region of interest over the range of input energies and trajectories (Vector Fields 2008-2009)

$$\delta_s = \int_0^{E_{in}} \int_0^{\frac{\pi}{2}} \int_0^{2\pi} \gamma(E,\theta,\varphi) \sin\theta \, \partial E \partial\theta \partial\varphi \qquad \textbf{(5.13)}$$

Where:

δ_s is the total yield (emission fraction)

E is the energy of the incident particle

θ is a polar angle of the incident particle

φ is the azimuthal angle of the incident particle

γ is a secondary particle generation distribution function of energy and angles

Secondary emission in a volume must be tied to the energetic particles of the primary beam. Secondary emission can only occur along the beam and has some probability density distribution for the probability of secondary particle generation and direction. In this case polar angle is measured from the primary beam direction vector

(Vector Fields 2008-2009). So the general emission fraction of the volume is defined by the number of secondary particles generated per the number of incident particles per unit length of the beam path:

$$\delta_s = \frac{N_{\sec ondaries}}{n_{\Pr imary}} \tag{5.14}$$

Where:

N is the total number of secondary particles generated

n is the total number of incident particles

Or in terms of the volume integral:

$$\delta_s = \int_0^{E_{in}} \int_0^{\frac{\pi}{2}} \int_0^{2\pi} \frac{N_{\sec ondaries}}{n_{primary}\, l} P(E,\theta,\varphi)\, \partial E \partial\theta \partial\varphi$$
$$Where: \iiint P(E,\theta,\varphi) \partial E \partial\theta \partial\varphi = 1 \tag{5.15}$$

Where:

l (cm) is the beam length

$P(E, \theta,\varphi)$ is a normalized probability density function for the secondary particles

Within Vector fields a number of back-scattered and secondary emission fractions have been pre-programmed for typical applications in a vacuum envelope based on energy loss and estimates of particle generation per primary particle. The emission fractions can also be fully developed by the user to define secondary emission fractions.

With an underwater or gaseous discharge, the secondary particles are most likely to be emitted along the beam direction. The particle generation can be assumed to have an axially symmetric distribution about the primary particle trajectory since the likelihood of emission will decrease with increased angle and have a zero probability of

backwards emission (Malton 2009). This means that there is no dependence from the azimuthal angle. Also because the distribution can be assumed to be axially symmetric the output distribution is redefined as a $\cos^2(\theta_{out}/2)$ distribution (Simkin 2009). The volume integral simplifies to:

$$\delta_s = \int_0^{\frac{\pi}{2}} \gamma(E,\theta)\sin\left(\frac{\theta}{2}\right)\partial\theta \qquad \textbf{(5.16)}$$

If the distribution is defined to have equal probability that a secondary particle will have any energy between zero and the incident particle energy the dependence on incident energy also is removed. John Simkin and Steve Elliott have worked to simulate the secondary particle generation on a wide variety of gaseous secondary particle generation simulations (Elliot 2009). They have found that the emission fraction for many gaseous volume secondary particle generation can be simulated by defining $\gamma(E,\theta)$ as:

$$\gamma(E,\theta) = \frac{1}{2\pi\, 10^6} \qquad \textbf{(5.17)}$$

Therefore integrating 5.16 with the distribution factor in 5.17, the following expression for the emission fraction for the volume secondary particle generation can be obtained:

$$\delta_s = \frac{1}{2}\left(\frac{\cos^2\left(\theta_{out}/2\right)}{2\pi\, 10^6}\right) \qquad \textbf{(5.18)}$$

This emission fraction was programmed into the simulation to determine the volume secondary particle generation (electrons and ion generation) in the discharge gap. The gaseous particle generation simulation was used because it is assumed that the

majority of the secondary emission will occur in the plasma bubble, where it is commonly simulated as an ideal gas.

5.3.4 **Anode Emission Phenomena**

When the primary electron beam collides with the anode a large amount of energy must be dissipated by the anode. Most of the kinetic energy will be dissipated by heat causing the surface of the anode to melt with some metal vaporization and ionization. Additionally, some of the energy will cause secondary emission of anode material particles (electrons and ions) and some of the beam will be backscattered back into the discharge gap.

Similar to the volume secondary emission, it is possible to either use the built-in backscattering or secondary emission functions or to define the emission fraction. The built-in backscatter and secondary emission functions use a cos(θ) distribution. The backscatter random particle generator is based on a user defined energy loss fraction and the backscatter emission fraction is defined as:

$$\delta_s = \xi \cos\theta \tag{5.19}$$

A common loss fraction for backscattering simulations is 0.85. This means that the average energy of a backscattered particle is 85% of the incident particle energy (Elliot 2009) (Simkin 2009). In many applications this has been found to have good correlation with experimental results in many applications.

Similarly the secondary emission uses a user defined expression for the average energy of the secondary particles generated. Often the average energy of the secondary particles is assumed to be between 50% and 75% of the incident particle energy. The

secondary emission fraction can also be programmed into the simulation if there is knowledge about the physics from experimental results.

This simulation results show a 0.85 loss factor backscatter plot to demonstrate the potential trajectories of backscattered particles (as these particles will emit some photons as they change energy states and influence the shape of the illuminated plasma bubble). The secondary emission used the built-in emission fraction with both a 50% and 75% incident particle energy distribution function.

The backscattered and secondary emission characteristics of the anode have not been completely validated through experimental results but are used to show the potential use of these features to better define the discharge physics and potentially identify specific chemical compounds formed as a result of the discharge.

5.4 Simulation Results: Primary Electron Beam

The work function, cathode spot size, discharge gap, and the dielectric properties for the different regions of the dielectric media had significant effects on the simulation output. These effects are described in greater detail in chapter 6 to demonstrate how these different parameters affect the current density and electron temperature results. The simulation results in this chapter are for the validated simulation results. The inputs used in the simulation to achieve these results are included in Table 5-2

Table 5-2: Simulation Inputs

Model Attribute	Properties	Copper
Electrical	Work Function (eV)	4.4
	Cathode Spot Temperature (K)	4,000
	Emission Constant (A/cm^2K^2)	120
Boundary Conditions	Cathode (V)	-72
	Anode (V)	0
Cathode Spot	Size (mm)	1
	Discharge Gap (mm)	1
Plasma Bubble	Relative Permittivity	92
	Conductivity (S/m)	9
Plasma/Slurry Transition	Relative Permittivity	85, 88
	Conductivity (S/m)	3, 5
Slurry	Relative Permittivity	82
	Conductivity (S/m)	0.01

As noted previously, it is expected that the beam induced magnetic field should have a significant effect on the primary electron beam (Boxman, Martin and Sanders 1995) (Elliot 2009). Figure 5-8 shows a representation of the trajectories of a typical primary charged particle beam (electrons, protons, neutrals, and positive ions) for copper without including beam induced magnetic effects (Biot-Savart).

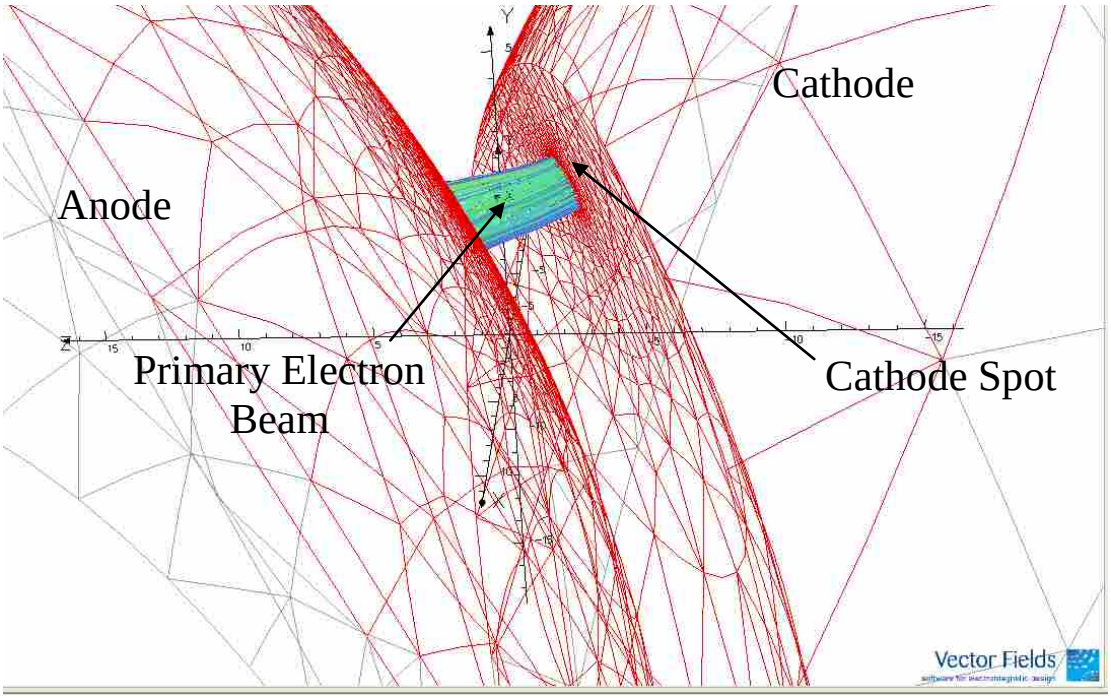

Figure 5-8: Primary Beam of a Copper Discharge

There are a number of problems with this primary electron beam. First, there is no evidence of the formation of a cathode sheath. The cathode sheath should demonstrate significant particle acceleration across a short region and a rapid potential change (Wendelstorf 2000). This beam has an almost linear acceleration across the gap. There is a uniform potential change across the gap as well. Second, as result of the weak acceleration, the current density remains nearly constant between the cathode and anode spots which has no correspondence to experimental anode spots. Third, the current density map for the anode spot is nearly uniform and is slightly larger than the cathode spot. This does not match up with any experimental result. Therefore, this model with no beam induced magnetic fields does not accurately simulate the underwater discharge.

Figure 5-9 shows the primary beam with the beam magnetics included in the simulation. Figure 5-10 shows a close up view of the primary beam to discuss the features of the beam.

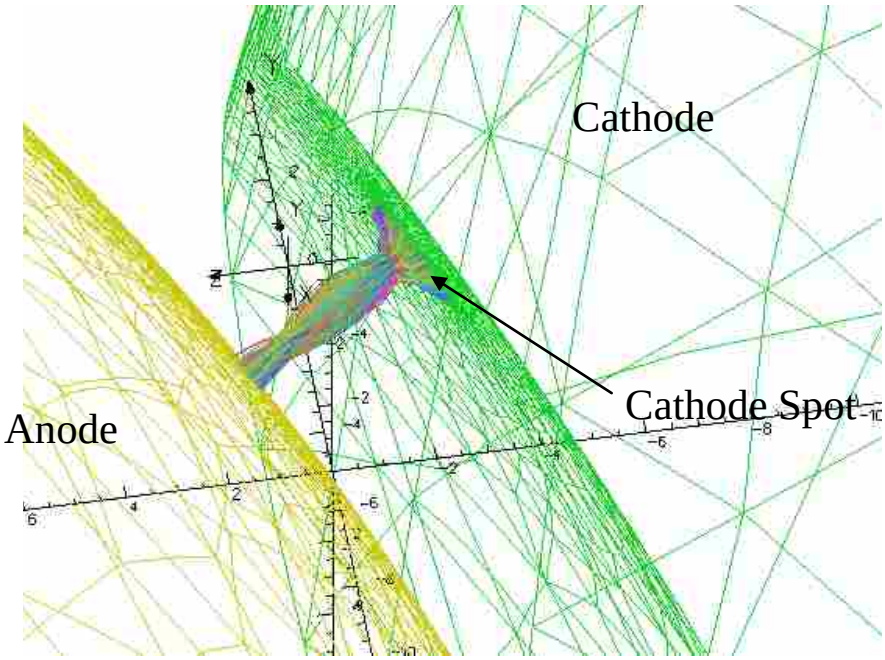

Figure 5-9: Primary Copper Beam with Beam Magnetics

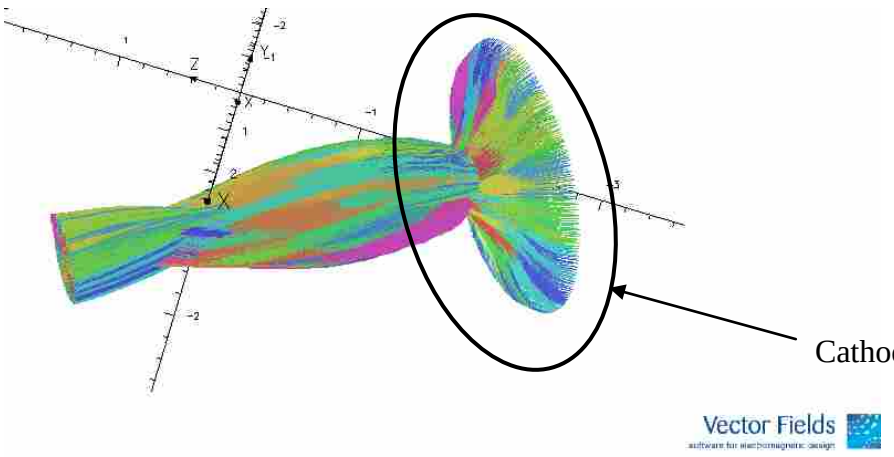

Figure 5-10: Primary Beam

This beam has all of the features that were missing from the beam when the magnetics were neglected. The cathode sheath is present with an order of magnitude acceleration of the electrons, a length less than 0.1 mm (as measured by the length required to reach an order of magnitude acceleration, which corresponds to the point where the beam begins to wrap around itself), and a large potential change across the sheath region.

Another important finding is the shape of the sheath region itself. Researchers who study constricted arcs have postulated that there should be significant beam constriction in sheath from the space charge, the dielectric media, the beam induced magnetic fields, and the emission characteristics of the arc (Boxman, Martin and Sanders 1995) (Harris 1980) (Elliot 2009). The simulation clearly shows this phenomenon and the simulation can be used to determine which input parameters have the largest effect on the sheath region formation and characteristics.

Second, the beam induced magnetic fields causes the beam to wrap around as it crosses the gap. It was found that the material work function and the dielectric media properties dominated the shape of the beam and how much it wrapped around itself as it crossed the gap. For example, as shown in Figure 5-11, if the work function is changed from 4.3 to 4.2 the level of beam induced magnetic warping, or beam constriction, is reduced and the sheath layer length increases. There is still the expected order of magnitude acceleration in the sheath region, but the length is approximately 0.12 mm.

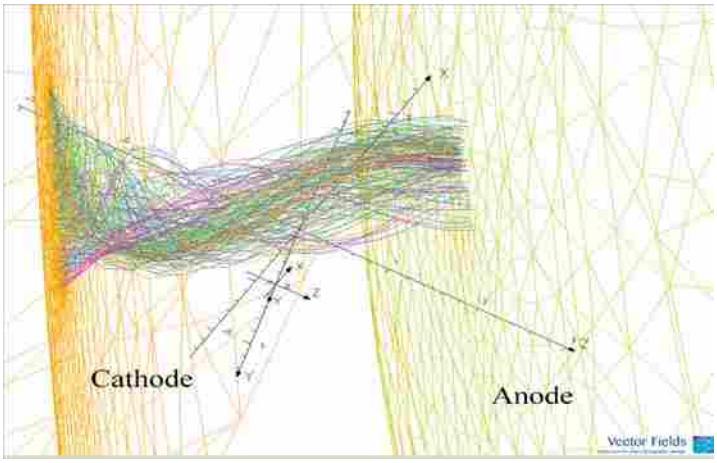

Figure 5-11: Primary Copper Beam (Work Function 4.2)

To illustrate further, using a work function of 4.3 and pure water for all the dielectric properties (permittivity = 80, conductivity $1x10^{-6}$ S/m) the primary beam will become significantly more constricted than the beam in Figure 5-10 and the cathode sheath length will decrease as shown in Figure 5-12.

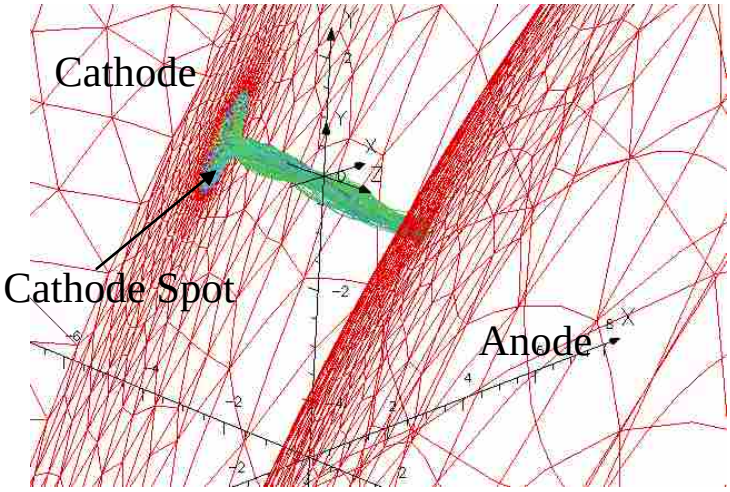

Figure 5-12: Primary Copper Beam in Pure Water

In the case of pure water, the length of the cathode sheath is reduced to less than 0.01 mm and the constriction of the beam as it crosses the gap is significantly greater than when variable dielectric properties are used.

Finally, the current density on the cathode and anode are significantly different. The cathode current density maps (Figure 5-6) shows a uniform emission as it has been defined by the emission physics and geometry. The anode current density map shows that the beam forms regions of high and low current densities. Figure 5-13 shows an example anode current density map from the primary electron beam in Figure 5-9 as well as the current density associated with the secondary particle generation as the beam crosses the discharge gap.

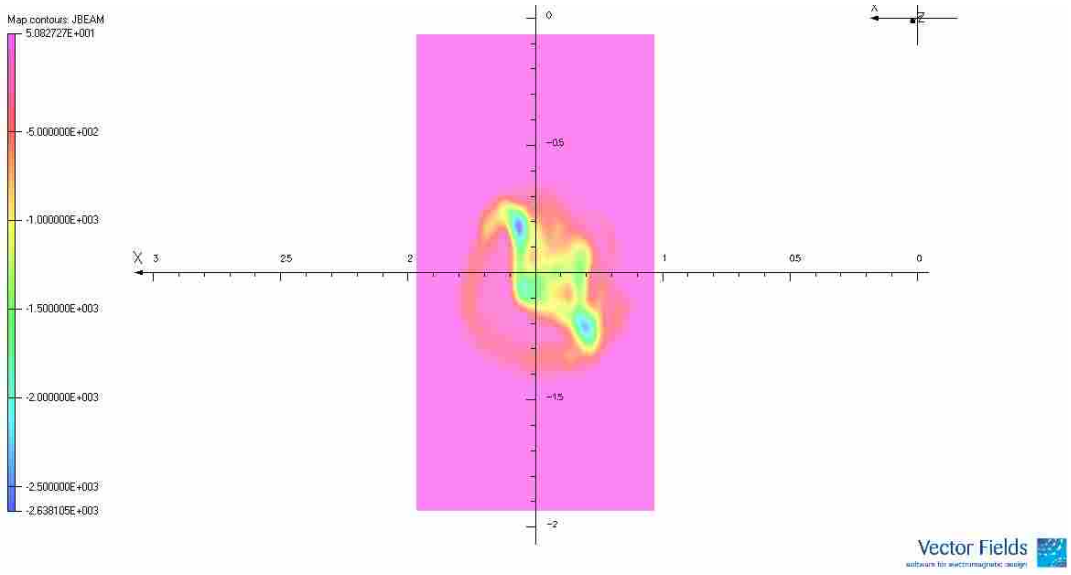

Figure 5-13: Example Anode Current Density Map

As will be described in greater detail in chapter 6, the anode current density maps are commonly used as a qualitative tool for evaluating charged particle simulations (Elliot 2009) (Simkin 2009). In this case, there are a number of non-uniform regions

between 0.1 -0.25 mm in diameter where there is a significantly higher current density. The entire anode spot fits within a rectangular patch measuring 0.5 mm x 0.6 mm. Qualitatively, if there are small regions in the anode remnants that show heavier damage, melting, or material removal, and the typical anode spot fits within the same rectangular patch then there is good correspondence between the anode current density maps and the actual anode remnants. This and other effects of the various input parameters are characterized in the discussion of the results in Chapter 6: Discussion of Experimental Apparatus Results and Simulation Validation.

5.5 Simulation Results: Volume Secondary Particle Emission

As noted previously, equation 5.18 shows the volume secondary emission fraction that was programmed into the simulation for the secondary particle generation as the primary electron beam travels across the discharge gap. The following secondary particles were simulated: electrons (representative of the interactions between the primary beam dielectric media), neutral hydrogen, hydrogen ions (H^{+1}), neutral oxygen, and oxygen ions (O^{-1}, O^{-2}). The secondary ion generation was based on the ionization energy of the various ionic species and from studies of atomic and ionic species generated in an underwater discharge (Lide 2007-2008) (Patnaik 2004) (Fulton 1986) (International Institute of Welding 1983) (Lancaster 1986) (Lan et. al. 2009).

Hydrogen does not react with copper and will only reformulate into water molecules with oxygen ions or will recombine into elemental hydrogen gas and leave the system. Neutral oxygen is noted as being an atomic formulation from a discharge (Lan,

et al. 2009). However, its presence is almost negligible compared to hydrogen in gas analysis from underwater discharges (Descoeudres 2006). Therefore, there should be electrons, neutral hydrogen, hydrogen ions (+1), neutral oxygen, and oxygen ions (-1, -2) resulting from an underwater discharge. The formation of these materials can be simulated using volumetric secondary emission in the discharge gap as the primary beam interacts with the dielectric media in the gap. The simulation can be programmed to estimate emission of any element and charge state. This section presents the results of secondary particle emission of the species of interest from the simulation.

The first species of interest is the secondary emission of electrons. As the primary electron beam passes through the discharge gap the energetic electrons influence the water molecules. Because energy is conserved, the water molecule and the passing electrons must have a change in state. Water disassociates and the resulting oxygen and hydrogen atoms can become ionized. The result is a net increase of free electrons along the beam path. Figure 5-14 shows the simulation results for the secondary electron emission from the primary electron beam.

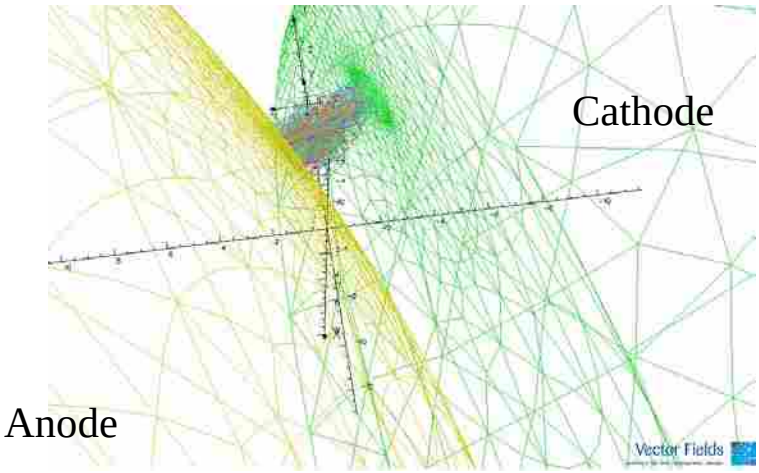

Figure 5-14: Secondary Electron Emission

Secondary electron emission does not occur until the electrons have passed beyond the cathode sheath. Until the electrons are able to overcome the space charge through acceleration in the sheath, there is not enough energy to produce secondary emission. Once clear of the sheath, secondary emission begins. The secondary electron particles are drawn across the gap through electromagnetic attraction to the anode surface. These secondary particles are what create the ring effect on the anode current density map shown in Figure 5-13.

The next species of interest are formed with hydrogen. As noted previously, hydrogen has been shown to only form the elemental hydrogen and the H^+ ion in solution (Lan, et al. 2009). It is anticipated that the majority of the hydrogen ions reformulate to hydrogen gas or water molecules while some will remain in solution creating a slightly acidic slurry (Descoeudres 2006) (Lan et. al. 2009). Similar to Descoeudres, gas bubbles formed on the surface of the cathode without the presence of a discharge as shown in Figure 5-15. Descoeudres notes that the gas is primarily hydrogen caused by electrolysis as measured through gas analysis.

Figure 5-15: Pre-Breakdown Bubble in Case Study

The ph of the slurry was constantly measured during experiments with the experimental apparatus. The slurry became slightly acidic over time indicating the presence of dissolved hydrogen ions. These findings support the results of Lan and Descoeudres. Therefore, the simulation includes secondary emission of both neutral and ionic hydrogen. The neutral hydrogen particle trajectories are shown in Figure 5-16. The simulation of the hydrogen ion trajectories are shown in Figure 5-17.

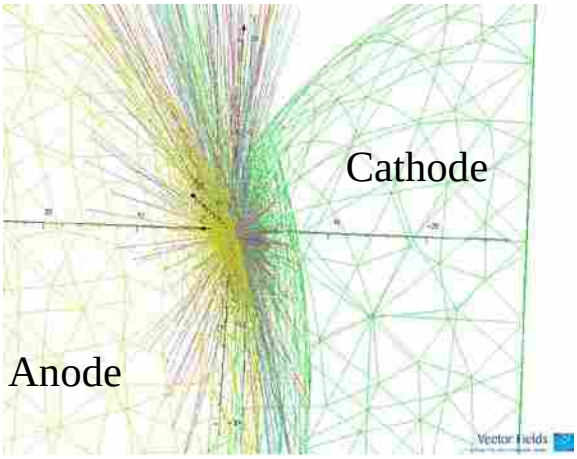

Figure 5-16: Simulation of Neutral Hydrogen Trajectories

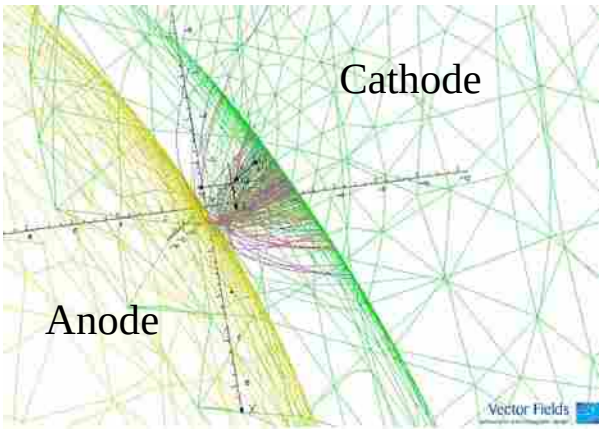

Figure 5-17: Hydrogen (+1) Ion Trajectories

As would be expected, the neutral hydrogen is not attracted to any charged surface and is ejected into the surrounding media. In the physical system this is represented by the bubbles that are generated in the discharge. The simulated hydrogen ions are attracted to the negatively charged cathode as the particles are naturally drawn back to the cathode.

The last species generated in underwater discharges are formed by oxygen. As noted previously the oxygen species that form are elemental oxygen and two ions (O^{1-}, O^{2-}) (Lan et. al. 2009). While it is possible that higher order ions are formed, they are so volatile that they will rapidly react to a more stable ion state. The neutral oxygen will behave just like the neutral hydrogen and be ejected into the surrounding media as shown in Figure 5-16. Figures 5-18 and 5-19 show the oxygen ion trajectories from the simulation for the two ion states.

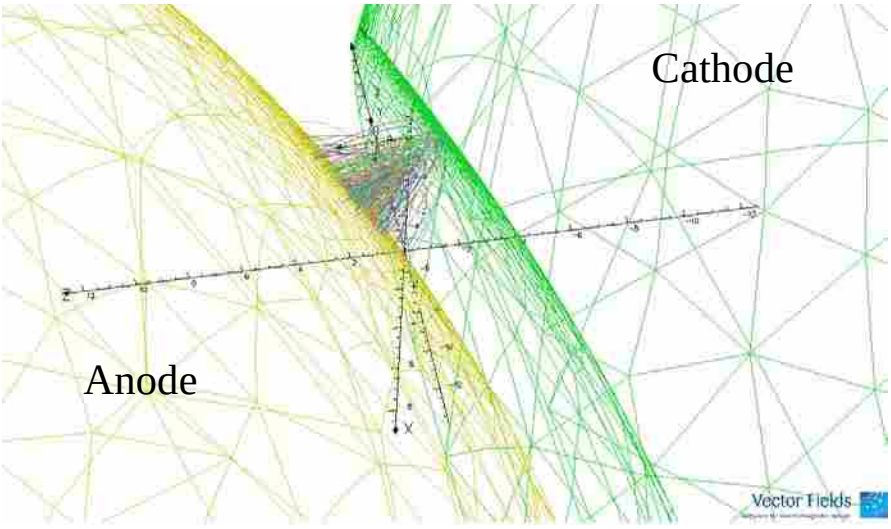

Figure 5-18: Oxygen (-2) Ion Trajectories

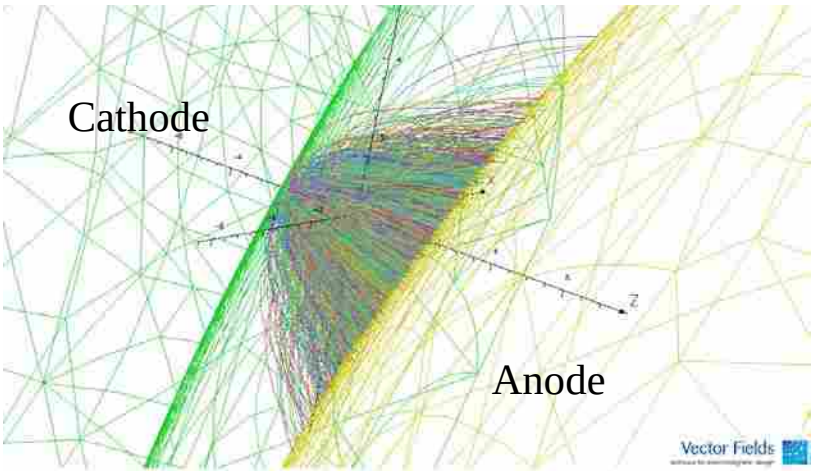

Figure 5-19: Oxygen (-1) Ion Trajectories

The oxygen ions are drawn to the positively charged anode and the lower ionization of oxygen has more than double the ion content as the higher oxygen energy state (-2). Oxygen (-1) is a stable ionization state for oxygen and has an ionization energy less than half of oxygen (-2) (Lide 2007-2008) (Chemglobe 2009). A more detailed discussion of these results will be included in Chapter 6.

5.6 Simulation Results: Anode Emission Phenomena

Both backscatter and secondary emission were included with the anode analysis. As the primary beam strikes the surface of the anode, the majority of the energy will be absorbed as heat causing melting, vaporization, and erosion of the anode. However, there will also be some small fraction of incident particles that are backscattered from the surface, and there will be some copper ion secondary particles generated. Literature and experimental results from the process machine indicate that the most common secondary ions will be Cu^{+} and Cu^{++}. It is possible that higher order ions could be generated, but since they are not stable ion states they will rapidly revert to one of these stable ion states.

Backscattering was simulated with an energy loss distribution with a maximum energy of 85% of the incident particle and a cos(θ) distribution. Figure 5-20 shows the backscattered electron trajectories for the simulation.

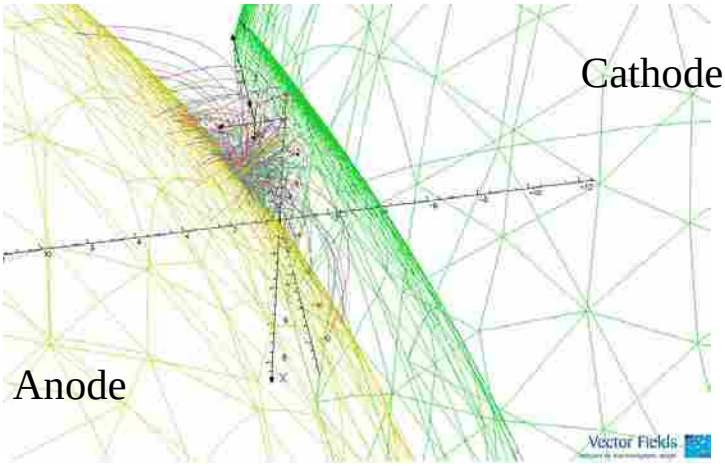

Figure 5-20: Backscattered Electrons from the Anode Surface

The simulation predicts that all of the electrons will return to the anode surface. None have the energy to escape from the anode structure. The backscatter phenomenon is difficult to validate since the effect is so small compared to the primary beam and is difficult to separate secondary effects from each other in an experimental setup.

The only research area where backscatter and anode phenomenon have been accurately and extensively studied experimentally is in vacuum phenomena (Boxman, Martin and Sanders 1995) (Harris 1980). The energy required to create the oxygen ions which are discussed above can be used to estimate the charge states possible for copper. Both copper (+1) and copper (+2) are stable ion states and have lower formation energy states than oxygen (-2) (Lide 2007-2008) (Chemglobe 2009). Therefore secondary emission for these two copper ion states is included in the simulation of the discharge.

Figure 5-21 shows the simulation results of the copper (+1) ion trajectories and Figure 5-22 shows the Copper (+2) ion trajectories.

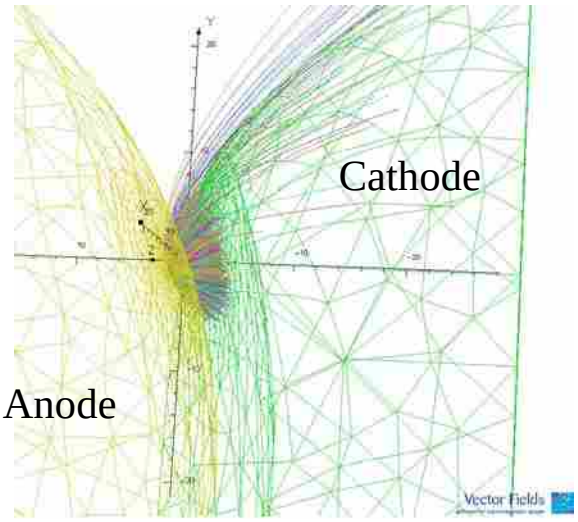

Figure 5-21: Copper (+1) Ion Trajectories

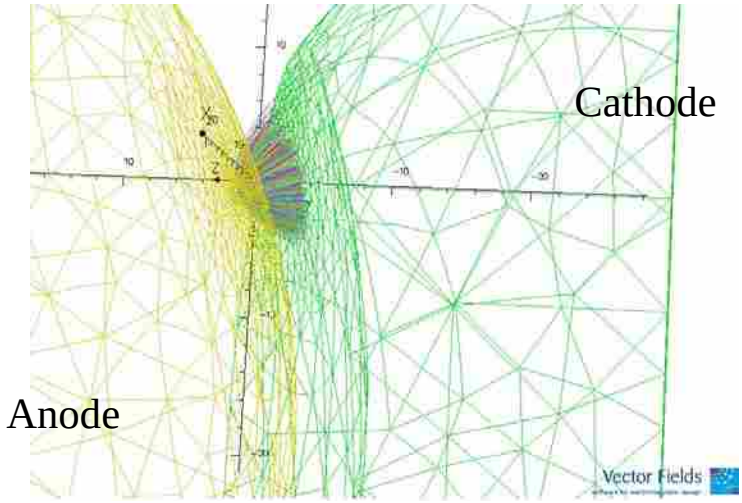

Figure 5-22: Copper (+2) Ion Trajectories

The copper ions generated are attracted back towards the cathode. The particles should be attracted to the cathode spot sheath to help neutralize the space charge and participate in the ionization within the cathode sheath (Wendelstorf 2000). This

phenomenon is called back ion bombardment. The ion bombardment can be evaluated with a current density map of the copper ions near the cathode surface which is shown in Figure 5-23.

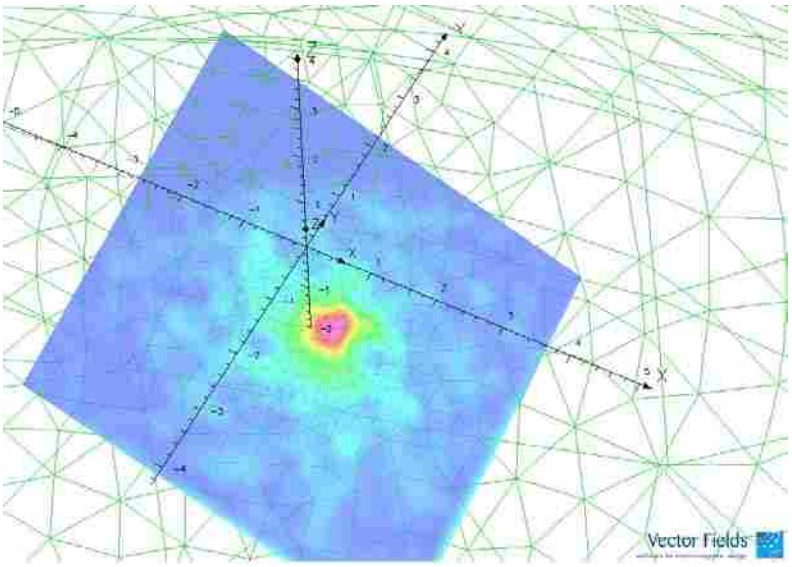

Figure 5-23: Back Ion Bombardment to Cathode

The simulation result shows that the highest concentration of positive ion bombardment is located in the cathode sheath. The outermost diameter of a theoretical circular patch containing all of the back ion bombardment is 1.6 mm in diameter.

Adding together all of the secondary particle emission and backscatter gives a complete picture of the particle trajectories for the simulation. These secondary particles describe the ionic content and can be used to determine the electrostatic characteristics of the discharge. Figure 5-24 shows the secondary particle emission trajectories without the neutral particle trajectories.

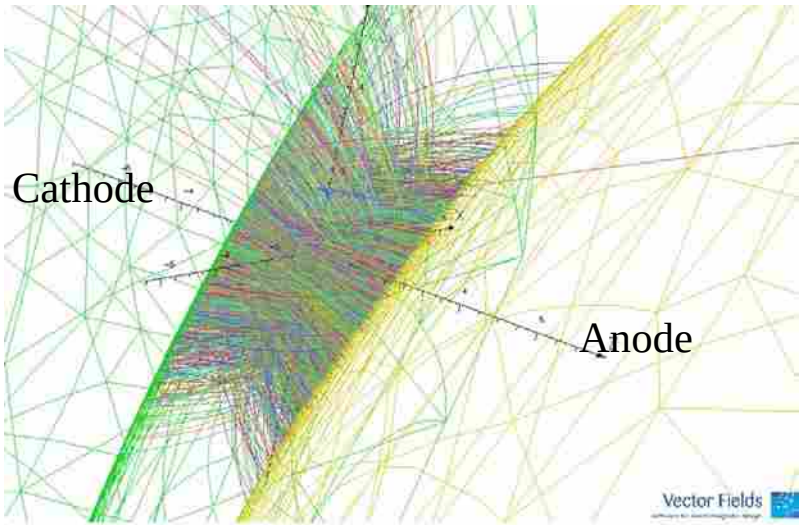

Figure 5-24: Total Secondary Particle Emission

The simulation predicts that there is a dense cloud of particles in the discharge gap generated from the secondary emission of particles made up of hydrogen and oxygen.

5.7 Chapter Summary

The inclusion of beam induced magnetic fields is required to include the necessary physics to simulate the underwater discharge. The simulation shows all of the features expected by other simulation efforts and experimental results in the literature. The cathode sheath is present with an order of magnitude acceleration of the electrons, a length less than 0.1 mm, and a large potential change across the sheath region. Additionally, the simulation shows that space charge and the dielectric media affect the length of the sheath region.

Another important finding is the shape of the sheath region itself. Researchers who study constricted arcs have postulated that there should be significant beam constriction in sheath from the space charge, the dielectric media, the beam induced

magnetic fields, and the emission characteristics of the arc (Boxman, Martin and Sanders 1995) (Harris 1980) (Elliot 2009). The simulation clearly shows this phenomenon and the simulation can be used to determine which input parameters have the largest effect on the sheath region formation and characteristics.

Secondary particle emission in the discharge gap and at the anode surface is also included in the simulation to form a complete picture of the particle physics of the underwater discharge.

The simulation is flexible enough to be able to study a large range of parameters with relatively low computational effort. The voltage boundary conditions, emission physics, material properties, emission properties of the system are readily varied to investigate different types of input voltages, materials, and potential fouling factors. It is now necessary to validate the simulation to determine how realistic the simulation results are compared with results from the literature and experimental measurements, and to determine the operational range of the simulation. Chapter 6 will present the validation methods, results, and the working range of the simulation input parameters.

6 Discussion of Case Study Results and Simulation Validation

This chapter describes how the simulation was validated. The simulation validation is separated into the tools used to validate the primary electron beam and tools used to validate the secondary particle emission. Following this discussion the operational range of the simulation will be presented.

The simulation validation compares the simulation outputs to published literature and experimental results from the case study. The operational range was determined by varying the simulation inputs and observing how they affect the simulation outputs. The key simulation outputs are:

- Anode current density
- Total current
- Electron temperature
- Cathode sheath parameters (length, electron acceleration, and space charge)
- Secondary particle generation

6.1 Simulation Validation

The simulation validation is separated into two sections. The first describes the validation of the physics of the primary electron beam. The primary beam dominates the

discharge physics and there are a number of characteristics of the primary beam that can be compared to experimental results using the process machine and published results for similar discharges in the literature. The second section describes the validation of the secondary particle generation.

6.1.1 Primary Beam Validation

There were three tools used to validate the physics described by the primary electron beam in the simulation:

1. Anode current density maps vs. experimental anode spot remnants
2. Simulation electron temperature vs. published electron temperature data
3. Simulation total current vs. experimental total current

The first tool is largely qualitative and is used as a gage to determine if the beam has believable physical characteristics. The second tool is the key validation tool. There is a large body of literature of experimentally determined electron temperature values for copper electrodes in underwater discharges. The simulation can be used to directly calculate the electron temperature distribution of the beam for direct comparison to the literature. Finally, the total current from the simulation can be compared to measurements of the experimental process machine and also to the literature.

6.1.1.1 Current Density Maps vs. Anode Spot Remnants

The technique described in this section is a qualitative tool that is commonly used to evaluate the primary beam physics of charged particle simulations (Elliot 2009). Qualitatively, if the current density map of the simulation contains the same general

structures as the actual anode spot remnants, the simulation is considered to have good correspondence with experimental results. The structures that are being evaluated are the total size of the affected region (anode spot), and the size and distribution of areas of high energy deposition. Areas of high energy deposition typically should correspond to regions of heavier material removal, damage, melting, and/or secondary emission.

To compare structures between the simulation and the experimental results, a current density map at or near the anode surface is used to determine the beam distribution of energy on the anode. The current density map can contain the primary beam, secondary particles, or all incident particles on the anode that deposit energy into the anode.

Thirty anode spot remnants from controlled experiments were investigated with 100X to 1000X magnification to provide a clear view of the macroscopic anode remnant structures of single discharges. The affected area of the spots is irregularly shaped with no readily identified patterns from the images. These thirty images were evaluated using the image processing software Image J, to determine the size of the total affected area and the size and shape of the areas of heavier damage/erosion that occur from the discharge. The data was analyzed using MiniTab V15. Figure 6-1 shows the distribution of the total affected area of the anode spots from the thirty images.

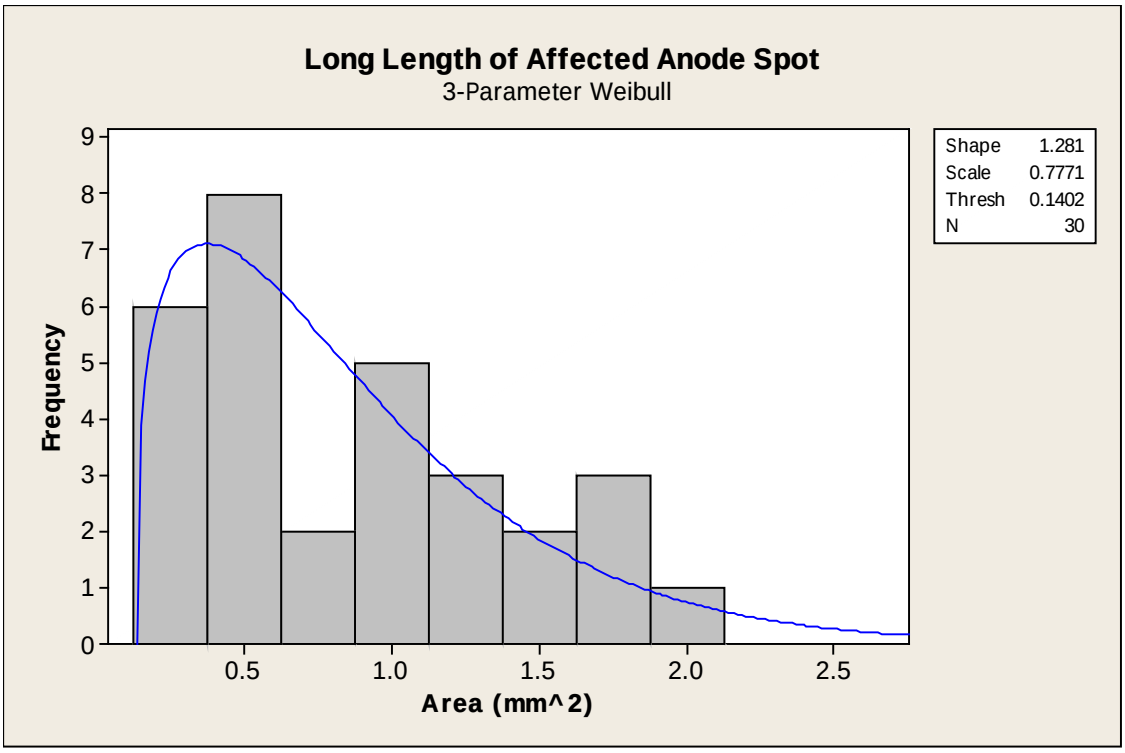

Figure 6-1: Histogram of the Affected Area (Anode Spots)

The data of the total affected area of the discharge was found to be non-normal. The best fitting distributions were extreme value distributions. The highest ranking fit was a 3 Parameter Wiebull distribution with a shape factor of 1.281 as shown in Figure 6-1. Data from breakdown studies of solid and liquid dielectrics and discharges in general have been found to be better fit by extreme value statistics like a Wiebull distribution (Goshima, et al. 1996). The affected area of all anode spots measured can fit within a 2mm x 2mm square patch on the surface of the anode and average spot will fit in a rectangular patch measuring 0.75 mm x 1 mm. The average area of a spot is approximately 0.87 mm^2. The maximum affected area measured was 1.96 mm^2.

All of the anode spot images have at least one smaller area within the affected area that has significantly higher damage or erosion. The higher erosion areas are

roughly circular ranging between 0.1 - 0.25 mm in diameter. Figure 6-2 shows the size distribution of the heaviest areas of damage of the anode remnants.

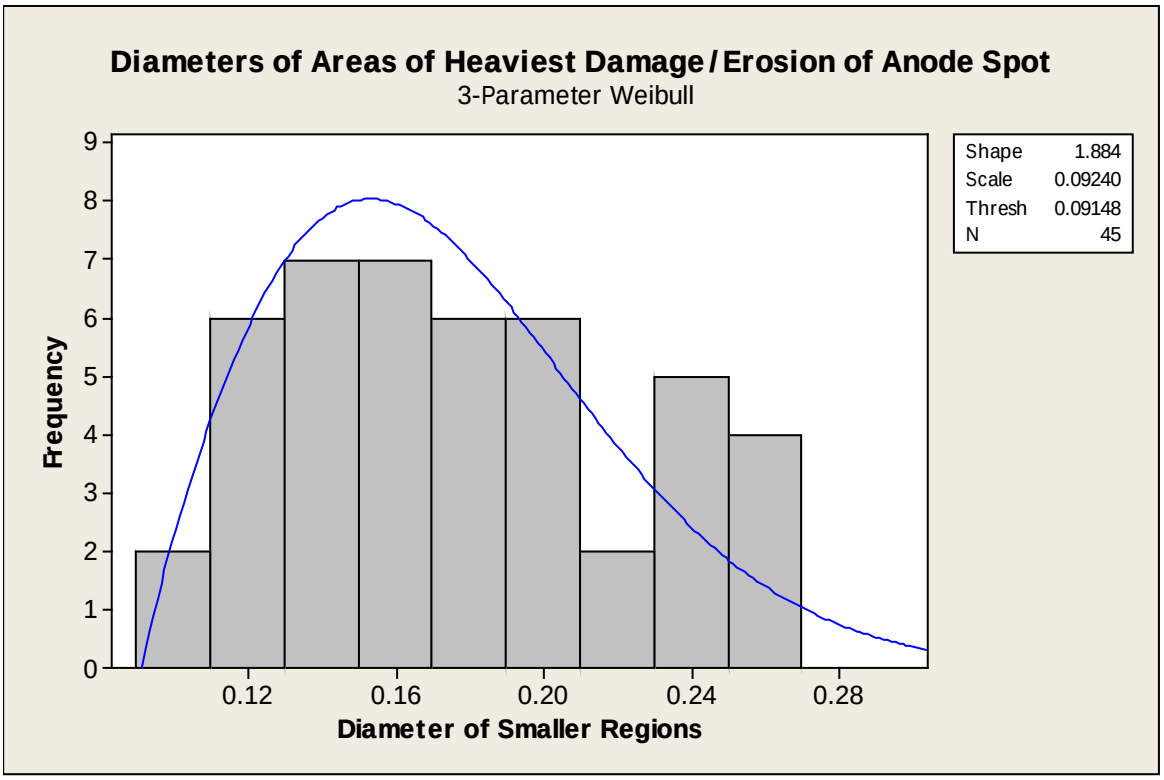

Figure 6-2: Histogram of the Diameters of Areas of Greatest Erosion

Like total area, a 3 parameter Wiebull distribution had the best fit for the data. The heavily erosion areas also have a wide range of affected depths as can be seen in Figures 6-3 to 6-5. These images show examples of the range of the cathode spot remnant images obtained from experiments with the experimental process machine. It can be seen that there is not a clear pattern to the affected areas and that the depth of the erosion varies widely between the three images.

Figure 6-3: Example Anode Spot (1)

Figure 6-4: Example Anode Spot (2)

Figure 6-5: Example Anode Spot (3)

To show correspondence with the experimental results, the anode current density maps obtained from the simulation should contain non-uniform regions with the total affected area no larger than 2 mm^2 and be able to fit in a maximum of 2 mm x 2 mm patch. There should also be regions of significantly higher current density that are roughly circular that measure between 0.1 - 0.25 mm in diameter with significantly higher current density. Figures 6-6 through 6-8 provide three examples of anode current density maps from simulation runs with the same emission inputs, but different dielectric properties.

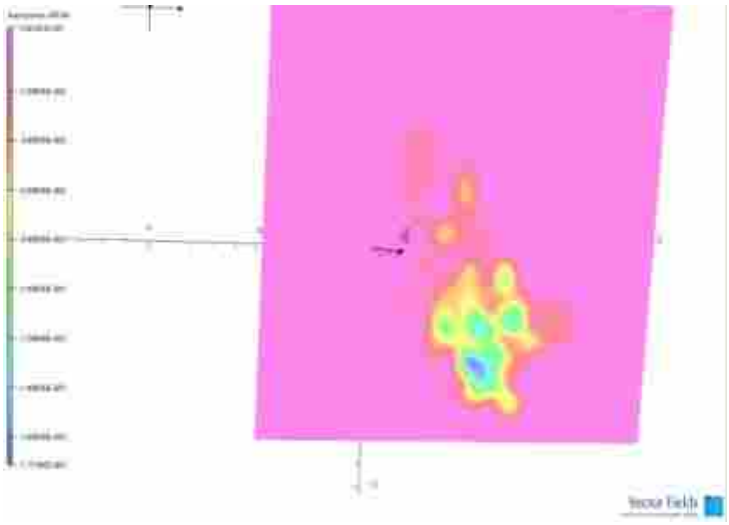

Figure 6-6: Example Current Density Map

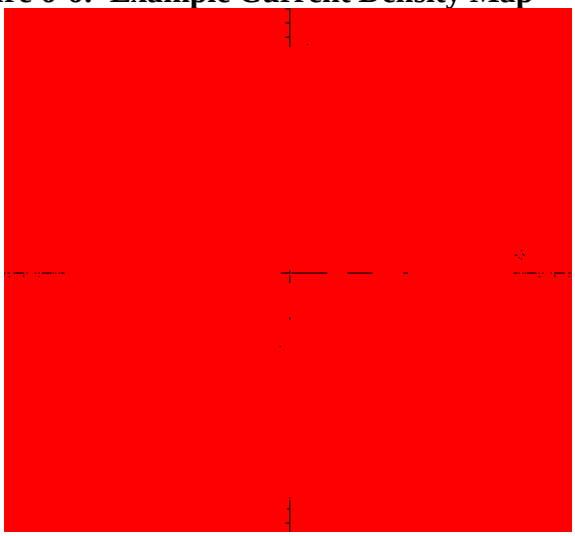

Figure 6-7: Example Current Density Map

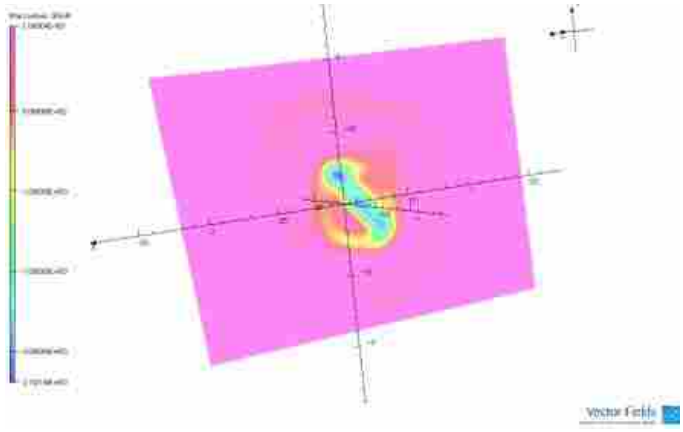

Figure 6-8: Example Current Density Map (Including Secondary Particles)

The simulation predicts that there will be a non-uniform spot with at least one region with significantly higher current density. The primary beam shows that the affected area fits within a 1 mm x 1mm area. The areas of highest current density (blue and blue-green) are less than 0.4 mm in the longest dimension and are mostly circular. Even when all emission sources (primary and secondary) are included, the affected area fits within 2 mm x 2 mm rectangular patch.

To compare directly between the anode spot images and the simulation results, the distributions of the total affected area and longest dimension of the regions of heaviest damage or current density were used. The number of current density maps used in the analysis was four. It was assumed that the distribution of the area should be the same as the anode spots so a 3 parameter Wiebull distribution was used. Figure 6-9 shows a comparison between the distribution of the affected area of the anode spot derived from the microscope images and the simulation current density maps.

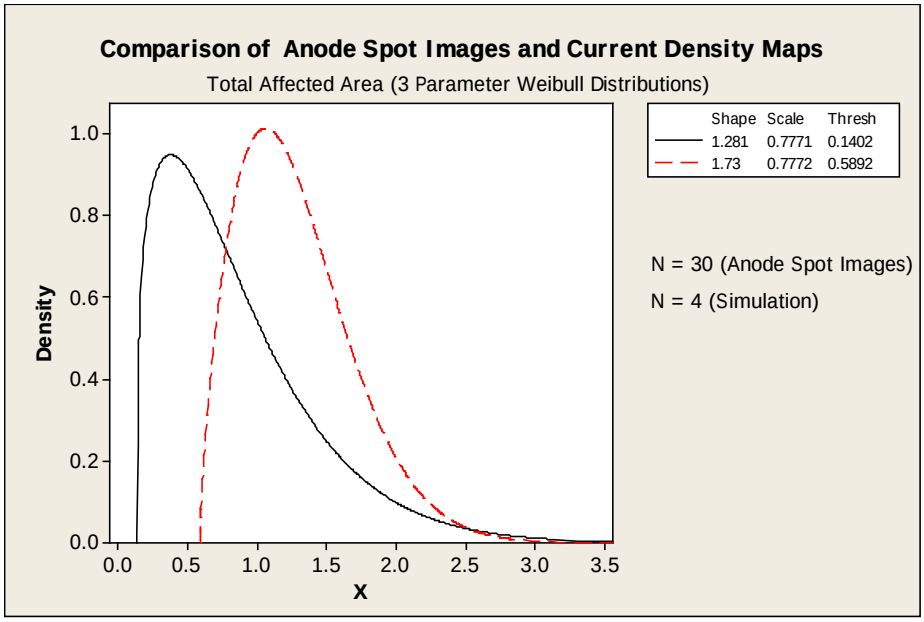

Figure 6-9: Distribution Comparisons of Anode Spots and Current Density Maps

The threshold parameter indicates the smallest recorded value for the output of interest. The smallest anode spot from the electrode images was 0.140 mm^2 whereas the smallest spot size from the simulation was 0.589 mm^2. This accounts for the shift between the two distributions. The shape and scale parameters define the distribution. Both parameters are very similar to each other resulting in similar distribution functions. Therefore the simulation predicts a slightly higher average affected spot size than the actual images, but the distributions are reasonably well correlated to each other.

Similarly the size of the areas of highest erosion and the areas of highest current density can be studied. In this case the sample size for the simulation is higher since there are multiple regions in each image. The total sample for the simulation is 11 while the total sample for the images is 45. Figure 6-10 shows the comparison of the diameters of the regions of highest current density (simulation) and erosion (spot images).

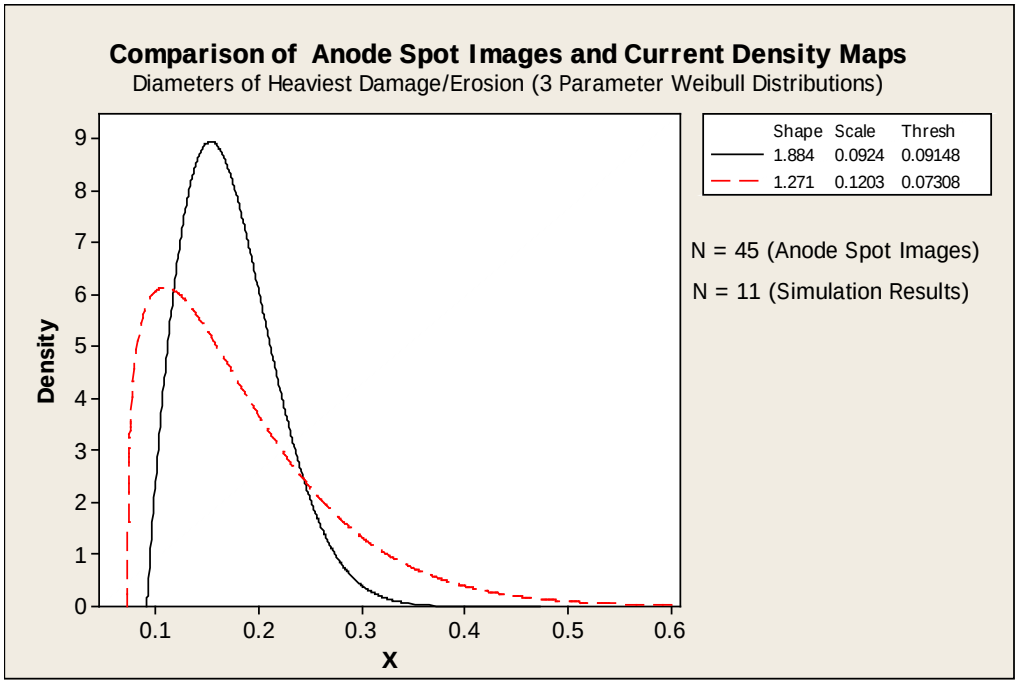

Figure 6-10: Distribution Comparisons of Anode Spots and Current Density Maps

The threshold between these two distributions is very similar, showing that the smallest size measured is equivalent in both groups. The current density maps indicate areas of highest current density to be slightly larger than the actual remnants on the anode spot images but have similar distribution shape parameters. Therefore, there is a strong correspondence between the structures of the anode current density maps and the anode remnants from the experimental process machine.

6.1.1.2 Electron Temperature

There are a number of examples in the literature describing the measurement of electron temperature in underwater discharges with copper electrodes (Komolov and Rachovsky 1992) (Jones and Kunhardt 1995) (Korobeinikov and Melekhov 2002) (Aka-Ngnui and Beroual 2001) (Descoeudres 2006) (Nakamura, et al. 2009) (Namihira, et al. 2007). The literature focuses on EDM and high voltage pulsed discharges. Descoeudres noted that for EDM discharges (which are similar to the process machine discharge in this case study) the experimentally determined electron temperature was consistent during his experiments with an average of 0.7 eV (Descoeudres 2006).

Experimentally determined electron temperature is determined using spectroscopy methods, such as 2-color pyrometry or optical emission spectroscopy (Namihira, et al. 2007) (Descoeudres 2006). These spectroscopy methods measure the wavelengths of the emitted light spectra for a particular material (usually the cathode material). The wavelengths can then be used to estimate the electron temperature of the discharge.

As noted by Namihira, there are virtually no examples in the literature describing numerical simulation efforts to determine electron temperature of underwater discharges

(Namihira, et al. 2007). In order to calculate electron temperature the velocity of the electrons must be known. Since the literature typically approaches discharges from a plasma physics perspective rather than a particle physics perspective, it is difficult to determine or simulate the velocity of the electrons. However; this is a readily obtained output from the Vector Fields simulation. It is also one of the most powerful simulation outputs because it can be directly compared to experimental data.

The electron temperature of a discharge is directly related to the kinetic energy of the electrons in the plasma (Komolov and Rachovsky 1992) (Descoeudres 2006). If the velocities of the electrons in the discharge plasma follow a Maxwell or Maxwell-Bolzmann distribution the electron temperature can be directly calculated using the kinetic energy and thermal energy of the electrons (Vladimirov, Ostrikov and Samarian 2005). The kinetic energy of an electron can be calculated by:

$$E_{e,\,kinetic} = \frac{1}{2} m v^2 \qquad \textbf{(6.1)}$$

Where:

$E_{e,kinetic}$ (J) is the kinetic energy of an electron or group of electrons

m (kg) is the mass of an electron

v (m/s) is the velocity of the electron or group of electrons

The thermal energy of an electron (with three translational degrees of freedom) in a Maxwell-Boltzmann distribution is (Vladimirov, Ostrikov and Samarian 2005):

$$E_{e,\,thermal} = \frac{3}{2} k T_e \qquad \textbf{(6.2)}$$

Where:

$E_{e,\,thermal}$ (J) is the thermal energy of an electron or group of electrons

k (J/K or eV/K) is the Boltzmann constant

T_e (K or eV) is the electron temperature

Combining 6.1 and 6.2 an expression for the electron temperature based on electron velocity can be obtained:

$$T_e = \frac{1}{3k} m v^2 \tag{6.3}$$

Therefore, if a velocity profile can be defined for the discharge, the electron temperature can be calculated directly from the simulation. Vector Fields treats the velocity of the electrons in all simulations as following a Maxwell velocity distribution (Vector Fields 2008-2009). Two velocity profiles of the primary electron beam as calculated from the simulation are shown in Figure 6-11 and Figure 6-12.

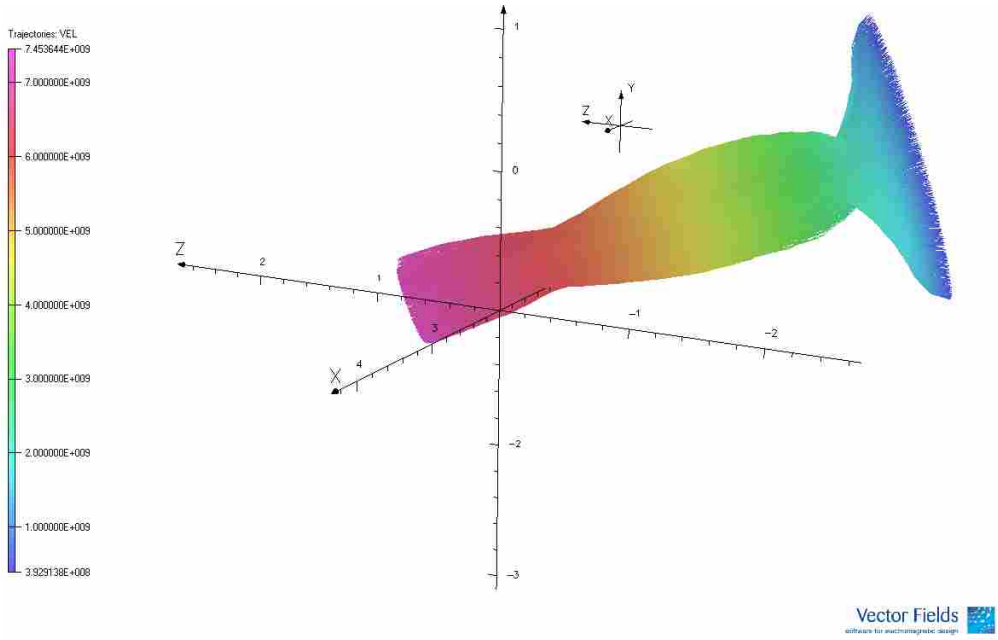

Figure 6-1: Example Velocity Profile of a Primary Electron Beam

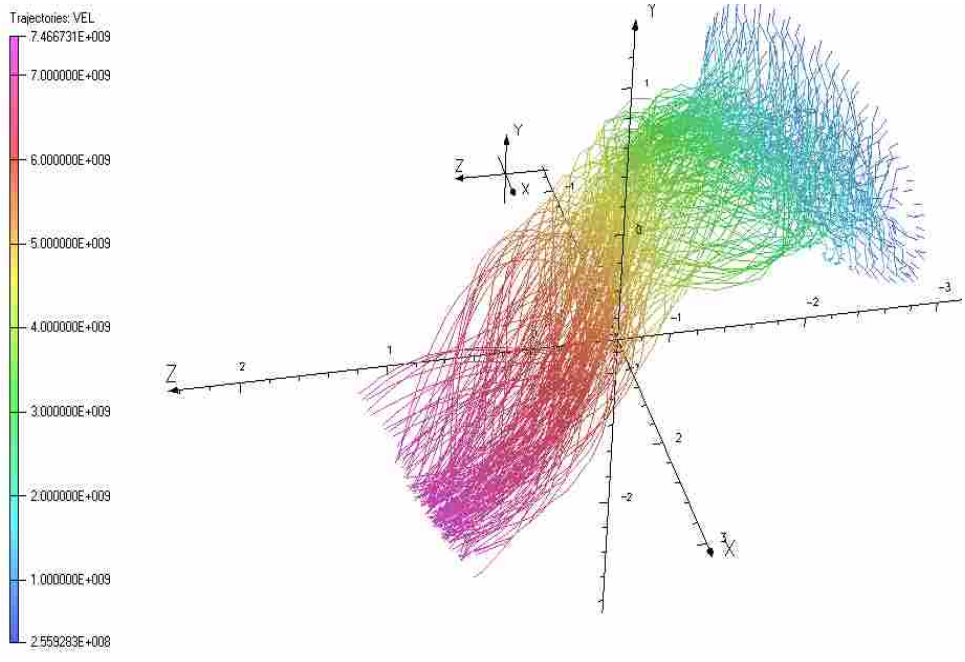

Figure 6-12: Example Velocity Profile of a Primary Electron Beam

There are only two differences between the simulations in these two images, the number of tracks in the image and the dielectric properties. Figure 6-11 contains three times as many tracks for special resolution as Figure 6-12. The dielectric properties are closer to pure water in Figure 6-11 than for Figure 6-12. Even with these differences it can be seen that the velocity profiles have the same general characteristics. The key points from the images are:

- There is an order of magnitude acceleration across the sheath region
- The sheath length in Figure 6-9 is 0.1 mm with much more beam constriction, the sheath length is 0.18 mm in Figure 6-10 with more beam curvature
- After the sheath region there is continued acceleration across the gap
- The maximum velocity of the two simulations is equivalent

The differences in the beams and the key points from above can be seen in Figure 6-13 below. The figure shows the mean particle velocity as a function of the discharge gap.

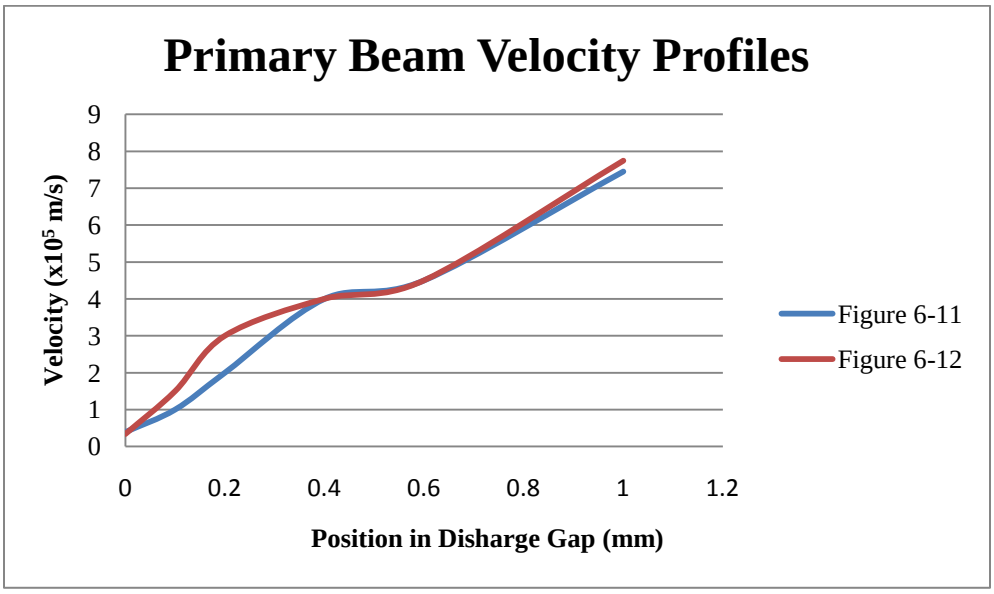

Figure 6-13: Comparison of Particle Velocity as a Function of Position

The sheath length and the acceleration across the sheath match well to the literature (Fridman and Kennedy 2004) (Wendelstorf 2000). Boxman and others have postulated that in a discharge in a dielectric media that there should be a constriction of the arc and there should be significant beam induced magnetic effects (Boxman, Martin and Sanders 1995) (Harris 1980). The particle physics in the presence of an electric field and beam induced magnetic fields do, in fact, cause constriction of the primary beam. The dielectric constant and conductivity of the dielectric media have the largest effect on beam constriction.

Since the acceleration of the particles crossing the gap is not linear, to find the mean velocity will require sampling the velocity at multiple points across the gap and taking the average velocity. The individual velocities of the particles can be obtained

with a velocity density map. In order to determine a mean velocity, and thus the mean electron temperature, 10 velocity density maps from 0.1 mm to 0.75 mm of the discharge gap were used to determine the velocity distribution for the primary electron particle beam and secondary electrons generated. Figure 6-14 shows a histogram of particle velocities from the 10 velocity maps for the discharge shown in Figure 6-12.

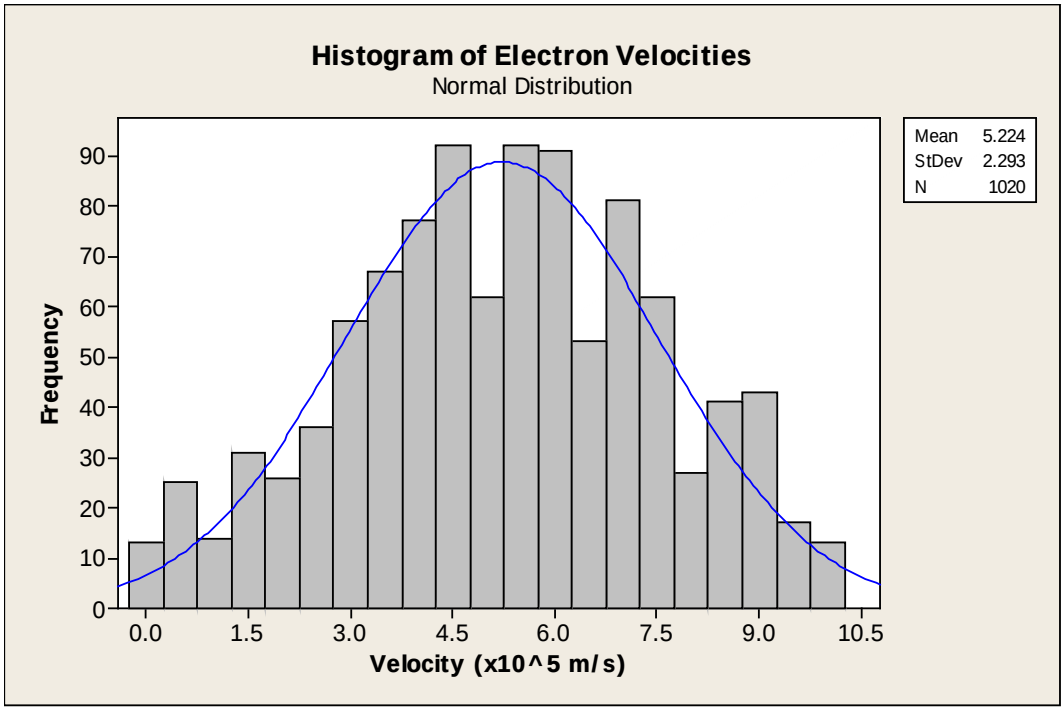

Figure 6-14: Velocity Distribution from a Velocity Density Map

The mean velocity of the primary and secondary electrons in the simulation is 5.224×10^5 m/s which results in an electron temperature of 6,000 K or 0.51 eV,

Similar analysis of a number of other simulation runs using various dielectric properties showed that the average electron temperature ranges from 0.46 eV to 1.1 eV.

As noted previously, EDM and high voltage pulsed underwater discharges are well researched for experimentally determined electron temperature with underwater discharges using copper electrodes. In both cases the discharge is only allowed to be present for a few microseconds though at significantly different power levels. The reported values for the electron temperature for each application are (Descoeudres 2006) (Nakamura and al 2009) (Namihira, et al. 2007):

- EDM
    - 0.4 to 1.3 eV — Range measured values using spectroscopy
    - 0.7 eV — Average reported value
- High kV Pulsed underwater discharges
    - 1.2 to 3.44 eV — Range of reported values

The simulation corresponds extremely well with the electron temperatures published in the EDM literature. There are a number of similarities between the case study discharge and EDM. For example:

- The drive voltage for EDM machines typically range from 60 to 90 volts and the discharge voltage is from 20 to 35 volts compared to 72 volts and 25 volts for the welding power supply
- EDM machines pulse the voltage supply to generate small, focused discharges that last only a few microseconds. Because of the size and rotation of the electrodes, the discharge in the process machine only lasts 3 to5 microseconds, so the discharge is constantly starting and stopping similar to an EDM discharge

Therefore, it is reasonable to postulate that the case study discharge can be compared to an EDM discharge for a single spot that is not sustained more than a few

microseconds and that the simulation predicts an accurate electron temperature profile for the discharge.

6.1.1.3 Total Current

The third tool used to validate the simulation was to compare the total current of the discharge predicted by the simulation to experimental current measurements and to the literature. There is a body of literature describing experimental current measurements of discharges in dielectric media. Peak discharge currents for pulsed underwater discharges can be a few kA, vacuum arcs can exceed 300 A, and EDM have currents listed from a few amps to hundreds of amps (Jones and Kunhardt 1995) (Namihira, et al. 2007) (Boxman, Martin and Sanders 1995) (Harris 1980) (Aka-Ngnui and Beroual 2001) (Descoeudres 2006).

A fast response current transformer (Pearson 4100) and digital oscilloscope (LeCroy Waverunner 6000A) were used to capture the discharge current profile for the experimental system. Table 6-1 shows the specifications for the current transformer.

Table 6-1: Current Transformer Specifications

Parameter	Specification
Sensitivity	1 Volt/Ampere +1/-0%
Output resistance	50 Ohms
Maximum peak current	500 Amperes
Maximum rms current	5 Amperes
Droop rate	0.09 %/microsecond
Useable rise time	10 nanoseconds
Current time product	0.002 Amp-second max*
Low frequency 3dB point	140 Hz (approximate)
High frequency 3dB point	35 MHz (approximate)

A series of controlled experiments to initiate a single discharge were used to measure the peak discharge current of a single discharge event. Figure 6-15 shows a histogram of the experimental measurements fitted to a normal distribution. And Figure 6-16 shows the range of typical current traces for single discharges.

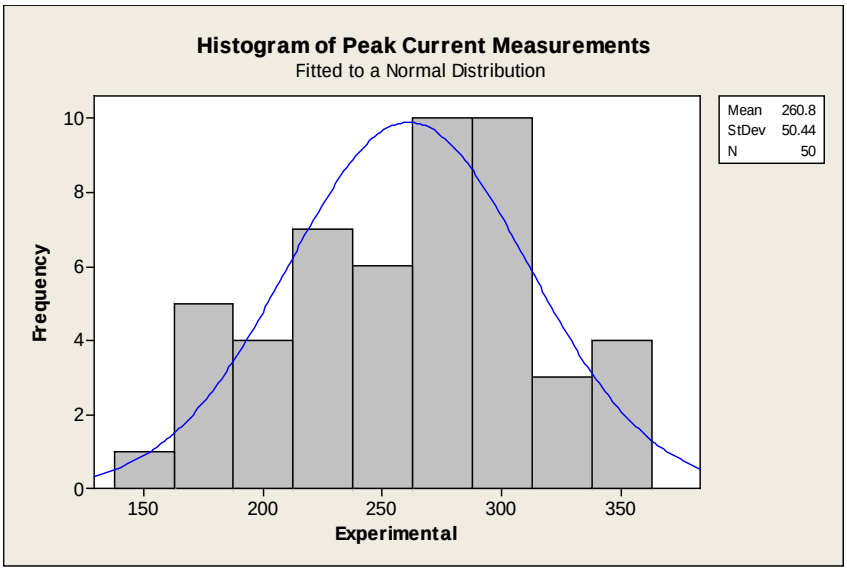

Figure 6-15: Peak Current Experimental Measurements

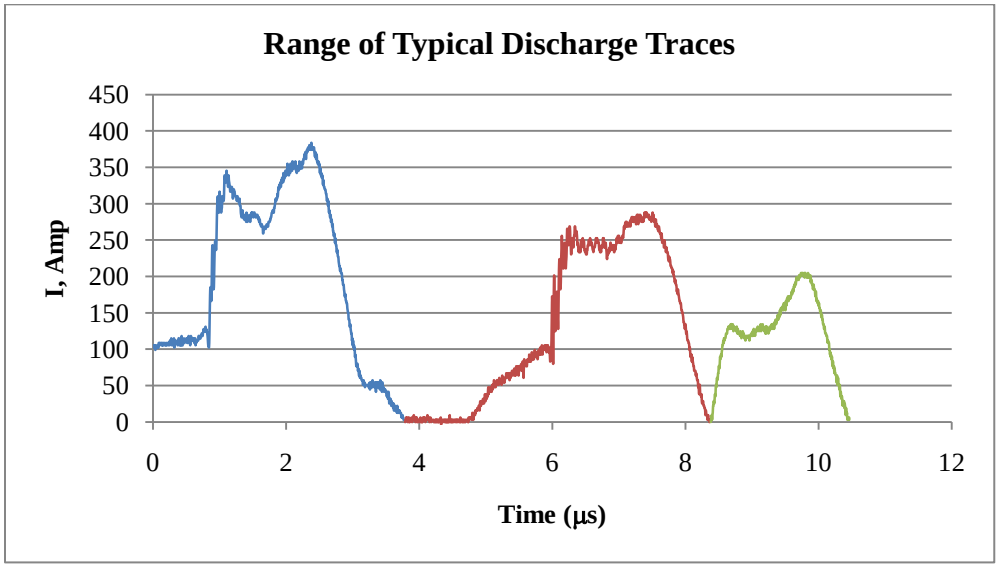

Figure 6-16: Discharge Current Traces

The following is a summary of the mean peak discharge current taken from a sample of 50 experimental measurements of a single discharge represented in the previous images.

- Total current ranged 153 to 350 Amp
- Average current = 260 Amp with a standard deviation = 50 A
- Average length of the discharge = 2.3 μs
- Not able to distinguish between single spot from multi-spot discharges

The Vector Field simulations predicted a range from 208 to 295 amps with an average total current of 224 amps in 10 simulations with the same emission characteristics but with variable dielectric properties of the slurry. Figure 6-17 compares the simulation results to the experimental results for total current.

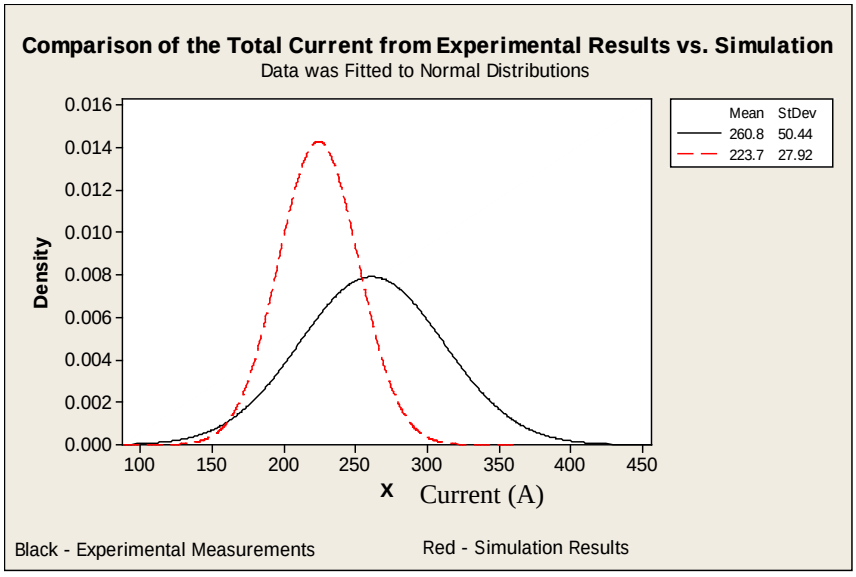

Figure 6-17: Experimental vs. Simulation Results for Total Current

The distribution from the simulation is fully contained within the experimental results; therefore, there is correspondence between the simulation, experimental, and literature for the total peak current in a single discharge.

In summary, Table 6-1 contains a summary of typical copper cathode spot characteristics from a number of sources (Fridman and Kennedy 2004) (Jones and Kunhardt 1995) (Namihira, et al. 2007) (Boxman, Martin and Sanders 1995) (Harris 1980) (Aka-Ngnui and Beroual 2001) (Descoeudres 2006):

Table 6-2: Copper Cathode Spot Characteristics

Characteristic	Value	Units
Minimum Spot Current	1.6	Ampere
Average Spot Current	100	Ampere
Current Density	10^4 - 10^8	A/cm^2
Typical Spot Voltage Drop	18	Volts
Specific Erosion (100-200 Amp Discharge)	10^{-4}	g/C
Typical Vapor Jet Velocity	$1.5x10^5$	cm/sec
Typical Work Function	4.3 4.4	eV
Length of a Single Controlled Discharge	1-4	μs
Spot Temperature	3,500 - 4,500	K

The tools used in these sections have shown that the physics of the primary electron beam of the Vector Field simulation have strong correspondence and agreement with the literature and with experimental results.

6.1.2 Secondary Particle Validation

There were three tools used to compare the simulation results of the secondary particle generation to the literature and experimental results:

1. Comparison of the secondary particle distributions to literature of species generated in an underwater discharge
2. Comparison of secondary particles to compounds found in the slurry from the experimental process machine
3. Comparison of the secondary particle "cloud" to high speed images of the discharge in the experimental process machine

6.1.2.1 Comparison of Secondary Particles to Species Literature

Lan performed a study to compare species generated in an underwater pulsed discharge to a numerical simulation using first principles (Lan, et al. 2009). They had good agreement between the simulation and the experimental results. One of the key results of the study was the time evolution of the particle density of various species over time.

The Vector Field simulation will not directly provide time evolution data as the simulation is an electrostatic solution. However, we can obtain a particle density distribution function of each of the simulated particles to determine if the same ratio of particle densities is achieved in the VF simulation as in results for Lan et.al. Figure 6-18 shows the time evolution of particle density from Lan (Lan, et al. 2009).

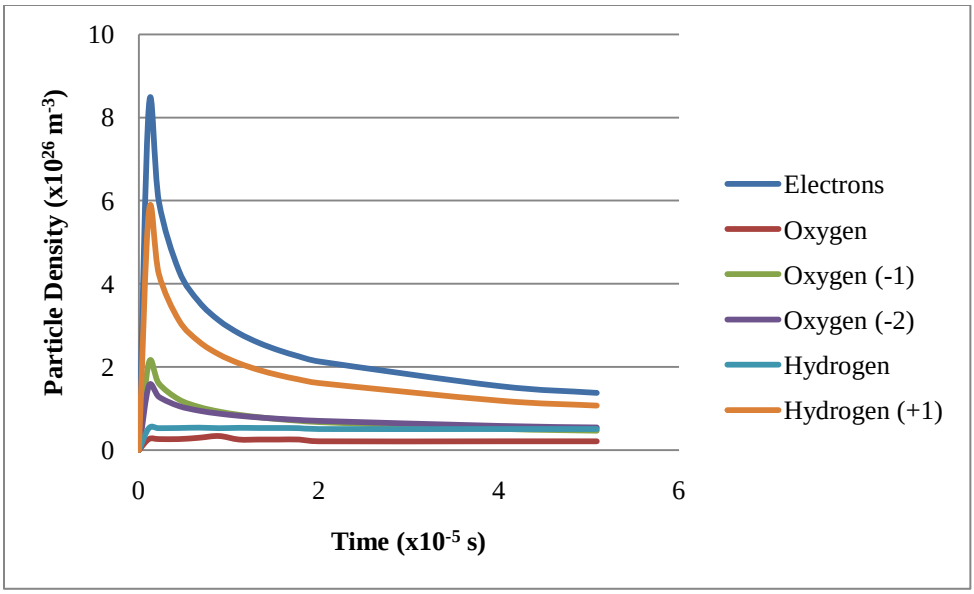

Figure 6-18: Time Evolution of Species Particle Density

The following analysis is based on using the simulation discussed in Chapter 5 to compare species content. The simulation can output the total number of particles by emitter type. Since the individual species are simulated by an individually defined emitter (in this case volume secondary emission physics), each species can be individually accounted for and a total number of particles can be obtained. The total number of particles in the simulation is 3,522. Figure 6-19 shows the histogram for the species distribution of particles.

As expected, the electrons dominate the simulation. The electrons come from two emitters: the primary beam and the volume secondary emission. The primary beam contained 964 electrons and the volume secondary emission accounted for 657 electrons in the simulation.

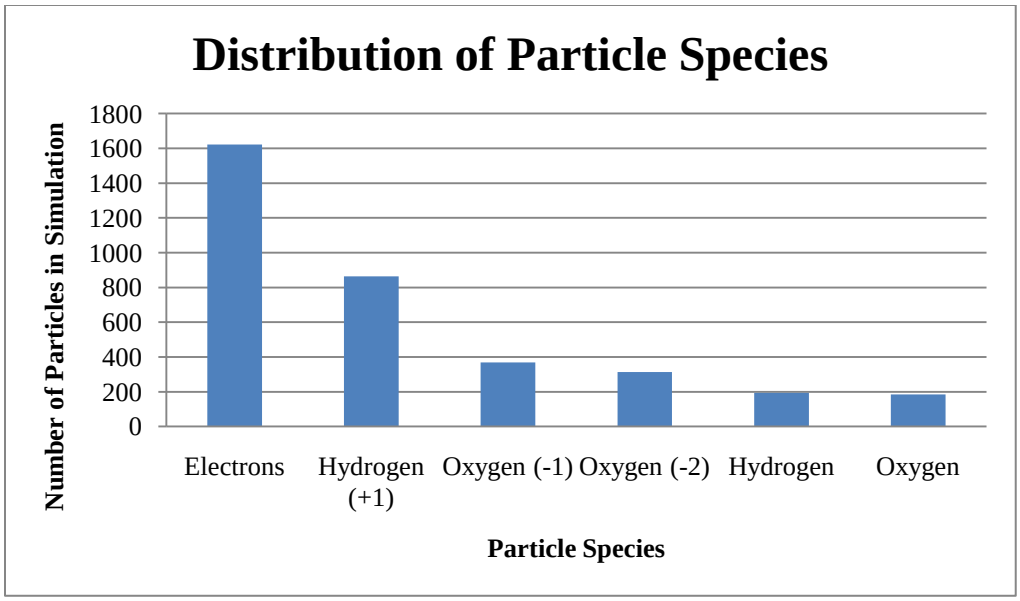

Figure 6-19: Distribution of Particle Species from VF Simulation

Comparison should not be made between the number of particles per unit volume of the VF simulation and Lan et.al. In Lan, the particle density is in units of ($x10^{26}$ particles/m^3). The total volume for the simulation discharge is approximately $1.2x10^{-8}$ m^3. Following the results from Lan, the maximum electron content should be approximately $9.6x10^{18}$ electrons. The VF simulation has a total of 1621 electrons in the simulation. The VF simulation is based on the number of particle trajectories emitted from a single element. The simulation has one particle per element to minimize computational time. While the absolute number of particles cannot be compared the ratio of the electrons to other species can be used to compare the simulation and literature.

The ratio of electrons to the other species can be used to determine whether the simulation data matches the published literature. The electron content dominates the discharge followed by the ion content and then neutral atoms. The ratio of electrons to the other species can be used to compare the results of the two data sets. The ratio of

electrons to the other species should be similar even if the total number of particles is different. Table 6-3 compares the electron ratios for the VF simulation and Lan et.al.

Table 6-3: Ratios of Electrons to Particles Species

Species	VF Simulation	Lan - Literature
Hydrogen (+1)	1.88	1.38
Oxygen (-1)	4.4	3.08
Oxygen (-2)	5.18	4
Hydrogen	8.36	8.89
Oxygen	8.81	10

The ratio of the electrons to the other particles in the simulation is similar to the ratios obtained in the literature. The Pearson correlation coefficient between the two data sets is 0.981 with a p-value of 0.003. The correlation between the data set can be seen in Figure 6-20.

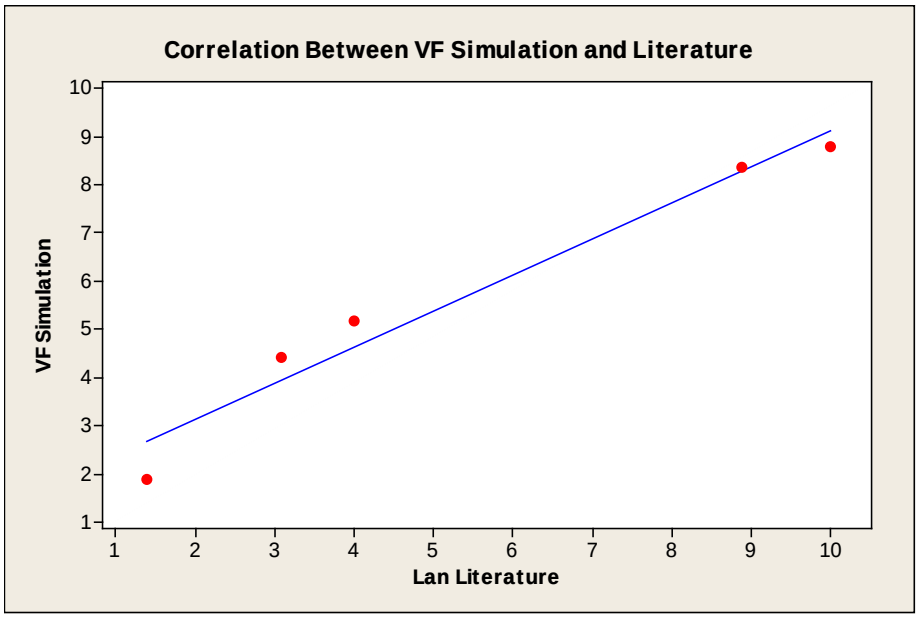

Figure 6-20: Correlation between Simulation and Literature

There is strong correlation between the Vector Fields simulation results and those published by Lan. Therefore, it can be concluded that the physics used in the VF simulation produces a similar particle species trend as other research efforts found in the literature and that the simulation physics accurately represents species formation.

6.1.2.2 Comparison of Secondary Particles to Slurry Compounds

Having established that the ratios of the secondary particles match other research efforts from the literature, they can be used to estimate potential compounds in the slurry. The simulation showed that both copper +1 and +2 ions are formed. The copper +1 ion is approximately 2.3 times as abundant as the copper (+2) ion. Elementary chemistry indicates that the most likely compounds to form in the underwater discharge are elemental copper (melted from anode and not ionized, and copper ions that interact with the free electrons in the system), and two forms of copper oxides (Cu_2O, CuO) which are made up from the two ion states of copper and the two ion states of oxygen (Yoder 2006) (Patnaik 2004) (Lide 2007-2008) (Burgess 1999). The secondary emission characteristics of copper followed those outlined by Barber (Barber 1921).

Copper oxides have the advantage of having clearly distinguishable compounds based solely on the color of the resulting compounds. For example, Copper (I) oxide is a reddish powder and copper (II) is a dark brown, or nearly black powder. If copper carbonate forms it is a yellow powder (Patnaik 2004) (Chemglobe 2009). Therefore, with copper we can with reasonable accuracy determine what compounds have been formed without extensive chemical analysis.

To evaluate compounds in the slurry three methods were used. The first was to dry homogeneous volumes onto microscope slides for high magnification analysis. The second was to dry homogeneous volumes of the solution onto silicon wafers for SEM/EDS analysis. The third was to use an independent chemistry lab to perform wet chemical analysis to determine chemical compound content.

Method 1: Light Microscope

Samples of the slurry were evaporated and the remaining material is viewed under a high magnification light microscope. Dark brown, reddish, and copper metal colors were clearly observed. Based on the descriptions of the color of the copper oxide compounds, it can be concluded that elementary copper, copper (I) oxide, and copper (II) oxide are all present in the slurry. However, even at 1000X magnification it was not possible to determine the species distribution.

Method 2: SEM Analysis

Samples of the slurry were prepared for scanning electron microscope (SEM) analysis. The SEM used was a Philips XL-30 ESEM with EDAX (EDS) capability. All samples were mounted on silicon wafers. The SEM system uses a field emission source and is housed in the Benjamin Cluff building in the biology department at Brigham Young University. Samples were prepared by placing a small volume of homogeneous slurry onto the silicon slide and allowing the water to evaporate. The remaining particles were analyzed under SEM.

Two primary types of structures were observed: a crystalline structures and a fine, wispy type structure that is believed to be an amorphous copper oxide structure. The crystalline structures were fairly uniform in shape and size. The wispy structures were

less common than the crystalline structures. An example image of the crystalline structures is shown in Figure 6-21 and an example image of the amorphous structures is shown in Figure 6-22.

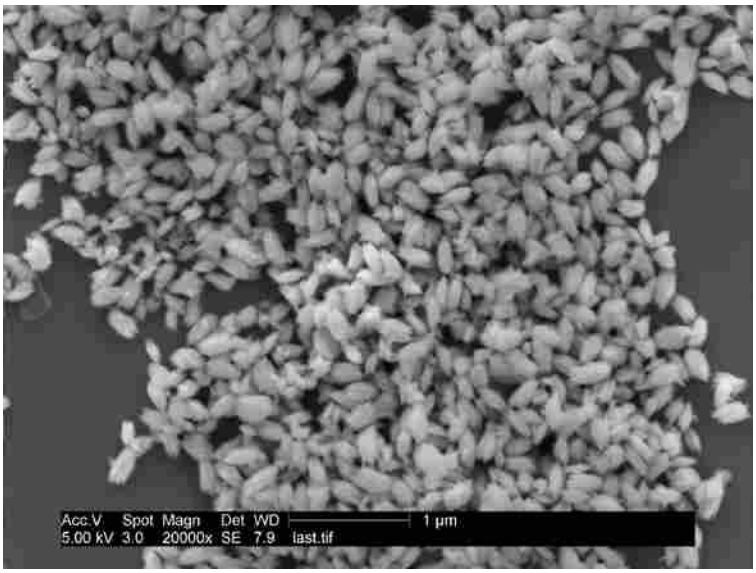

Figure 6-21: SEM of Crystalline Copper Particles

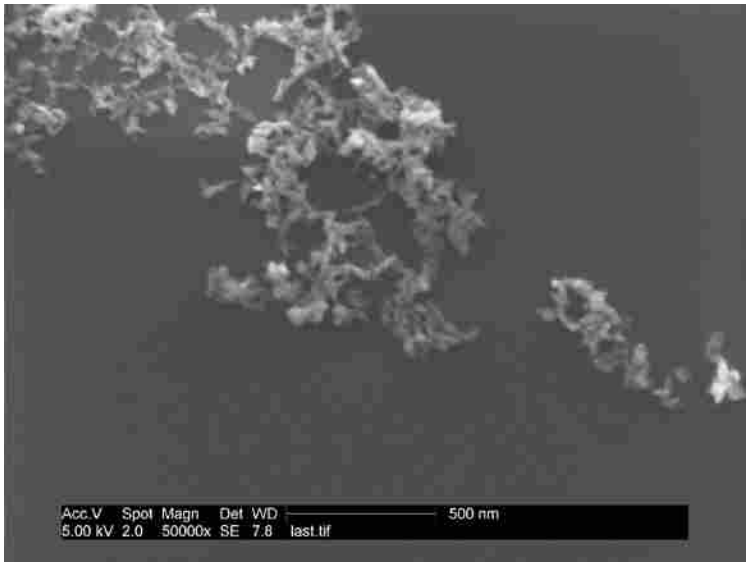

Figure 6-22: SEM of Amorphous Copper Structures

In both cases, the particle size is in the sub-micron scale. The smallest structures are less than 20 nm. These represent primarily colloidal materials that are suspended in the slurry. The EDS for both particle types was similar. An example is Figure 6-23.

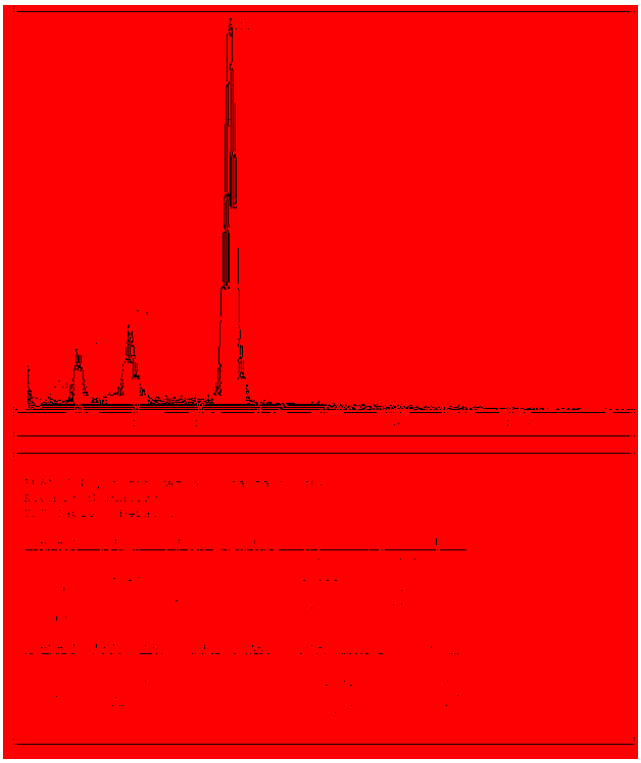

Figure 6-23: EDS of Copper Particles

EDS shows that there is copper and oxygen in sufficient weights and atomic content to indicate both copper (I) and (II) oxides could be present. It is unknown if the crystalline and amorphous structures are different compounds, or representative of different states of the same oxide compounds. Other SEM images identified particles of pure copper. The SEM analysis showed that there is pure copper metal, and by atomic weight, both copper oxide formulations. It is unclear which oxide form is more prevalent or what the species distribution is.

Method 3: Independent Laboratory

Samples of the slurry from the process machine were sent to an independent chemistry lab to perform wet chemical analysis to determine chemical compound content. The laboratory confirmed the presence of elemental copper and both copper oxides. The non-aqueous species distribution from their analysis was 42% elemental copper, 37% copper (I) oxide, 19% copper (II) oxide, and 2% unknown compounds.

6.1.2.3 Comparison of Secondary Particle Tracks to High Speed Images

The third tool used with the secondary particles was to compare the particle tracks to high speed images. This method is the most qualitative of the three tools and is used only for comparative analysis. There are two primary types of visible light emission: spectral emission and thermal emission. Spectral emission occurs when an electron gives off its characteristic spectrum through a change of energy state (state change, change in direction, ionization). Thermal emission is dominated by the highest temperature material in the plasma. Spectral emission is what is used to experimentally determine the electron temperature of the discharge.

As the primary electron beam travels through the gap and interacts with the dielectric media the secondary particles are generated. The Vector Field simulation simulates the secondary emission of electrons, hydrogen (neutral and ion), and oxygen (neutral and ion). It is inferred that when the collision and ionization occur (generation of a secondary particle), that there is some form of spectral or thermal photon emission. Therefore, while the simulation does not specifically predict photo emission

characteristics, the secondary emission particle trajectory, or particle cloud, should have some resemblance to the actual discharge.

There were two high speed cameras used to obtain images of the discharge. The first was a Phantom V12.1 research grade monochromatic camera from Vision Research with frame rates from 500 to 320,000 frames per second. The discharge could not be resolved at frame rates above 180,000 fps (128 x 128 pixels). The second camera was a Panasonic HDC-TM300K with up to 1,000 fps color and full HD at 30 fps. It was found that the Phantom V12 camera was most effective at determining the following: velocity of illuminated particles, the number of cathode spots, the duration of a discharge, and the total size of the illuminated region (plasma). The color images show the color spectrum of the plasma, the formation and ejection of gaseous compounds (either hydrogen or oxygen) and comparison of the plasma shapes with the simulation results. Table 6-3 shows the results of using the Vision Research image processing tools on the footage.

Table 6-4: Summary of Plasma Characteristics from the Phantom V.12

Characteristic	Units	Range	Average/Typical
Illuminated Particle Velocity	cm/sec	10^3 to 10^5	8.76 x 10^4
Number of Cathode Spots	Integer	1 to 4	1 to 2
Duration of a Discharge	microsecond	<1 to 200	4 to 6
Plasma Dimensions (Length, Width)	mm	L: 1 to 10 W: 0.2 to 6	L: 4 to 6 W: 0.8 to 1.5

The velocity and the duration of the discharges are in good agreement with the literature (Fridman and Kennedy 2004). Because it is a non-refractory metal, and in the process machine the electrodes are typically rotating, it is expected to see multiple cathode spots in a discharge. Evidence of this can readily be seen in a typical discharge

at viewed at 20,000 fps (680 x 680 pixel resolution) from the Phantom V.12 as shown in Figure 6-24.

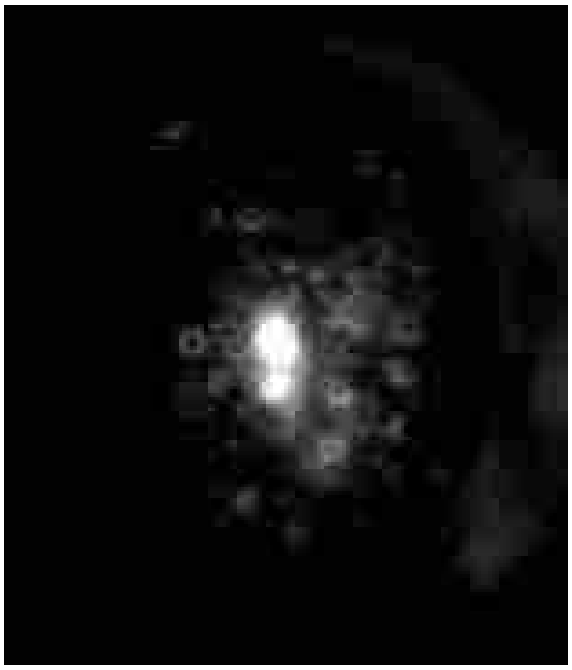

Figure 6-24: Typical Discharge 20,000 fps (2 Cathode Spots)

However, under controlled experiments a single discharge without multiple cathode spots could be achieved. It is images of these single discharges that will be used to compare the high speed images to the particle trajectories in the simulation. Figure 6-25 shows a frame from the Panasonic camera where arc ignition was captured. This image is compared to the primary and secondary electron beam trajectories.

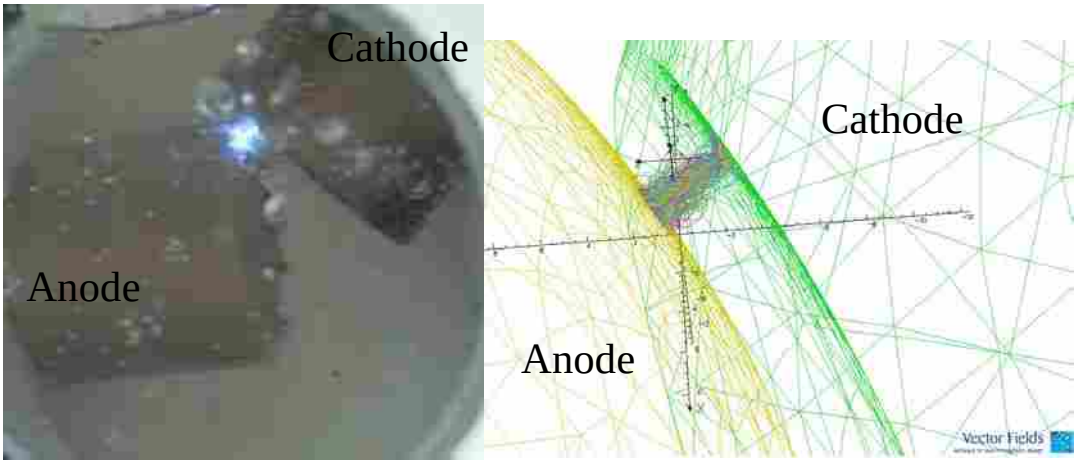

Figure 6-25: Arc Initiation vs. Primary and Secondary Electron Beam

There is a fine, cylindrical beam of intense light in the center of the discharge which visually corresponds to the shape and size of the primary beam with the secondary electron emission. There is a non-uniform corona of blue light surrounding the beam. Close inspection of the corona shows fine bubbles being formed and accelerated away from the discharge region. The bubbles are traveling perpendicular to the lighted area of the discharge indicating that there is little or no charge in the bubbles. Figure 6-26 shows the comparison of the secondary particle cloud from the simulation compared to a typical discharge from the high speed images.

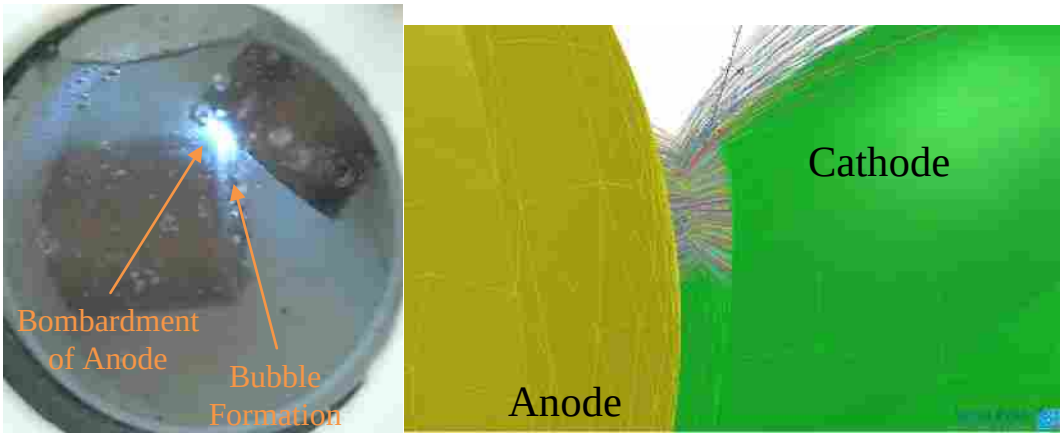

Figure 6-26: Secondary Particle Cloud vs. High Speed Image

In the high speed image it can be seen that there are illuminated particles bombarding the surface of the anode. The shape of the plasma is almost cylindrical with curvature where the surfaces meet. The simulation is taken from the same perspective showing that even with a relatively small number of particle trajectories that the same general pattern is present. Ion bombardment in the simulation is readily observed and separated from the other trajectories. The particle bombardment in the high speed image has the same shape (nearly hemispherical) as the simulation. This is an example of the cos(θ) distribution for secondary particle emission.

Bubble formation can also be seen in the larger gap between the electrodes. The trajectories of bubble motion are in randomly oriented straight lines traveling away from the plasma region. These bubbles are hydrogen or oxygen and would be the neutral particles from the simulation which have a random orientation, but travel in a straight line away from the primary beam and secondary cloud as they have no electrical attraction to either the cathode or the anode. A more illustrative high speed image of this phenomenon compared to the Vector Fields simulation of the neutral particles is shown in Figure 6-27.

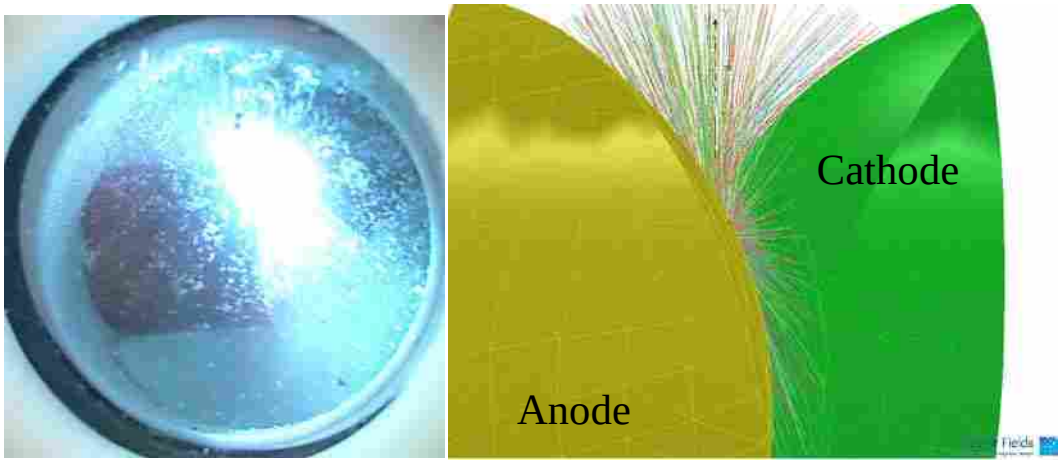

Figure 6-27: Neutral Particle Trajectories

Here it can be seen that there is a massive number of fine bubbles being generated and that they are traveling away from the discharge. By moving frame by frame in the sequence it is evident that the particles are traveling in straight lines away from the discharge. In can be concluded that the primary secondary particle physics (ion bombardment of anode, cos(θ) distribution of emission, trajectories of neutral particles, and general shape of the plasma region) represented in the VF simulation have corresponding empirical evidence in the high speed images. Further, the shape and size of the VF simulation has good correspondence with the typical discharge recorded by the high speed images.

6.2 Validation Summary

The primary electron beam from the simulation exhibits the general physics and features expected by a constricted arc. There is a cathode sheath with length and acceleration profiles that correlate with widely published literature. The expected beam induced magnetic fields are simulated and demonstrate the expected effect. And the electron temperature calculated directly from the particle velocity of the model corresponds to published data for similar discharges.

The electron content dominates the discharge in the simulation followed by the ion content and then neutral atoms. The ratio of the electrons to the other particles in the simulation is similar to the ratios obtained in the literature. The VF simulation has a consistently higher ratio, but the same trends. The physics used in the VF simulation produces a similar particle species trend as other research efforts in the literature.

The distribution of the particles from the simulation was not well correlated or validated to actual compounds generated, but the expected compounds from elementary chemistry from the simulation results were all present. The simulation could not be used to determine the actual species distribution, but emission physics and particle trajectories from the simulation have real correspondence the discharge created by the experimental process machine.

The general dimensions of the charged particle cloud correspond to the typical dimensions of the illuminated region in the high speed images. The neutral particles, which are a representation of the hydrogen and oxygen gas bubbles, have good correspondence to images where the gas bubble generation is clearly observed. Therefore, it is concluded that there is reasonable correspondence between the simulation and the actual process machine.

6.3 Simulation Range

The primary electron beam characteristics are the most important results from the simulation. The beam dominates the physics within the discharge. Additionally, the secondary emission physics are important to have a complete physical representation of the discharge. The results discussed to this point have come from the same emission physics from literature with only slight variations in the dielectric properties of the slurry.

A more complete understanding to the usable range of the simulation inputs is important for future investigation of other materials, input power, electrode

configurations, and dielectric property analysis. In order to determine which input parameters a sensitivity analysis of the simulation is needed.

Through the simulation development it was established that the emission physics were heavily influenced by the cathode spot size and the discharge gap. However, if the discharge gap is altered in the simulation the dielectric media and the mesh structure must be updated for the new model configuration. Also, the size of the cathode spot is directly proportional to the amount of emission that occurs. As the area of emission surface increases the higher the emission will be since Vector Fields is based on a theoretically infinite current source.

As noted previously, the average affected are of the cathode spot was approximately 1 mm^2 and the discharge gap was typically 1 mm. In order to maintain the same boundary conditions without introducing a potential lurking variable from different electrode configurations the spot size and discharge gap were kept constant. Also, since the unaffected slurry has no effect on the discharge physics it was also kept constant.

After these controlled parameters, there are 10 other primary simulation inputs that could be varied. In order to investigate the effects of these ten parameters a statistical screening method was used. A twelve run Plackett-Burman screening design was used to analyze the main effects of the various input parameters. The same analysis tools discussed in the validation sections above were used to analyze the results of the simulation runs for the screening design. As a summary the following tools were used:

1. Shape of the primary electron beam – effect of beam magnetics present
2. Anode current density maps – determine if the correct types of structures are present

3. Total current – value compared to experimental and validated simulation
4. Electron temperature – values compared to validated simulation
5. Cathode sheath parameters, - length, electron acceleration, beam magnetics

Table 6-4 shows the ten factors included in the 12 run Plackett-Burman screening design and the high and low values used for the analysis.

Table 6-5: Factors for Plackett-Burman Experimental Design

Factor Designation	Properties (Factors)	Low	High
X_1	Work Function (eV)	4.3	4.5
X_2	Cathode Spot Temperature (K)	3,000	4,000
X_3	Emission Constant (A/cm^2K^2)	60	120
X_4	Voltage Boundary Condition	-25	-72
X_5	Relative Permittivity (Plasma Bubble)	85	100
X_6	Conductivity (S/m) (Plasma Bubble)	5	10
X_7	Relative Permittivity (Transition Layer 1)	82	88
X_8	Conductivity (S/m) (Transition Layer 1)	1	5
X_9	Relative Permittivity (Transition Layer 2)	82	85
X_{10}	Conductivity (S/m) (Transition Layer 2)	0.001	0.01

Upon reviewing the raw data there were some settings that produced unrealistic primary electron beams, anode spot structures, and that had very low current compared to others in the sample. The results for total current, maximum current density, and mean velocity of the simulation were the most useful outputs for statistical analysis. Figures 6-

28 and 6-29 show a Pareto diagram and a normal plot of the standardized effects for total current of the design evaluation of the simulation.

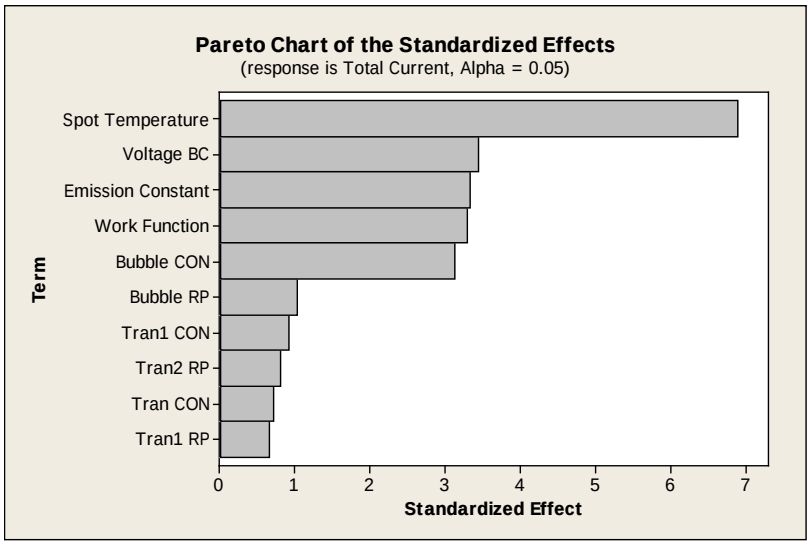

Figure 6-28: Pareto Chart of Effects on Total Current

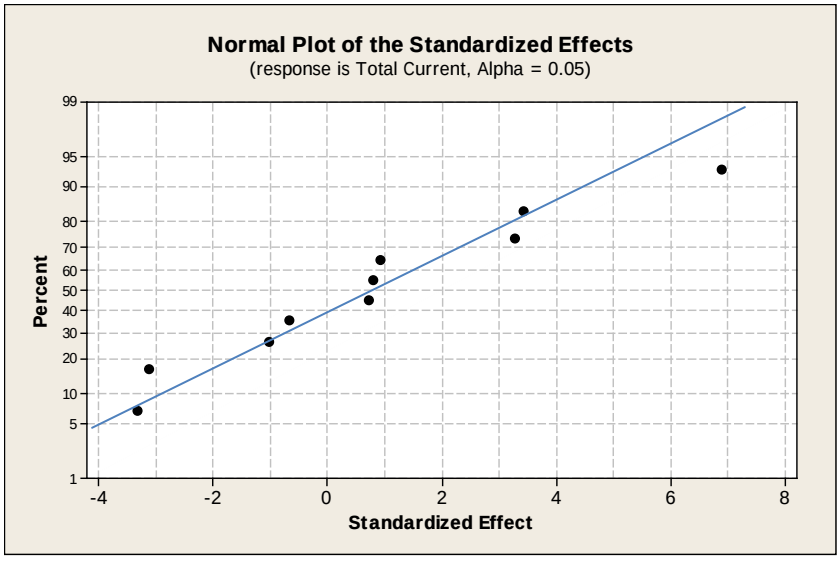

Figure 6-29: Normal Probability of Effects on Total Current

The total current is most heavily affected by the emission characteristics of the cathode spot and the voltage boundary condition. Of all of the slurry properties the

conductivity of the plasma bubble has the largest effects on the system. However, the spot temperature is the only effect on the normal probability plot that indicates a main effect. Therefore, the cathode spot temperature is an important parameter for this simulation. Upon further investigation, the cathode voltage will not provide any realistic electron beam below 18 volts. Therefore, 18 volts is the lower limit for the simulation. High kV analysis was not completed in this work. The usable range for the input voltage as tested is -18 volts to -120 volts; although higher voltages are likely to be able to correlate to data. Related to total current is current density at the anode surface where the primary beam contacts the anode. Figure 6.30 shows the pareto diagram of effects on current density.

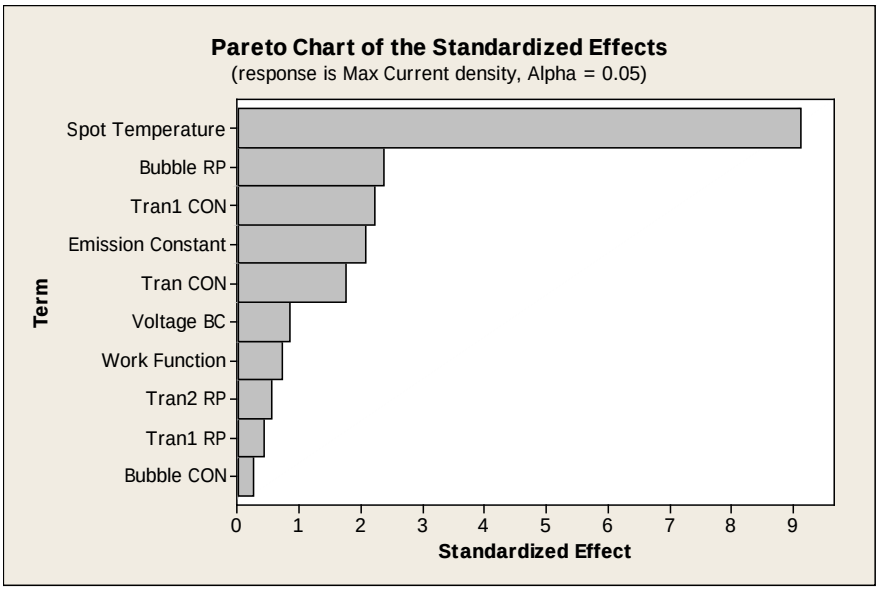

Figure 6-30: Pareto Charge of Effects on Max Current Density

Similarly to the current Pareto chart, the spot temperature is the most important parameter for this effect. The dielectric properties of the different regions of the simulation have a minor effect. Using the normal probability of effects plot show that

electron temperature is the most important characteristic of the discharge current. Figure 6-31 shows the Pareto diagram for effects on the average velocity of the primary electron beam.

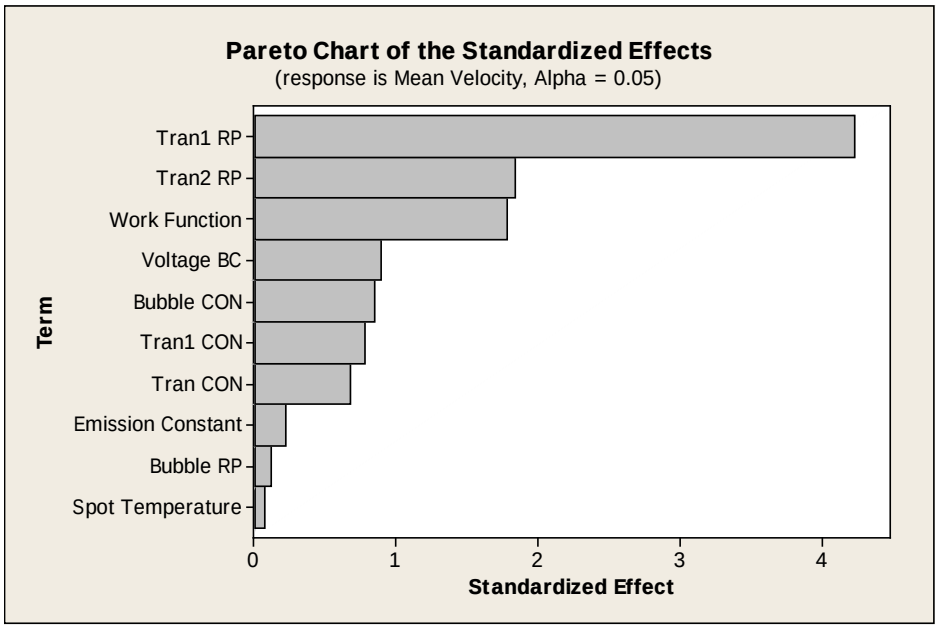

Figure 6-31: Pareto Chart of the Standardized Effects on Mean Velocity

Unlike the other outputs, the velocity parameters are most heavily influenced by the relative permittivity (dielectric constant) and the work function of the cathode than any other parameters. The conductivity of the various layers has no appreciable effect on the simulation outputs.

From the screening test the three emission parameters (spot temperature, work function, and emission constant) are important to the discharge. The relative permittivity has a larger effect on the discharge physics than the conductivity for the three outputs listed above. Overall, the most important parameter to the discharge physics is the cathode spot temperature.

The lower limit for the cathode spot temperature (3,000 K) always produced unrealistic primary electron beam shapes, currents, and anode current density maps. The experimental design included center points and the simulation at 3,750 K had good beam induced magnetic effects, beam currents with the experimental distribution, and realistic beam currents. Another simulation run was completed at 3,500 K and the outputs were unrealistic. The lower temperature limit for the cathode spot temperature is 3,700 K regardless of work function or emission constant values.

The work function of all commonly used electrode materials range from 2.5 to 5.0 eV. This simulation can only be compared to copper which has a typical value of 4.4 eV. The screening design showed that for values of 4.3 to 4.5 eV the outputs of the simulation were comparable to the validation results described previously. Therefore for copper, a work function between 4.3-4.5 eV can be used.

The emission constant was not statistically significant in for any of the outputs tested in the screening design. As noted previously, this parameter is typically used to adjust the emission and beam physics to tune the simulation to match experimental results. In this case it could be assumed that the emission constant can be left at 120 with marginal effects on the simulation results.

The relative permittivity of the different regions can have a significant effect on the discharge physics. The acceptable ranges of the different regions are still unknown. However, the settings used in the results and validation section provide good correspondence between the simulation and experimental results or results published in the literature.

Like the emission constant, the conductivity of the various layers in the dielectric media can be used to tune the simulation to better match experimental results. They do not have a statistically signification role in any of the outputs of interest.

In summary, the most important parameters for the discharge physics are the cathode spot temperature, the voltage boundary condition, and the relative permittivity of the regions in the dielectric media. The work function should be defined by material and are well researched and published in the literature. The emission constant can be used to tune a simulation to match empirical results. The relative permittivity of the dielectric media should be included in characterizing the discharge while the conductivities can be used to tune the simulation similar to the emission constant.

6.4 Chapter Summary

The simulation was validated in using six tools for the two different types of charged particles in the system. The primary beam was validated using the following:

- A semi-quantitative method of comparing the anode spot remnants to the current density maps from various simulation runs
- Comparison of the electron temperature calculated directly from the simulation to the literature
- Comparison of the total current in the simulation to the experimentally measured peak discharge current and to literature

There was good correspondence between the simulation output results and the experimental and literature results. The secondary particles were validated using the following methods:

- Comparison of the individual species generated in the discharge gap to literature
- Comparison of the species generated to compounds identified using SEM and other microscopy tools
- Comparison of high speed images to the secondary emission tracks from the simulation

There was good correlation for the individual species in the discharge gap and those in literature. The microscopy methods provided insight into the structures of the formed particles. The comparison of the emission tracks to the high speed images provides some qualitative data that the simulation corresponds to the actual discharge. More quantitative measurement methods should be developed.

Having validated the simulation and identified the key simulation outputs, the range of input parameter settings and their effect on the output was investigated with a screening design. The most important parameters for the discharge physics are the cathode spot temperature, the voltage boundary condition, and the relative permittivity of the regions in the dielectric media. The work function should be defined by material and are well researched and published in the literature. The emission constant can be used to tune a simulation to match empirical results. The relative permittivity of the dielectric media should be included in characterizing the discharge while the conductivities can be used to tune the simulation similar to the emission constant.

7 Inferences and Conclusions

This chapter will review the research objectives and hypothesis in relation to the research. Following this review, the strengths and weaknesses of the simulation results and simulation methodology are reviewed. Finally, the key inferences, conclusions, and contributions of this research are described.

7.1 Research Objective and Hypothesis Review

It was noted that the majority of the literature regarding the numerical simulation and other modeling approaches for arc discharges has been accomplished using a plasma physics approach with ideal gas approximations. However, discharges that occur in liquid dielectric media, such as oil and water, do not have as extensive simulation efforts described in the literature primarily because the dielectric media has a significant effect on the discharge physics.

It was hypothesized that the discharge physics of a DC electric arc discharge in a lossy dielectric media could be accurately simulated within the Vector Fields environment using a particle physics approach. This hypothesis resulted in the development of two research objectives:

3. Develop a methodology to examine a discharge in a lossy dielectric media within the Vector Fields environment
4. Validate the methodology using a case study of interest (provided by QLR, LLC)

As shown in chapters three through six, the research objectives were fully met and the hypothesis is confirmed. A particle physics approach to a discharge can be used to simulate a discharge in a liquid dielectric media.

7.2 Strengths and Weaknesses of the Simulation Methodology and Results

One of the primary advantages of the simulation methodology is that a whole class of discharges can now be investigated using this simulation tool. The following are some key strengths and weakness of the simulation methodology and the simulation used in the case study with the experimental apparatus.

7.2.1 Simulation Strengths

The following is a list of the strengths of the simulation methodology and results from the case study.

1. The primary electron beam from the simulation exhibits the general physics and features expected by a constricted arc and are well validated:
    a. Cathode sheath length and acceleration profiles that correlate with widely published literature
    b. The beam induced magnetic fields are simulated and demonstrated in greater detail than those found in other simulation efforts

c. The electron temperature calculated directly from the particle velocity of the model corresponds to published data for similar discharges

2. The simulation includes the secondary particle generation physics by chemical species and has correspondence to literature and experimental results
3. Simulation methodology can be used to simulate a discharge in a dielectric media and provides a self-consistent electrostatic simulation with the particle physics of the primary constituents of the discharge

7.2.2 Simulation Limitations/Weaknesses

As this simulation is the first of its kind, there are some inherent limitations or weaknesses of the simulation methodology. The following is a list of the model limitations or weaknesses of the simulation mythology and results from the case study.

1. The effects of temperature, pressure, and other hydrodynamic effects of the discharge are not included in the simulation
2. Cathode spot phenomena such as spot motion and splitting are not included
3. The cathode spot geometry and physics are simulation inputs rather than outputs
4. The simulation is electrostatic (steady-state) no transient effects from the electrical or thermal changes are included
5. Infinite current is assumed in the model where in reality there is some current loss in the beam and voltage drops across the sheath as emission occurs
6. The dielectric properties are extrapolated from slurry data rather than functionalized to simulation physics (temperature, phase change, contamination rates of metal and metal-oxides generated by the discharge)

7. The simulation tool was only validated for copper discharges and needs to be validated for other materials and geometries

7.3 Key Inferences, Conclusions, and Contributions

The following is a list of the key inferences and conclusions that can be drawn from the simulation and its validation as well as the contributions of this research to the body of knowledge for discharges in dielectric media:

1. The physics of the primary beam shows good correspondence to the literature and experimental results in the following areas:
    a. Cathode sheath physics in the length and acceleration of electrons
    b. Predicted electron temperature profile of the beam
    c. Total beam current
2. The simulation shows how the primary electron beam and secondary particle physics are affected by the space charge, dielectric media, beam induced magnetic fields, and emission characteristics of the arc
3. The simulation can readily be used to investigate other materials or dielectric media. The geometry or the methodology can readily be applied to other electrode and dielectric media configurations
4. The simulation provides a representation of the actual particle trajectories in the discharge and can be used to investigate both primary and secondary emission

5. The most important parameters for the discharge physics are the cathode spot temperature, the voltage boundary condition, and the relative permittivity of the regions in the dielectric media.
    a. The emission constant can be used to tune a simulation to match empirical results
    b. The relative permittivity of the dielectric media should be included in characterizing the discharge
    c. The conductivity of the various regions in the dielectric material can be used to tune the simulation similar to the emission constant

Therefore, the simulation methodology can be used to investigate the following:

1. Any metal, electrode geometry, discharge gap, or dielectric media can be studied
2. Primary Beam Physics
    a. Electron velocity/acceleration (direct calculation of electron temperature)
    b. Energy deposition on the anode from all emission sources
    c. Effect of dielectric media on beam physics (trajectories, velocity, constriction, beam induced magnetic fields, space chare, and secondary emission)
    d. Beam current
    e. Particle trajectories (including relativistic effects)
3. Secondary Particle Generation and physics
    a. Atomic species (neutral particles or ions) and secondary electron emission
    b. Particle trajectories
    c. Back ion bombardment on the cathode

The key contributions of this research to the body of engineering knowledge are:

1. Taken an existing tool and developed it for a new application
2. This newly developed tool is the first to simulate the charged particle beam in a discharge within a dielectric media by adapting a commercial FEA code
3. The results of using this tool confirms that a particle physics approach to simulating discharges is comparable to a plasma physics and experimental research
4. This new simulation tool can be used to provide greater insight into the following phenomenon for an underwater discharge:
    a. The primary and secondary emission physics and particle trajectories
    b. The effect of the dielectric media on emission physics, beam induced magnetic fields, and arc constriction
    c. Anode energy deposition
5. Direct simulation of electron temperature for comparison to experimental spectroscopy measurements
6. New tool opens the door to developing process rules for creating particles using an underwater discharge

It can be seen that the simulation methodology and results have some important strengths and limitations. Also, the case study simulation has good correspondence of its key outputs to examples in the literature and experimental results from the process machine. Overall, this methodology and the case study results show that using a particle physics approach to simulate a discharge will provide useful results for the further study of discharge physics.

8 Recommendations for Future Research

This chapter will list the recommended future research activities based on the findings which have been detailed in this work. Many of these recommendations follow from the limitations of the methodology and case study in the previous chapter.

1. Using experimentation and this new simulation tool, manufacturing process rules should be developed for creating desired particles using an underwater discharge
2. Apply simulation methodology to:
    a. Other electrode materials, configurations, and discharge gaps
    b. Other dielectric media, gases, vacuum (EDM, gaseous discharges)
    c. Investigate multiple cathode spot behavior
    d. Similar applications:
        i. Liquid dielectric breakdown
        ii. Vacuum discharges
        iii. Underwater high kV pulsed power discharges
        iv. Lightning strikes
        v. Ion beam/gas interactions
3. Develop a methodology to include the missing physics of the model:
    a. Temperature, Pressure, and Hydrodynamic Effects

b. Add energy and current loss from collisional interactions in the model
c. Include transient electrical and thermal effects
d. Include power supply current and voltage performance (realistic power source instead of an ideal current source)

4. Develop a methodology to correlate the erosion/vaporization of the cathode and anode to the current density from the cathode spot emission and energy deposition of the primary beam to anode
5. Develop a method to functionalize dielectric properties of the slurry to one of the simulation outputs such as temperature, electrical field, or current. The dielectric properties then could be used with optimization routines for the simulation or to readily study other materials without concern for determining the dielectric properties using some other technique

9 References

www.aws.org (accessed 2009).

Aka-Ngnui, T, and A Beroual. "Bubble Dynamics and Transition into Streamers in Liquid Dielectrics Under a High Divergent Electric Field." (Journal of Physics D: Applied Physics) 39, no. 9 (2001): 1408-1412.

American National Standards Institute. "ASTM D877-00: Standard Test Method for Dielectric Breakdown Voltage of Insulating Liquids Using Disk Electrodes." In *2001 Annual Book of Standards Volume 10.03*. 2001.

Anders, A. *A formulary for plasma physics.* Akademie-Verlag, 1990.

Anders, Andre. *Tracking Down the Origin of Arc Plasma Science II. Early Continuous Discharges.* United States Department of Energy, Washington DC: Office of Scientific and Technical Information (OSTI), 2003.

Barber, I. Garnett. "Secondary Electron Emission from Copper Surfaces." *Physics Review* (Ameriacan Physical Society) 17, no. 3 (August 1921): 322-338.

Benilov, M S, and A Marotta. "A model of the cathod region of atmospheric pressure arcs." (Journal of Physics D: Applied Physics) 28, no. 1869-1882 (1995).

Bingul, Zafer. *Dynamic Modeling of the Gas Metal Arc Welding Process.* Electrical Engineering, Nashville, TN: Vanderbuilt University, 2000.

Boxman, R., and E. Gidalevich. *Communications on Underwater Discharges* (2007-2008).

Boxman, Raymond L, Philip J Martin, and David M Sanders. *Handbook of Vacuum Arc Science and Technology, Fundamentals and Applications.* Park Ridge, New Jersey: Noyes Publications, 1995.

Brigham Young University Department of Chemistry. 2009. [Online] http://people.chem.byu.edu/bfwoodfield/research_interests.html (accessed 2009).

Burgess, John. *Ions in Solution.* Coll House, Wetergate, Chichester, West Sussex, Englan: Horwood Publishing Limited, 1999.

Chadband, W.G. "From Bubble to breakdown, or vice-versa." *IEEE 11th International Conference on Conduction and Breakdown in Dielectric Liquids.* Baden-Dattwil, Switerland: IEEE, 1993. 184-193.

Chemglobe. 2009. www.chemglobe.org/ptoe/.

Chhowalla, M, H Wang, N Sano, Teo KBK, and GAJ Amaratunga. "Carbon onions: Carriers of the 217.5nm intersteller absorption feature." (Physical Review Letters) 90, no. art. no. 155504 (2003).

Chhowalla, Manish. *Personal Communication* (2008).

Colbham Technical Services. *Opera User Manual for Vector Fields Version 12.* Oxford, England, 2009.

Damamme, G, C Le Gressus, and A S De Reggi. "Space Charge Characterization for the 21st Century." (IEEE Transactions on Dielectris and Electrical Insulation) 4, no. 5 (October 1997).

Davila, Lilian P, Valerie J Leppert, and Subhash H Risbud. "Microstructure and Microchemistry of Silicon Particles formed during Electrical Discharge Machining." (Journal of Materials Science: Materials in Electronics) 14, no. 2003 (2003): 507-510.

Descoeudres, Antonine. *Characterization of Electrical Discharge Machining Plasmas.* Lausanne, France: Ecole Polytechnique Federale De LaUSaNNE, 2006.

Dobrestsov, L N, and M V Gomounova. *Emission Electronics.* Moscow: Nauka Science, 1966.

Dowden, John, and Phiroze Kapadia. "Plamsa arc welding: a mathematical model of the arc." (IOP Plublishing Ltd) 1994.

Ducharme, Robert, Phiroze Kapadia, John Dowden, Matthew Thronton, and Ian Richardson. "A mathematical model fo TIC electric arcs operating in the hyperbaric range." (Journal of Physics D: Applied Physics) 29 (1996).

Efunda. *Efunda Engineering Fundamentals.* August 2008. www.efunda.com/ (accessed August 2008).

Elliot, Steven. *Thin Film Consulting, Communications Regarding Vector Fields* Salt Lake City, UT, (2009).

Engineers, Miller Applications. *Personal Communications Over AC Welding Development* (2008).

Fowler, R.H. "The Thermionic Emission Constant." *Proceedings of the Royal Society of London A.* Royal Society Publishing, 1929. 36-49.

Fransis, G. *Ionization Phenomena in Gases.* London: Butterworths, 1960.

Fridman, Alexander, and Lawrence A. Kennedy. *Plasma Physics and Engineering.* New York, NY: Taylor & Francis, 2004.

Fulton, Richard N. "Advances in Underwater Welding." (IEEE) 1986.

Gidalevich, E, and R L Boxman. "Steady-state model of an arc discharge in flowing water." (Plasma Sources Science and Technology) 15 (2006).

Gidalevich, E, and R L Boxman. "Sub-and Super sonic expansion of an arc channel in liquid." (Journal of Physics D: Applied Physics) 39 (2006).

Gidalevich, E, R L Boxman, and S Goldsmith. "Hydrodynamic effects in liquids subjected to pulsed low current arc discharges." (Journal of Physics D: Applied Physics) 27 (2004).

Gidalevich, E, R L Boxman, and S Goldsmith. "Theory and modelling of the interaction of two parallel supersonic plasma jets ." (Journal of Physics D: Applied Physics) 31, no. 3 (304-311) (1998).

Gnedienko, Boris, Igor Pavlov, Igor Ushakov, and Sumantra Chakravarty. *Statistical Reliablity Engineering.* New York, NY: John Wiley & Sons Inc., 1999.

Godyak, Valery A, and Natalia Sternberg. "Smooth Plasma-Sheath Transition in a Hydrodynamic Model." (IEEE Transactions on Plasma Science) 18, no. 1 (1990).
Granovsky, V L. *Electric Current in Gas, Steady Current.* Moscow: Nauka Science, 1971.

Gurney, Ronald W. *Ionic Processes in Solution.* New York: Dover Publications, Inc., 1953.

Goshima, H, N Hayakawa, M Hikita, H Okubo, and K Uchida. "Weibull Statistical Anlaysis of Area and Volume Effects on the Breakdown Strength of Liquid Nitrogen." (IEEE Transactions on Dielctrics and Electrical Insulation) 2, no. 3 (1996).

Harris, L. P. "Arc Cathode Phenomena." In *Vacuum Arcs Theory and Application*, by James M. Lafferty, 120-168. San Fransico: John Wiley and Sons, Inc., 1980.

Hirata, Yoshihiro, Yoshio Ueda, Hiroaki Takase, and Kazuaki Suzuki. Method and device for manufacturing metallic particulates, and manufactured metallic particulates. United States of America Patent 7108735. September 19, 2006.

Hsu, K. C., and E. Pfender. "Modeling of a Free-Burning, High-Intensity Arc at Elevated Pressures." (Plasma Chemistry and Plasma Processing) 4, no. 3 (1984).

Incropera, Frank P, and David P DeWitt. *Fundamentals of Heat and Mass Transfer, 5th Edition.* New York, NY: John Wiley & Sons, Inc, 2002.

International Institute of Welding. *Underwater Welding.* New York: Pergamon Press Inc., 1983.

Jacobs, H, G Hees, and W.P Crossley. "The Relationship between the Emission Constant and the Apparent Work Function for Various Oxide-Coted Cathodes." *Proceedings of the IRE.* IEEE, 1948. 1109-1114.

Jagadeesh, G, and K Takayama. "Novel applications of micro-shock waves in biological sciences." (Journal of the Indian Institute of Science) 82, no. 49-57 (2002).

Jones, H M, and E E Kunhardt. "Development of pulsed dielectric breakdown in liquids." (Journal of Physics D: Applied Physics) 28, no. 178-188 (1995).

Komolov, Yu D, and V I Rachovsky. *Total Current Spectroscopy of Surfaces.* Gordon & Breach Science Publishers, 1992.

Korobeinikov, S M, and A V Melekhov. "Breakdown Initiation in Water with the Aid of Bubbles." (High Temperature) 40, no. 5 (2002): 652-659.

Lafferty, James M. *Vacuum Arcs Theory and Application.* San Fransico: John Wiley and Sons, Inc., 1980.

Lan, Sheng, Jizxiang Yang, Jieling Jiang, and Zhiqiang Zhou. "Numerical Simulation of Charged Particles Initiated by Underwater Pulsed Discharge." *Plasma Science and Technology* 11, no. 4 (August 2009).

Lancaster, J F. *The physics of welding, 2nd Edition.* Oxford: Pergamon Press, 1986.
Landau, L D, and E M Lifshitz. *Statistical Physics, Part 1, 3rd Edition.* Oxford: Butterworkth-Heinemann, 1980.

Latham, Rod. *High Voltage Vacuum Insulation, Basic Concepts and Technological Practice.* San Diego: Academic Press Limited, 1995.

Latimer, Wendell M. *The oxidation states of the elements and their potentials in aqueous solutions, 2nd Edition.* United States of America: Prentic-Hall, Inc, 1952.

Lau, K KS, et al. "Superhydrophobic Carbon Nanotube Forests." (Nanoletters) 3, no. 1707-1705 (2003).

Lawson, John, and John Drjavec. *Modern Statistics for Engineering and Quality Improvement.* Pacific Grove, CA: Duxbury, Thomson Learning, 2001.

Lide, David R. *CRC Handbook of Chemistry.* New York, NY: Taylor & Francis, 2007-2008.

Lister, G G, and H G Adler. "Modeling and diagnostics of HID lamp electrodes." Warsaw, Poland: XXIV International conferece on phenomena in ionized gases (ICPIG), 1999.

Liu, S, Q Liu, J Boerio-Goates, and Brian F Woodfield. Preparation of Uniform Naoparticles of Ultra-High Purity Metal Oxides, Mixed Metal Oxides, Metals, and Metal Alloys II. United States of America. 2006.

Lozansky, E. D., and O. B. Firsov. *Theory of Sparks.* Moscow: Atomizdat, 1975.
Lyubimov, G A, and V I Rachovsky. "Cathode spot of vacuum arc." (Advanced Physical Science Uspehi Physics Nauk) 125:995 (1978).

MacKeown, S S. "The cathode drop in an electric arc." (Physics Review) 34, no. 611-617 (1929).

Malton, Steve. *Discussions on the Emission Fraction within SCALA Softawre* Cobham Technical Services, (2009).

Memmott, Joseph M. *Impinging jets evaluated through experimentation and modeling in order to limit the cutting length of a waterjet for dentistry.* MS Thesis, Provo: Brigham Young University, 2003.

Miller. *Miller Educational Content.* 2008. http://www.millerwelds.com/education/articles/articles14.html (accessed August 2008).

Modinos, A. *Field, Thermionic and Secondary Electron Emission Spectroscopy.* New York: Plenum Press, 1984.

Munson, Bruce R, Donald F Young, and Theodore H Okiishi. *Fundamentals of Fluid Mechanics, 4th Edition.* New York, NY: John Wiley & Sons, Inc., 2002.

Murphy, E L, and R H Good. "Thermionic Emission, Field Emission, and the Transition Region." (Physics Review) 106(6), no. 1464-1473 (1956).

Mysinski, Wojciech. "Power Supply Unit for an Electrical Dishcarge Machine." *Power Electronics and Motion Control Conference.* IEEE, 2003. 1321-1325.

Nakamura, Shingihero, and et al. "Optical Measurements of the Electric Field of Pulsed Streamer Dishcarges in Water." *IEEE Transactions on Dielectrics and Electrical Insulation* 16, no. 4 (August 2009).

Namihira, Takao, et al. "Electron Temperature and Electron Density of Underwater Pulsed Discharge Plasma Produced by Solid-State Pulsed-Power Generator." (IEEE Transactions on Plasma Science) 35, no. 3 (2007).

NIST/SEMATECH . *e-Handbook of Statistical Methods.* August 2008. http://www.itl.nist.gov/div898/handbook/ (accessed August 2008).

Odulio, Carl Micheal F, Luis G Sison, and Jr, Miguel T Escoto. "Energy-saving Flyback converter for EDM Applications." *TENCON 2005 IEEE Region 10.* IEEE, 2005. 1-6.

Ogawa, Yoji. "Mechanized underwater welding and cutting for VLFS." (IEEE) International Symposium on Underwater Technology (2002).

Parkansky, N, K Glikman, I I Beilis, B Alterkop, R L Boxman, and D Gindin. "W-C Electrode Erosion in a Pulsed Arc Submerged in Liquid." (Plasma Chemistry and Plasm Processing) Online 25 August 2007 (2007).

Parmar, RS. "Temperature distribution in underwater shielded metal arc welding of free flat plates." (IE(I) Journal - ME) 58, no. July (1977).

Patnaik, Pradyot. *Dean's Analytical Chemistry Handbook, 2nd Edtition.* New York, NY: McGraw-Hill, 2004.

Paulini, J, T Klein, and G Simon. "Thermo-field emission and nottingham effect." (Journal of Physics D: Applied Physics) 23 (1993).

Qian, J, et al. "Microbubble-based Model Anlysis of Liquid Breakdown Initiation by a Sub-microsecond Pulse." (Journal of Applied Physics) 97, no. 11 (2005): 113-304.

Raizer, Yuri P. *Gas discharge physics.* Berlin: Pringer Verlag, 1991.

Ridah, S. "Shock waves in water." (Journal of Applied Physics) 64, no. 152 (1998).

Sakurai, Takao, Yoshihiro Momose, and Keiji Nakayama. "New method to determine the work function using photoelectron emission." *E-Journal of Surface Science and Nanotechnology* (The Surface Science Society of Japan) Vol. 3 (2005): 179-183.

Sano, N, H Wang, M Chhowalla, I Alexandrou, and GA J Amaratunga. "Nanotechnology - Synthesis of carbon 'onions' in water." (Nature) 414, no. 506-507 (2001).

Schneider, Wolfgang. *Studies on arcing phenomena at high current discharges.* England: University of Essex, 1999.

Shadowitz, Albert. *The Electromagnetic Field.* New York: Dover Publications, Inc, 1975.

Simkin, John. *Discussions on the Emission Fraction within SCALA Software* Cobham Technical Services, (2009).

Teo, KBK, C Singh, M Chhowalla, and W I Milne. "Catalytic growth of carbon nanotubes and nanofibers." (Encyclopedia of Nanoscience and Nanotechnology) Edited by H. S. Nalwa (2008-2009).

Terunuma, Y, K Takahashi, T Yoshizawa, and Y Momose. "Temperature Dependence of the Photoelectron Emission from Intentionally Oxidized Copper." *Applied Surface Science* (Elsevier Science B.V.) 115, no. 4 (August 1997): 317-325.

Vector Fields. *Opera-3d Reference Manual.* Software Reference Manual. Vector Fields. 2008-2009.

Vilsmeier, F. *Laserstreuung und Stromtransport im Argon-Bogenplasma, Dissertation.* Munchen: TU Munchen, 1982.

Vladimirov, S V, K Ostrikov, and A A Samarian. *Physics and Applications of Complex Plasmas.* Govent Garden, London, England: Imperial College Press, 2005.

Wang, H, M Chhowalla, N Sano, S Jia, and GAJ Amaratunga. "Large scale synthesis of single-walled carbon nanohorns by submerged arc." (Nanotechnology) 15, no. 546-550 (2004).

Warren, R. "Interpretation of field measurements in the cathode region of glow discharges." (Physics Review) 98, no. 1658-1664 (1955).

Wendelstorf, Jens. *Ab initio modelling of thermal plasma gas discharges (electric arc).* Dissertation, Braunschwieg: Technischen Universitat Carolo-Wilhelmina, 2000.

Wohlfarth, E.P. "Anomalous Values of the Thermionic Emission Constant." (American Physical Society) 74, no. 8 (1948): 964-985.

Wojciechowski, K F. "Work function of transition metals calculated from the Brodie's expression ." (Vacuum) 48, no. Number 3, pp. 257-259(3) (1997).

Woodson, Herbert H, and James R Melcher. *Electromechanical Dynamics, Part II: Fields, Forces, and Motion.* Malabar, Florida: John Wiley and Sons, Inc., 1968.
Yoder, Claude H. *Ionic Compounds.* Hoboken, New Jersey: John Wiley & Sons, Inc., 2006.

Yongning, Liu, Xiaolong Song, Tingkai Zhao, Jiewu Zhu, Michael Hirscher, and Philipp Fritz. "Amorphous carbon nanotubes produced by a temperature controlled DC arc discharge." (Elsevier LTD) Online publishing 16 March 2004 (2004).

Zel'dovich, Ya B, and Yu P Raizer. *Physics of Shock Waves adn High-Temperature Hydrodynamic Phenomena.* New York: Academic, 1966.

Zhukov, M F. *Elecrode Processes in Arc Discharges.* Novosibirsk: Nauka Science, 1982.